

THESIS FOR THE DEGREE OF DOCTOR OF PHILOSOPHY

**Binder Jetting – Influence of the Processing Atmosphere on
Process Robustness and Part Quality of 17-4 PH Stainless Steel**

KAI ZISSEL



CHALMERS

Department of Industrial and Materials Science

CHALMERS UNIVERSITY OF TECHNOLOGY

Gothenburg, Sweden 2025

Binder Jetting – Influence of the Processing Atmosphere on Process Robustness and Part Quality of 17-4 PH Stainless Steel

KAI ZISSEL

ISBN 978-91-8103-207-9

© KAI ZISSEL, 2025

Doktorsavhandlingar vid Chalmers tekniska högskola

Ny serie nr 5665

ISSN 0346-718X

Department of Industrial and Materials Science

Chalmers University of Technology

SE-412 96 Gothenburg

Sweden

Telephone + 46 (0)31-772 1000

Printed by Chalmers Reproservice

Gothenburg, Sweden 2025

Binder Jetting – Influence of the Processing Atmosphere on Process Robustness and Part Quality of 17-4 PH Stainless Steel

KAI ZISSEL

Department of Industrial and Materials Science
Chalmers University of Technology

Abstract

The importance of the processing atmosphere for the Binder Jetting (BJT) technology is often underestimated. Its significance rises as the processing temperatures increase along the process chain. The processing atmosphere can affect the process robustness and part quality, which was investigated for 17-4 PH stainless steel.

The negative effect of curing in ambient air on process robustness was demonstrated, as the reuse of powder collected from depowdering showed slight oxidation, which altered the powder rheology. This, in turn, led to lower powder packing during printing, decreasing green densities and process robustness. Sintering in hydrogen (H_2) could compensate for the lower initial green densities by higher shrinkages but compromised dimensional tolerances. Curing in inert argon (Ar) preserved the powder properties.

The detrimental impact of the binder on part quality was revealed for hollow (shelled) green parts with a binder-affected shell and a binder-free core for sintering in inert Ar since debinding efficiency was low. Binder-affected areas resulted in lower sintering densification as increased carbon pickup from binder residue inhibited the formation of δ -ferrite. In addition, microhardness gradients were obtained after sintering since carbon stabilized austenite, reducing the fractions of martensite formed upon cooling.

The influence of the debinding atmosphere on part quality was investigated for inert, oxidizing and reducing atmosphere compositions. Debinding in inert Ar was ineffective and resulted in low sintered densities ($\sim 88\%$) due to high carbon residue, inhibiting the formation of δ -ferrite. However, the high carbon content led to efficient oxide removal by carbothermal reduction. Debinding in H_2 was inefficient at low temperatures ($300^\circ C$), while H_2 facilitated binder removal at higher temperatures, leading to high sintered densities ($>99\%$) and efficient metal oxide reduction.

Varying oxygen (O_2) content in the debinding atmosphere composition demonstrated that oxidizing atmospheres were efficient in binder removal at lower temperatures, as oxidative binder decomposition required less thermal activation. Increasing the O_2 concentration from 1 vol.% O_2 to 20 vol.% O_2 led to a reduction in the debinding temperatures but an increase in powder oxidation. Prior debinding in Ar + 1 vol.% O_2 ($300^\circ C$, 2 h) combined with sintering in inert Ar ($1300^\circ C$, 2 h) provided the best combination of brown part stability, sintered density ($\sim 98\%$) and sintered chemistry compared to higher O_2 concentrations in the debinding atmosphere. This combination poses a viable alternative to debinding and sintering in explosive H_2 or inert Ar.

Keywords: Binder Jetting, Additive Manufacturing, Powder Reuse, Curing, Debinding, Sintering, Processing Atmosphere, Oxidation, Carbothermal Reduction, Stainless Steel

Preface

The research presented in this doctoral thesis was conducted at the Technology Center of Linde GmbH and the Department of Industrial and Materials Science at Chalmers University of Technology in the framework of the Centre for Additive Manufacturing – Metal (CAM²), supported by the Swedish Governmental Agency of Innovation Systems (Vinnova). The author acknowledges funding by the Federal Ministry of Research and Education (BMBF, Germany) for the project SINEWAVE (FKZ 03HY123A) within the Hydrogen Flagship Project H2Giga.

The work was performed between July 2021 and April 2025. The academic supervisor was Prof. Eduard Hryha and the examiner was Prof. Lars Nyborg. The industrial supervisors were Pierre Forêt and Dr. Sophie Dubiez-Le Goff.

The thesis is based on seven appended Papers, which are listed below. An international patent application (International publication number: WO 2025/056191 A1) was filed as an outcome of this research, which was mainly connected to the findings from Papers V and VI.

List of appended Papers

Paper I: Binder Jetting – Impact of powder reuse and curing on powder characteristics, green parts and sintering densification of 17-4 PH stainless steel

Kai Zissel, Sophie Dubiez-Le Goff, Eduard Hryha

In Manuscript

Paper II: The impact of oxidation during curing of binder jetted 17-4 PH stainless steel on powder properties and powder surface chemistry

Sofia Kazi, Kai Zissel, Eduard Hryha

In Manuscript

Paper III: Binder Jetting – Influence of shell printing on sintering densification and microstructure of 17-4 PH stainless steel

Kai Zissel, Gowtham Soundarapandiyam, Sophie Dubiez-Le Goff, Eduard Hryha

In Manuscript

Paper IV: Binder Jetting – Influence of Processing Atmospheres on Sintering Anisotropy of 17-4 PH Stainless Steel

Kai Zissel, Sophie Dubiez-Le Goff, Umair Khan, Eduard Hryha

Journal of the Japan Society of Powder and Powder Metallurgy, Vol. 72 (Supplement), 2025, pp. S1065-1072

DOI: <https://doi.org/10.2497/jjspm.16A-T7-27>

Paper V: Impact of oxygen content on debinding of binder jetted 17-4 PH stainless steel: Part I – Debinding

Kai Zissel, Elena Bernardo, Pierre Forêt, Eduard Hryha

Powder Metallurgy, Vol. 68(1), 2024, pp. 3–15

DOI: <https://doi.org/10.1177/00325899241307824>

Paper VI: Impact of oxygen content on debinding of binder jetted 17-4 PH stainless steel: Part II – Sintering

Kai Zissel, Elena Bernardo, Pierre Forêt, Eduard Hryha

Powder Metallurgy, Vol. 68(1), 2024, pp. 16–28

DOI: <https://doi.org/10.1177/00325899241307871>

Paper VII: Impact of debinding atmosphere composition on binder removal and powder oxidation of binder jetted 17-4 PH stainless steel

Kai Zissel, Anok Babu Nagaram, Sophie Dubiez-Le Goff, Eduard Hryha

In Manuscript

Contribution to the appended Papers

Paper I: The author planned and conceptualized the study together with the co-authors. The author performed the majority of the experimental work and analysis of the results. The author drafted the manuscript and revised the Paper in close collaboration with the co-authors.

Paper II: The author planned and conceptualized the study together with the co-authors. The author carried out the curing of the powder and subsequent flowability and packing tests. The author performed chemical analysis of the powder. Sofia Kazi conducted powder analysis by scanning electron microscopy along with X-ray photoelectron spectroscopy and drafted the manuscript. The author revised the Paper in close collaboration with the co-authors.

Paper III: The author planned and conceptualized the study together with the co-authors. The author performed the majority of the experimental work and analysis of the results. Gowtham Soundarapandiyam conducted electron backscatter diffraction measurements. The author drafted the manuscript and revised the Paper in close collaboration with the co-authors.

Paper IV: The author planned and conceptualized the study together with the co-authors. The author performed the majority of the experimental work and analysis of the results. Umair Khan performed the metallographic preparation and light optical microscopy. The author drafted the manuscript and revised the Paper in close collaboration with the co-authors.

Paper V: The author planned and conceptualized the study together with the co-authors. The author performed the majority of the experimental work and analysis of the results. The author drafted the manuscript and revised the Paper in close collaboration with the co-authors.

Paper VI: The author planned and conceptualized the study together with the co-authors. The author performed the majority of the experimental work and analysis of the results. The author drafted the manuscript and revised the Paper in close collaboration with the co-authors.

Paper VII: The author planned and conceptualized the study together with the co-authors. The author was involved in the experimental execution and analyzed the results. Anok Babu Nagaram performed thermogravimetric trials. Carbon analysis was conducted at Höganäs AB. The author drafted the manuscript and revised the Paper in close collaboration with the co-authors.

Table of Contents

1	Introduction	1
1.1	Background & Motivation	1
1.2	Research Objectives.....	3
2	Metal Binder Jetting	5
2.1	Printing, Curing & Depowdering	5
2.2	Debinding	6
2.3	Sintering.....	7
2.4	Material Selection.....	10
2.4.1	Binders.....	10
2.4.2	Powders.....	11
2.4.3	17-4 PH Stainless Steel	11
2.5	Possibilities.....	12
2.6	Challenges	13
2.7	Applications.....	14
2.8	Process Parameters	15
3	Role of the Processing Atmosphere	17
3.1	Printing, Curing & Depowdering Atmospheres	17
3.2	Debinding Atmospheres	18
3.3	Sintering Atmospheres.....	19
4	Experimental Methods	23
4.1	Materials & Printing	23
4.2	Curing & Depowdering.....	25
4.3	Powder Reuse & Curing Atmosphere	25
4.4	Debinding & Sintering	26
4.4.1	Tube Furnace.....	26
4.4.2	Dilatometry	26
4.4.3	Thermogravimetry.....	27
4.5	Material Characterization	28
4.5.1	Powder Characterization.....	28
4.5.2	Elemental Analysis	29
4.5.3	Density Determination	29

4.5.4	Microstructural Investigation.....	29
4.5.5	Microhardness Testing.....	29
4.6	Thermodynamic Simulations.....	29
5	Summary of Results.....	31
5.1	Influence of curing atmosphere and powder reuse on powder characteristics, green parts and sintering densification.....	31
5.2	Impact of binder content and distribution on powder packing, sintering densification, microstructure gradients and shrinkage anisotropy.....	34
5.3	Impact of oxygen content in the debinding atmosphere on binder removal, powder oxidation and sintering densification.....	38
6	Conclusions.....	45
7	Future Work.....	49
	Acknowledgments.....	51
	References.....	53

List of Abbreviations

Acronym	Description
3D	Three-dimensional
AM	Additive Manufacturing
Ar	Argon
bcc	Body-centered cubic
BJT (BJT-MSt/M)	Binder Jetting
C	Carbon
CAD	Computer-aided design
C _n H _m	Hydrocarbon
CO	Carbon monoxide (gaseous)
CO ₂	Carbon dioxide (gaseous)
Cr	Chromium
Cu	Copper
DEG	Diethylene glycol
EBSD	Electron backscatter diffraction
EG	Ethylene glycol
fcc	Face-centered cubic
Fe	Iron
FTIR	Fourier transform infrared spectroscopy
H ₂	Hydrogen (gaseous)
H ₂ O	Water (gaseous)
He	Helium (gaseous)
HIP	Hot Isostatic Pressing
HV	Vickers hardness
ICP-OES	Inductively coupled plasma optical emission spectroscopy
LOM	Light optical microscopy
MBJ	Metal Binder Jetting
MIM	Metal Injection Molding
Mn	Manganese
N ₂	Nitrogen (gaseous)
Nb	Niobium
Ni	Nickel
O ₂	Oxygen (gaseous)
PAA	Polyacrylic acid
PBF	Powder Bed Fusion
PBF-LB/M	Laser-based powder bed fusion of metals
PH	Precipitation-hardened
PM	Powder Metallurgy
PSD	Particle size distribution

PVA	Polyvinyl alcohol
PVP	Polyvinylpyrrolidone
RQ	Research question
SBAM	Sinter-based Additive Manufacturing
SEM	Scanning electron microscopy
Si	Silicon
SXCT	Synchrotron X-ray computed tomography
Ta	Tantalum
TG	Thermogravimetry
TRL	Technology readiness level
UV	Ultraviolet
XPS	X-ray photoelectron spectroscopy
XRF	X-ray fluorescence

List of Symbols

Symbol	Description
ΔG°	Standard Gibbs free energy change
ΔH°	Standard enthalpy change
ΔS°	Standard entropy change
D_{10}	10 th percentile
D_{50}	50 th percentile
D_{90}	90 th percentile
K	Equilibrium constant (reaction)
K_1, K_2, K_3	Anisotropic factors
R	Molar gas constant
T	Temperature
ε_x	Shrinkage in X-direction (powder spreading direction)
ε_y	Shrinkage in Y-direction (compaction roller axis direction)
ε_z	Shrinkage in Z-direction (build direction)

1 Introduction

1.1 Background & Motivation

Additive Manufacturing (AM) is a manufacturing technology where three-dimensional parts are produced by the successive addition of material, typically layer upon layer. AM enables the creation of complex and novel designs for metal parts that were not achievable with conventional manufacturing methods such as machining, casting and forging [1,2]. Further advantages of AM compared to traditional manufacturing methods include part consolidation, topology optimization, rapid prototyping, mass customization, on-demand production and reduced material waste [3–5].

The benefits of metal AM have been utilized in various industries, particularly in healthcare and aerospace [6,7]. The adoption of metal AM technologies is primarily limited by high part costs and low productivity compared to traditional manufacturing technologies, especially for cost-driven industries such as automotive [8,9]. Various types of metal AM technologies exist with different advantages and disadvantages [10].

Binder Jetting (BJT) is an emerging metal AM technology that offers the potential to reduce manufacturing costs and increase production speeds compared to other metal AM technologies, such as Powder Bed Fusion (PBF) [1]. BJT is currently considered the most important sinter-based AM (SBAM) technology due to its high technology readiness level (TRL) and productivity compared to other SBAM processes [11]. BJT is classified as a multi-step process for metal part production according to ISO/ASTM 52900:2021 [12], which requires liquid binder and metal powder for printing and further sintering of the printed part to reach the necessary material properties.

During the printing process, the binder is selectively deposited onto spread layers of powder via inkjet technology to glue the metal particles together. This process is repeated layer by layer until the desired part is formed. After the printing process, the powder bed is subjected to a heat treatment to harden the binder, which is defined as curing. The curing process provides sufficient strength to the printed parts so that they can be separated from the surrounding loose powder, which is known as depowdering. At this stage, the part is termed green part and typically has a relative density between 50 % and 60 % [1,13]. The green part is placed into a furnace for debinding and sintering at high temperatures, where the binder is removed and a dense metal component is obtained. BJT components shrink by 10 % to 20 % in all three dimensions during sintering, depending on the initial green density and required densification [11,14].

Each process step is characterized by multiple adjustable process parameters that influence the outcome of the final part. The processing atmosphere is a parameter that is encountered within all process steps. A well-controlled and tailored processing atmosphere is necessary to ensure a robust manufacturing process and high-quality parts. The importance of the processing atmosphere rises along the multi-step process as the processing temperatures increase.

Achieving consistent green part quality is a significant challenge in BJT since it requires stable powder characteristics. During the production of green parts, excess powder is collected from printing (overflow powder) and depowdering (depowdered powder). This loose powder is typically reused to ensure a cost-efficient and sustainable manufacturing process. Printing is usually conducted in ambient conditions at room temperature, where the impact of the atmosphere on the powder characteristics is generally considered negligible.

In contrast, the depowdered powder is subjected to elevated temperatures between 150°C and 250°C during the curing process, which is commonly conducted in ambient air [15,16]. As the binder is hardened, the powder is prone to oxidation. Powder degradation resulting from powder reuse and curing can potentially compromise printing repeatability. However, there is limited research on powder reusability and the effect of the curing atmosphere on powder characteristics and process robustness. Therefore, it is crucial to study the influence of powder reuse and curing on powder characteristics, green parts and sintering densification.

Stainless steels such as 17-4 PH are a primary choice for binder-assisted powder manufacturing technologies, including BJT [17,18], which must fulfill the required mechanical properties for structural applications. The polymeric binder, however, is a source of carbon, oxygen and nitrogen. These elements can negatively impact the sintering densification, sintered microstructure and mechanical properties of stainless steels [14,18]. A detailed understanding of how binder residue influences the sintering densification and microstructure of 17-4 PH stainless steel is essential. Therefore, hollow green parts with varying shell thickness were printed and sintered in argon (Ar) and hydrogen (H₂) to assess the influence of the binder in common processing atmospheres. In addition, the shrinkage anisotropy of standard green samples processed in Ar and H₂ was investigated.

The debinding process determines the effectiveness of the binder removal. The binder is typically removed in a single-stage thermal debinding process for BJT green parts [11]. Successful debinding is defined as complete binder removal without defect formation in the part while preserving the powder quality. The choice of the processing atmosphere can significantly alter the binder decomposition and chemical reactions with the powder, determining the success of the debinding step. Thermal debinding can be conducted in inert, reducing or oxidizing atmospheres.

Inert atmospheres such as Ar protect the powder from oxidation but exhibit low debinding activity as the binder decomposition relies on the thermal degradation of the polymer itself. Debinding in a reducing H₂-containing atmosphere efficiently removes binder and carbon [19]. However, the use of H₂ gas might be avoided due to local regulations and safety concerns requiring special furnace designs [20].

Oxidizing atmospheres containing oxygen (O_2) enhance the polymer decomposition. Debinding in air is an efficient concept that can be accomplished in simple furnace designs. However, a considerable drawback is the susceptibility of the metal powder to oxidation. Severe powder oxidation is detrimental to sintering densification, mechanical performance and corrosion resistance of sintered stainless steels [21–23]. This becomes more problematic for oxygen-sensitive materials.

One strategy to balance binder removal and powder oxidation in an oxidizing atmosphere is to reduce the O_2 concentration. Using a tailored debinding atmosphere can offer the potential to improve the final part quality. The combination with an inert sintering atmosphere can provide an alternative to debinding and sintering in an H_2 atmosphere. Consequently, the influence of the O_2 content in the debinding atmosphere on binder removal and powder oxidation was explored. The impact on the subsequent sintering densification and part properties was studied for sintering in inert Ar within this thesis.

1.2 Research Objectives

The first part of this thesis aimed to highlight the role of the curing atmosphere and powder reuse on the process robustness. The process robustness was evaluated by printing accuracy, green part density, sintering shrinkage (dimensions) and sintered porosity. The reusability of 17-4 PH powder was assessed for 20 consecutive build jobs, while the influence of curing in ambient air and inert Ar on powder characteristics was compared. The printing of consistent green parts was a pre-requisite for reliably comparing the effects of debinding and sintering atmospheres.

The second part of this thesis focused on understanding how the binder content and its distribution affect the sintered part quality. Therefore, the influence of binder content and its distribution on sintering densification, microstructure and hardness of 17-4 PH stainless steel was investigated. Based on these insights, the influence of the debinding and sintering atmospheres on part quality could be evaluated.

The third part of this thesis explored the concept of reduced O_2 content in the debinding atmosphere to improve the sintered part quality. The aim was to provide an alternative to debinding and sintering in H_2 by combining a tailored debinding atmosphere with sintering in inert Ar. Thus, the influence of the O_2 concentration in the debinding atmosphere on binder removal and powder oxidation was studied. Subsequent sintering of the brown parts was conducted to assess the impact on sintering densification, microstructure and sintered chemistry.

Based on the objectives, the following research questions (RQ) were formulated:

1. What is the influence of the curing atmosphere and powder reuse on powder characteristics, green parts and sintering densification?
2. How do binder content and its distribution impact powder packing, sintering densification, microstructure gradients and shrinkage anisotropy?
3. What is the impact of oxygen content in the debinding atmosphere on binder removal, powder oxidation and subsequent sintering densification?

The resulting structure of the thesis and the addressed research questions in the appended Papers are visualized in Figure 1.

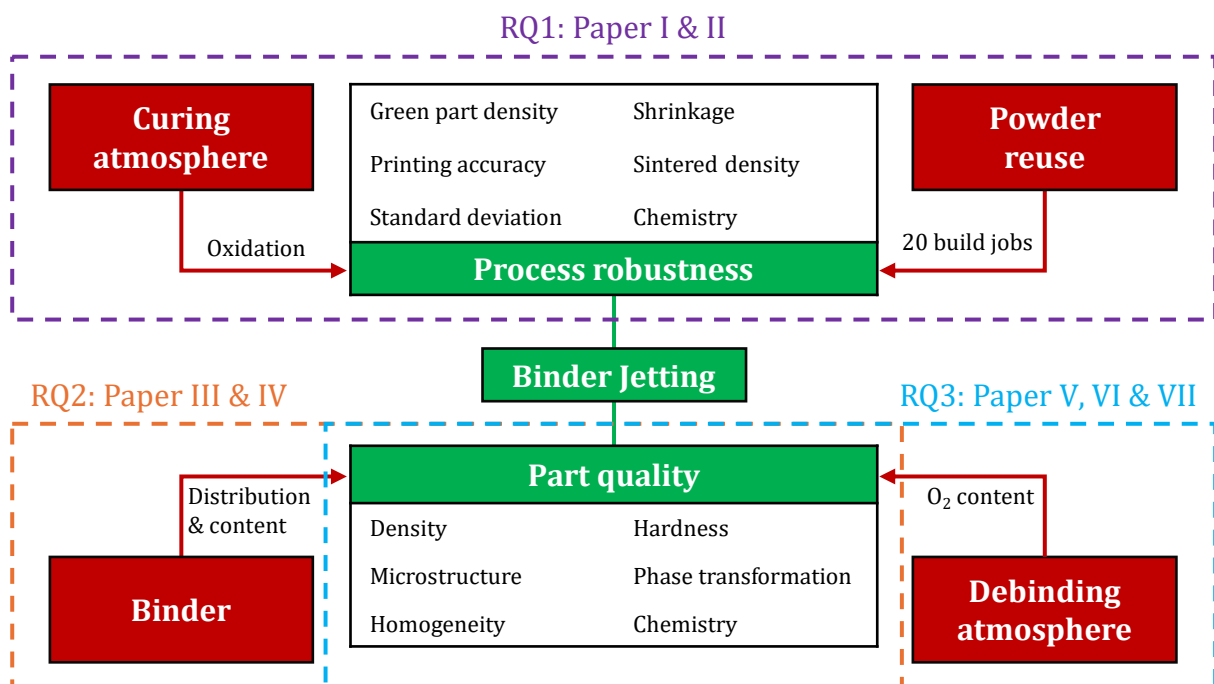


Figure 1: Thesis structure and addressed research questions in the appended Papers I to VII.

2 Metal Binder Jetting

Binder Jetting (BJT) is specified as a multi-step process (-MSt) for metals (/M), leading to the abbreviation BJT-MSt/M according to ISO/ASTM 52900:2021 [12]. The technology is also often referred to as Metal Binder Jetting (MBJ) [24]. For simplicity, the abbreviation BJT will be used throughout this thesis. The BJT process requires metal powder and liquid binder as the feedstock material [12]. Figure 2 visualizes the process steps required for BJT of metals, which include printing, curing, depowdering, debinding and sintering.

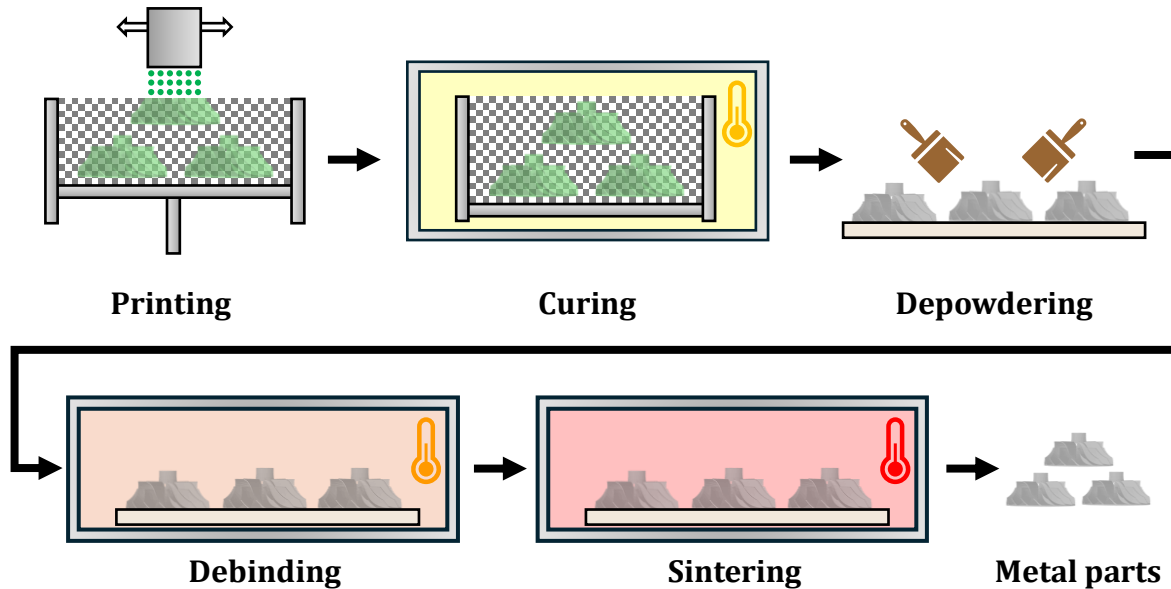


Figure 2: Sketch of the BJT process chain for metal parts consisting of printing, curing, depowdering, debinding and sintering.

Details on each process step are provided within this chapter. In addition, the binders and powders used for BJT are briefly summarized. The possibilities and challenges of the BJT technology will be discussed shortly. In addition, several examples of industrial BJT applications are presented. Finally, an overview of typical BJT process parameters is given. More information on each aspect can be found in the cited sources.

2.1 Printing, Curing & Depowdering

Figure 3 depicts the principle of the BJT printing process step. The printing starts with spreading powder onto a build plate, which is placed within a build box. The powder is then compacted by a roller or rake to form a dense powder layer [25]. A printhead then deposits liquid binder onto specific areas of the powder layer to selectively glue the metal particles together. The specific areas of each layer are determined by a slice of the part geometry at the specific layer height. Some binders and systems require heat or ultraviolet (UV) radiation to dry or cure the binder after the deposition [14,25,26]. Finally, the build plate is lowered by a defined layer thickness and a new layer of powder is spread on top of the previous layer.

The described steps are repeated until one or multiple three-dimensional (3D) components are generated. The printed parts, which are a mixture of metal powder and binder, are surrounded by a loose powder bed in the build box.

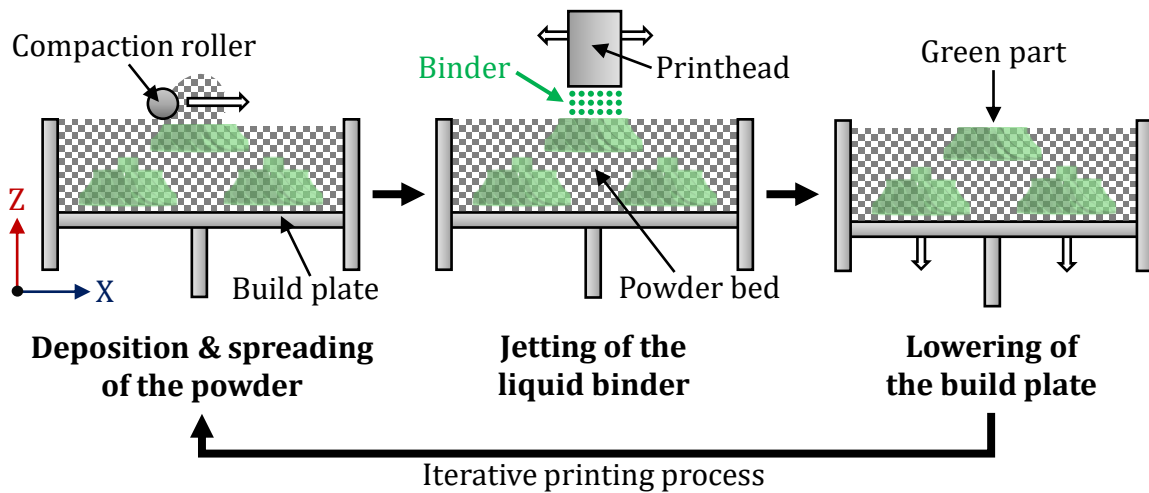


Figure 3: Illustration of the layer-wise BJT printing process for the production of green parts.

After the printing process, the build box is typically transferred into a furnace for curing to harden the binder, which is usually conducted at temperatures between 150°C and 250°C [15]. During curing, solvents evaporate and binder crosslinking can be induced depending on the binder composition [14]. During curing, the parts gain sufficient strength to separate them from the loose and compacted powder in the build box [1]. The printed parts are referred to as green parts.

Aids such as brushes and compressed air or gases are used to free the green parts from the powder bed, which is termed depowdering [1]. The green strength of BJT green parts can usually range from ~1 MPa to ~14 MPa depending on the binder composition, printing parameters, testing method and measurement direction [27–32]. Consequently, depowdering is a critical step since the intricate green parts can be easily broken during depowdering, especially for small and overhanging features. The obtained green parts usually have a density between 50 % and 60 % of the theoretical material density [1,13].

2.2 Debinding

Debinding refers to the process step where the sacrificial binder is removed. The debinding of BJT components is typically achieved via thermal debinding at temperatures between 300°C and 700°C, depending on the used binder and powder material [11]. Successful debinding is defined as complete binder removal without inflicting defects in the green part [19,33].

Impurities introduced by binder residue due to insufficient debinding can be detrimental to the mechanical properties and corrosion behavior of the material [11]. The polymeric binder is a potential source of carbon, oxygen, hydrogen and nitrogen [34,35], which can be picked up by the metal in case of incomplete binder removal. Residual carbon can

significantly affect the sintering densification and final material properties depending on the material's sensitivity to carbon [33,36–39].

Various chemical reactions can take place as binders are subjected to high temperatures, which include pyrolysis, oxidation or hydrogenation [19,33,40]. During the debinding process, binders typically decompose into lower-molecular weight species such as carbon dioxide (CO₂), carbon monoxide (CO), water (H₂O), various hydrocarbons (C_nH_m) or similar vapor products [19,41,42]. The sequence of thermal debinding usually includes binder expansion, binder melting (depending on the polymer), binder vaporization, diffusive vapor transport through the pores and finally the convective transport of the vapor products out of the furnace by gas flow [19,33,40].

The debinding process is usually limited by the heating rate. High heating rates can induce cracks in the green part due to stress gradients related to temperature and pressure [19]. Excessive vapor pressure buildup in the green part can cause cracks and blisters during debinding [19,33]. Slow heating rates and holding times at intermediate temperatures minimize the risk of defect formation during debinding [19,33]. The temperature profile set for debinding needs to strike a balance between minimum processing time and defect-free binder removal [43]. After the debinding process, the part is considered a brown part [16]. The debinding and subsequent sintering are usually combined into a single furnace cycle.

2.3 Sintering

Sintering is defined as the “thermal treatment of a powder or compact, at a temperature below the melting point of the main constituent, for the purpose of increasing its strength by the metallurgical bonding of its particles” according to ISO 3252:2023 [44]. The fundamental driving force of sintering is the reduction of the internal surface and interface energy of the powder compact, which is much higher than the bulk material of the same mass.

The minimization of the interfacial energy is achieved by two mechanisms. One mechanism is the densification that transforms solid-gaseous interfaces into solid-solid interfaces, reducing the interfacial energy. Another mechanism is grain growth, which reduces the grain boundary surface area and, thereby, the interfacial energy [45]. These mechanisms occur simultaneously during sintering.

Figure 4 presents the different types of mass transport mechanisms encountered during the sintering of crystalline materials for three adjacent particles. The mass transport mechanisms or paths include surface diffusion, volume (lattice) diffusion, grain boundary diffusion, plastic flow and vapor transport (evaporation and condensation) [46]. The mass transport mechanisms are generally distinguished into densifying and non-densifying mechanisms [46,47].

Atomic motion via surface diffusion, lattice diffusion and vapor transport from the particle surface to the neck leads to neck growth and particle coarsening but no densification or

shrinkage [46]. In contrast, grain boundary diffusion and lattice diffusion from the grain boundaries to the neck, as well as plastic flow, cause neck growth and densification [46]. In summary, densification during sintering requires mass transfer from the particle interior to the particle neck, where vacancy annihilation occurs by particle rearrangement and rotation [48].

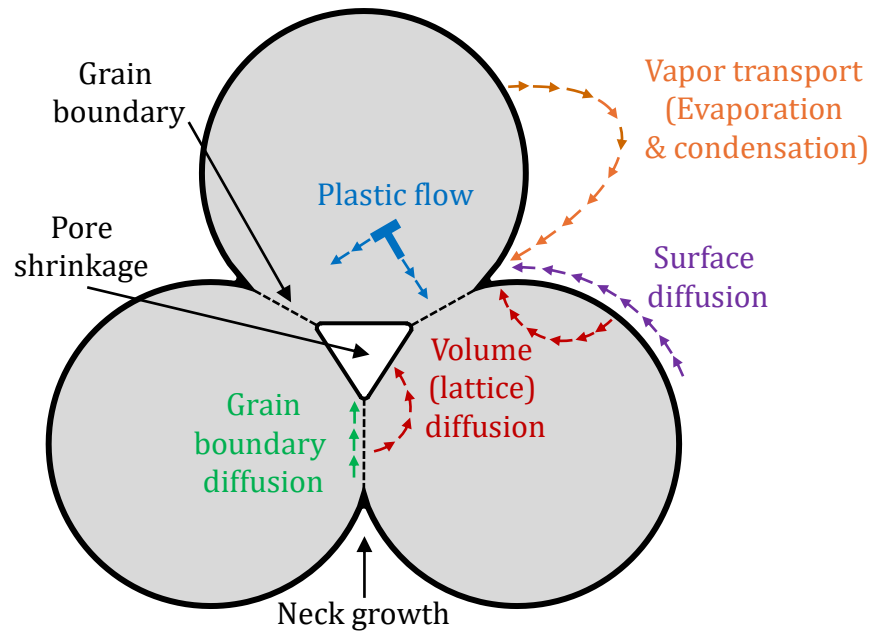


Figure 4: Different types of mass transport mechanisms during the sintering of crystalline materials visualized for three spherical particles. Figure adapted from [45].

Surface diffusion is the dominant sintering mechanism at low temperatures for many metals because the activation energy is lower compared to those of other mass transport mechanisms [48]. For the sintering densification of most metals, grain boundary diffusion is important [48]. The activation energy for grain boundary diffusion is higher than for surface diffusion but lower than for volume diffusion in most cases [48]. Grain growth, however, decreases the significance of grain boundary diffusion [48]. Volume diffusion is active at high temperatures for most materials but is often not the dominant mass transport mechanism during sintering, especially for small particle sizes [48].

Sintering can be divided into different stages, which describe the geometric progression from a loose powder compact to a metal part with high sintered density [49]. Figure 5 illustrates the evolution of the relative density and microstructure during sintering. The starting point is a loosely packed powder, where weak atomic forces at the particle contacts, such as van der Waals forces, keep the particles together [49].

The initial (first) stage of sintering begins with the growth of sintering necks by short-range atomic motion between the contacting particles, where the sintering is dominated by the gradient in the curvature from the particle surface to the root of the neck [45,48,49]. A grain boundary forms within the neck due to the random crystal orientations of the grains relative to each other [49]. At this stage, each neck grows independently of its neighbors [49]. The sintering necks in the initial stage are small, with

up to one-third in size of the particle [49]. Minor dimensional changes occur in the initial stage with maximum linear shrinkages of 3 % [48], which usually corresponds to relative densities below 70 %.

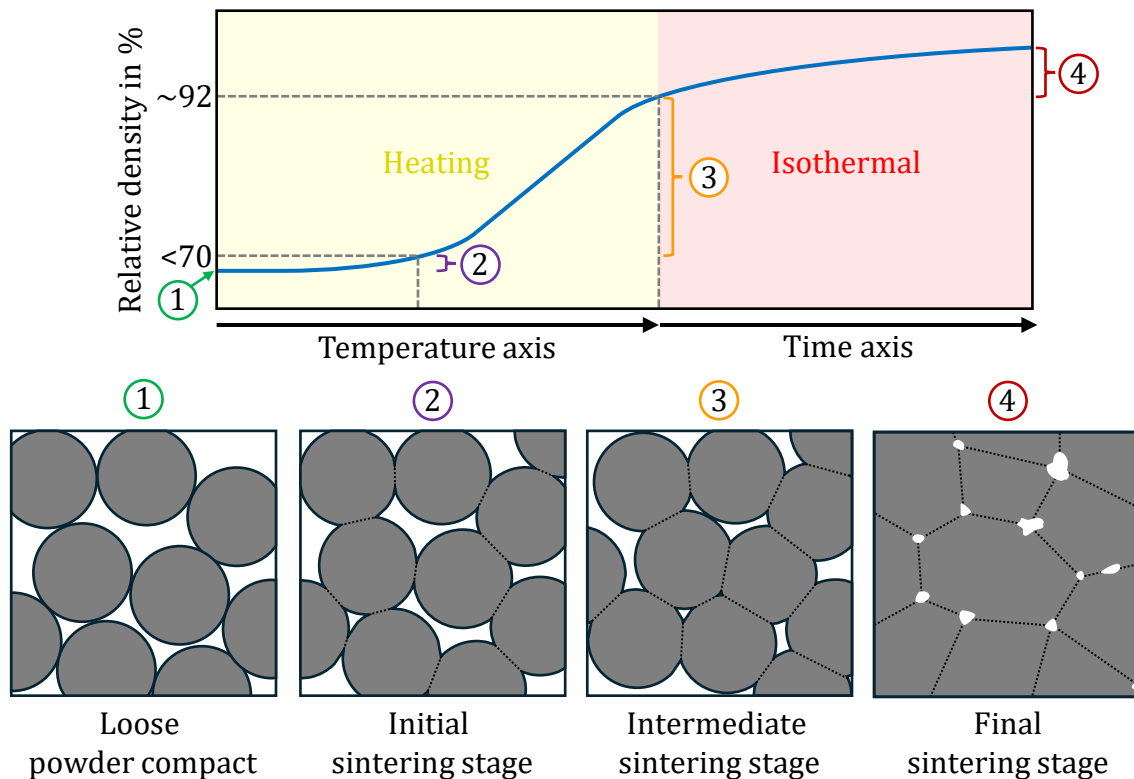


Figure 5: Schematic illustration of density and microstructure evolution during sintering. Figure adapted from [48,50].

The intermediate (second) stage of sintering encompasses pore rounding and the onset of grain growth [48]. The pores remain interconnected during the intermediate sintering stage, forming a network of tubular pores located at the grain boundaries [48,49]. At this stage, the interconnected porosity is still open to the external atmosphere [48]. The intermediate stage corresponds to necks larger than one-third of the particle size but less than half of the particle size [48]. The relative density ranges from 70 % to 92 % in the intermediate stage [48].

During the final (third) sintering stage, the pores collapse into closed spherical voids, which is typically encountered at ~92 % of relative density [48,49]. The pores do not remain open to the external surface and the isolated pores are filled with the processing atmosphere [48]. All pores are closed at ~5 % of remaining porosity [49], which are located at grain boundaries or inside the grains. The closed pores result in less hindrance to grain growth [48]. Densification occurs by vacancy diffusion from the pores to the grain boundaries but slows down since grain boundary areas decline due to grain growth [45].

The remaining pores after sintering are primarily smooth and spherical with different sizes, which cause vacancy concentration gradients [48]. The small pores act as vacancy sources, while the large pores act as vacancy sinks. The vacancy concentration gradients

cause coarsening of the large pores, while the small pores are eventually eliminated [48]. During the final stage, closed pores become distorted due to migration of the pores as the pores try to remain on the moving grain boundaries [48].

Sintering can be categorized into solid-state sintering and liquid-phase sintering [51]. Solid-state sintering refers to the densification of the powder compact in a fully solid state. In contrast, liquid-phase sintering involves the formation of a liquid phase in the powder compact [51]. Liquid phases accelerate sintering since atomic motion is faster in a liquid than in a solid [52,53]. Excessive liquid formation can, however, cause part distortion during sintering, which makes shape retention of complex geometries challenging [53]. In this thesis, solid-state sintering was investigated due to lower temperature requirements and improved shape retention.

Post-processing can be applied after sintering, depending on the application, but increases manufacturing costs and time. Hot Isostatic Pressing (HIP) can be used to eliminate residual porosity for high-performance applications [54–56]. Heat treatments such as aging can be applied to adjust the material properties after sintering [1]. Surface finishing operations such as sandblasting or electropolishing can be performed to minimize the surface roughness of the component [57]. Machining can be utilized if tight tolerances must be fulfilled.

2.4 Material Selection

Common binders and metal powder grades used for BJT are briefly listed in this section. In addition, the material 17-4 PH stainless steel is shortly introduced, which was the material of interest for this thesis study.

2.4.1 Binders

The binder selection is critical as it must fulfill several requirements. The binder must provide sufficient rheology and chemical stability for inkjet printing [1,58]. Furthermore, the binder must enable proper wetting and penetration of the powder bed [1,58]. Additionally, the binder must ensure sufficient binding strength for green part stability, but it must also be easily removable during debinding without leaving binder residue in the material [1,58]. Moreover, the binder and powder need to be compatible [16].

This overview is limited to polymeric binders. Liquid binders for BJT are typically polymer-solvent mixtures in order to achieve the rheological properties required for inkjet printing [36,59]. The solvent can be water-based, but other solvents can also be used [36]. Water-based binders are more common, as non-aqueous binders often include flammable or hazardous solvents [36]. Water-based binders usually contain other additives to adjust the binder properties [36]. The solvent is evaporated during printing or curing. The polymer can be thermosetting, which means the binder is crosslinked at elevated temperatures during curing, which increases the green part strength [5,60].

Commercially available binders are usually proprietary and their exact composition is not disclosed. Various binder formulations were studied and described in the literature. Some

examples of polymeric binders are polyvinylpyrrolidone (PVP), polyvinyl alcohol (PVA), polyacrylic acid (PAA), diethylene glycol (DEG) and ethylene glycol (EG) [61,62]. As previously discussed, these polymers are sources of carbon, oxygen, nitrogen and hydrogen [34,35], which can be picked up by the metal during BJT processing.

2.4.2 Powders

In theory, the BJT technology can process any powder that can be sintered but is constrained by the powder processability during printing and the binder compatibility. Fine particle sizes below 20 μm are generally favored for BJT since the higher surface area leads to earlier sintering onset and faster densification compared to conditions for coarser particles [1]. Spherical powder morphologies are preferred since such powder exhibits increased flowability and higher powder bed densities can be achieved [1,63,64].

In many cases, inexpensive powder grades for Metal Injection Molding (MIM) can be used for BJT [11,65]. Therefore, the material properties of BJT parts are often compared to those of MIM parts due to the similarities in the powder feedstock, green parts and thermal processing [11]. Nevertheless, the introduction and qualification of new materials for BJT might require extensive process development.

The BJT processing of various metal powder grades was reported in the literature, where a selection of materials is listed in this section. The BJT technology can process stainless steels [13,26,66,67], nickel-based alloys [68–70], cobalt-based alloys [71], aluminum alloys [72,73], titanium alloys [74] and magnesium alloys [75–77]. Copper can also be processed [78–81]. The sinter-based technology also enables the processing of non-weldable or difficult-to-weld materials such as carbon-containing tool steels [82,83] and hard metals [84–87]. Cemented carbides (WC-Co) can also be manufactured via BJT [88]. Furthermore, BJT is also used to print sand molds for metal casting [89].

The manufacturers of BJT printers usually offer a choice of binders and metal powders, where the material and process parameters are optimized for the corresponding BJT platform. The qualification status and availability of material data sheets vary depending on the supplier and material. Currently, metal powders and binders are commercially available for stainless steels (17-4 PH, 316L, 304L, 420, 440C), low alloy steels (4140, 4340, 4605), tool steels (D2, H13, M2, S7), titanium alloys (Ti-6Al-4V), nickel-based superalloys (Haynes 230, IN625, IN718, M247), aluminum alloys (6061), bronze, chromium zirconium copper (C18150), cobalt chrome, copper, silver, gold and tungsten carbide [90–95]. This list of materials is not extensive and is limited to materials directly advertised on the websites of several BJT printer manufacturers.

2.4.3 17-4 PH Stainless Steel

The most popular precipitation-hardened (PH) martensitic stainless steel is 17-4 PH stainless steel [18,96]. Other designations of the same material are UNS S17400, AISI 630, ASTM A564 (Type 630), MIM-17-4 PH and AMS 5643 [18]. The 17-4 PH stainless steel combines strength, hardness and corrosion resistance, making it ideal for aerospace, medical, dental, nuclear and consumer industries [18]. The 17-4 PH stainless steel is

readily available for most commercial BJT platforms and was chosen as the material for investigation within this thesis. Table 1 specifies the elemental composition of 17-4 PH stainless steel according to MIM standards [97,98], which are a common reference for BJT due to the similar processing.

Table 1: Specification of the chemical composition of 17-4 PH in wt.% according to MPIF35/ASTM B883 – 24 [97,98].

Element	Fe	C	Cr	Ni	Cu	Si	Mn	Nb + Ta	Other
Min. in wt.%	Bal.	-	15.5	3	3	-	-	0.15	-
Max. in wt.%	Bal.	0.07	17.5	5	5	1.0	1.0	0.45	1.0

The high chromium (Cr) content is responsible for the corrosion properties of 17-4 PH, while the nickel (Ni) content ensures the hardenability of the steel [99]. Copper (Cu) induces precipitation hardening by the formation of Cu-rich precipitates, which strengthens the martensitic matrix of 17-4 PH [99–103]. The martensitic matrix has a bcc crystal structure with a lath morphology [99].

The microstructure of 17-4 PH usually consists of martensite, δ -ferrite and residual pores after sintering [102,104]. Retained austenite may also be present [104]. The fractions of δ -ferrite depend on the sintering temperature and carbon content [102,104]. The δ -ferrite plays an important role in the sintering densification of 17-4 PH stainless steel due to its body-centered cubic (bcc) crystal structure, which has a higher self-diffusivity in comparison to the face-centered cubic (fcc) crystal structure of the γ -austenite [104,105]. The higher self-diffusivity in bcc is connected to a lower atomic packing factor of 0.68 compared to 0.74 for fcc, therefore resulting in higher mobility of atoms and interstitials in the bcc lattice [106,107].

The properties of 17-4 PH can be adjusted by heat treatment after sintering, including solution and aging treatments [96,108,109]. Precipitation hardening is induced by the aging of the material at temperatures between 480°C and 600°C [110]. Aging treatments at 482°C for 1 h (H900), 525°C for 1 h (H975) or 550°C for 1 h (H1025) are commonly applied for MIM of 17-4 PH according to ASTM B883 – 24 [98].

2.5 Possibilities

The BJT technology offers the potential of large production volumes at a higher cost-efficiency than other metal AM technologies [1,111]. BJT excels at productivity compared to laser-based powder bed fusion of metals (PBF-LB/M) [1,111], which is the most widespread metal AM technology in the industry [112,113]. Build rates of up to 12000 cm³/h are claimed in the case of BJT printing [11,114]. The BJT process demonstrated the potential to lower part production costs compared to PBF-LB/M, depending on the part geometry and utilization of the build volume [115,116]. Compared to other SBAM processes, BJT stands out due to its high productivity and scalability [11].

As BJT printing involves no melting and is conducted at room temperature, no issues related to thermal stresses, elemental segregation or oxidation are encountered in contrast to other metal AM processes [1]. In addition, the reusability of powder is considered high [1]. No support structures or attachment to the build plate is required due to the cold printing process [1]. Hence, parts can be stacked on top of each other to increase the utilization of the build volume [117].

The BJT of metals combines the advantages of AM with the potential material variety of traditional Powder Metallurgy (PM). BJT offers a huge material variety [63,111] and enables the use of MIM powders, as explained in Section 2.4.2. Therefore, BJT creates new possibilities in part design and production flexibility for manufacturers already practicing MIM or other traditional PM technologies, as the thermal processing and obtained material properties are comparable [113,117].

The sintering usually leads to isotropic grain morphology [26,111], while non-uniform microstructures are formed during PBF-LB/M connected to the rapid solidification process [118]. The sintering of fine particles can also result in lower surface roughness compared to PBF-LB/M [115,119], where bad surface quality is caused by the required printing support structures and unwanted powder sintering at down-facing (down-skin) part surfaces [117,120,121]. The BJT printing and sintering process can further be utilized for designed porosity on the mm and sub- μm levels [63].

2.6 Challenges

The minimum feature or part size is often constrained by the ability to depowder the part successfully without damaging it [1]. Small, intricate, or overhanging features might be easily broken due to depowdering [1,111], lowering the production yield. The ability to remove powder from cavities and tubes must also be considered during part design.

Even if the depowdering of complex geometries can be performed successfully, the process is time-consuming and requires costly manual labor [11,113,122,123]. Additionally, the operator is potentially exposed to fine metal powder during depowdering [11,123]. The listed difficulties associated with depowdering can be addressed by enhancing the green part strength, which increases the potential for automated solutions and more forceful depowdering methods [117]. In addition, the automation of handling green parts and powder is pursued [113].

While sintering offers advantages, it also comes with challenges in dimensional control since the green parts undergo high shrinkage towards full densification [11]. The shrinkage of BJT components is anisotropic [117,124], which must be considered during the part design phase. In addition, part distortion can occur during sintering due to gravity and friction with sintering setters [117]. Depending on the part design, sintering supports might be required to avoid sintering distortion [117].

Consequently, the manufacturing of complex shapes usually requires multiple design iterations to achieve the desired sintered geometry, which renders single-part production

economically challenging [65]. Therefore, sintering simulations are developed and utilized to predict the sintering shrinkage and adapt the part design based on the sintering simulation feedback to minimize design iterations and overcome the challenges of dimensional control [125–128].

In addition, safety concerns arise during BJT due to the fine metal powder involved [11]. Powders with particle sizes smaller than 15 μm pose significant safety risks as powder clouds can be formed with a potential for ignition or explosion [1]. Furthermore, fine metal powder requires respiratory and skin protection for the operator [1], especially for carcinogenic materials. Health concerns can also arise from the binder, as the binder or its volatile organic compounds can be problematic, requiring suction systems and proper ventilation [1].

From the part quality perspective, binder removal poses a challenge, which can lead to binder residue in the material [63], as discussed in Section 2.2. Furthermore, full densification by sintering is difficult due to the low initial green density [63]. HIP can be applied to minimize or eliminate the residual porosity. The debinding and sintering parameters can be optimized by utilization of thermoanalytical techniques such as thermogravimetry (TG). Additionally, the analysis of the gas composition and reaction products by techniques such as Fourier transform infrared spectroscopy (FTIR) can provide valuable information to improve the debinding and sintering process [129].

The BJT technology is a multi-step process that introduces complexity due to the many variables across the process chain. The lack of standards and material qualifications poses challenges for implementing BJT into existing manufacturing value chains. In addition, the high upfront investment in equipment limits widespread adoption [130], which includes printers, curing furnaces, depowdering stations, powder management units and furnaces for debinding and sintering. However, manufacturers of traditional PM parts are early adopters of the BJT technology and can easily take advantage of the associated advantages due to the existing equipment, infrastructure and expertise in sintering [113].

2.7 Applications

Multiple reports on the serial production of BJT components are available, which highlight the advantages of the technology compared to conventional manufacturing and other metal AM technologies such as PBF-LB/M. A selection of industrial BJT applications is presented below.

A successful adoption of the BJT process was demonstrated with a filter solution for circuit breakers made of 316L stainless steel, which are used in industrial plants and marine applications [131]. Sheet metal assemblies were previously used for the filter but led to performance limitations [131]. The use of BJT enabled the reduction of the cabinet size by 20 % to 30 %, which reduces the global footprint of the electrical switchgear and connected material consumption [131].

In addition, redesigning the filter for AM resulted in increased stiffness, enhanced efficiency and the consolidation of the filter mesh and frame into a single block for manufacturing [131]. The PBF-LB/M enabled successful production as well, but part costs were too high for series production due to the complex filter structure [131]. Over 5000 parts were produced in the pilot series with BJT [131].

Another adoption of the BJT process was found in the production of tool inserts for MIM with M2-grade material. The part design with BJT enabled the inclusion of complex conformal cooling channels combined with increased mechanical performance [132]. The wear resistance improved by 50 % to 80 % and the machinability by 40 % compared to conventional wrought M2 material [132].

Applications of BJT were also reported for the automotive industry [133]. An adjustable guide loop of a seatbelt pillar was BJT printed with 17-4 PH stainless steel, which is a safety-relevant part [133]. BJT enabled the consolidation of four separate parts into one component, saving costs and time [133]. In addition, the performance and weight of the part could be optimized [133].

Other emerging markets for BJT include consumer electronics [134], which benefit from cost reduction, design freedom and rapid product development. Metallic watch cases are another prominent example [135], which are widely manufactured by MIM [136]. BJT offers the advantage of customizability for watch production [137]. Jewelry is also a field explored with BJT printing [138].

2.8 Process Parameters

The success of the BJT process is strongly tied to the raw materials and various process parameters across the process chain. Figure 6 provides a rough overview of the powder characteristics, binder properties, process parameters and variables along the manufacturing chain that impact the outcome of the final part. The list is ordered alphabetically and not intending to rank the significance of the various properties and parameters. This overview acts as a general guideline to BJT and is neither extensive nor claims completeness. More details on the different aspects can be found in extensive literature reviews elsewhere [1,5,14,16,26].

The processing atmosphere is one common process parameter encountered for printing, curing, depowdering, debinding and sintering. The role of the processing atmosphere along the BJT process chain will be discussed in Chapter 3.

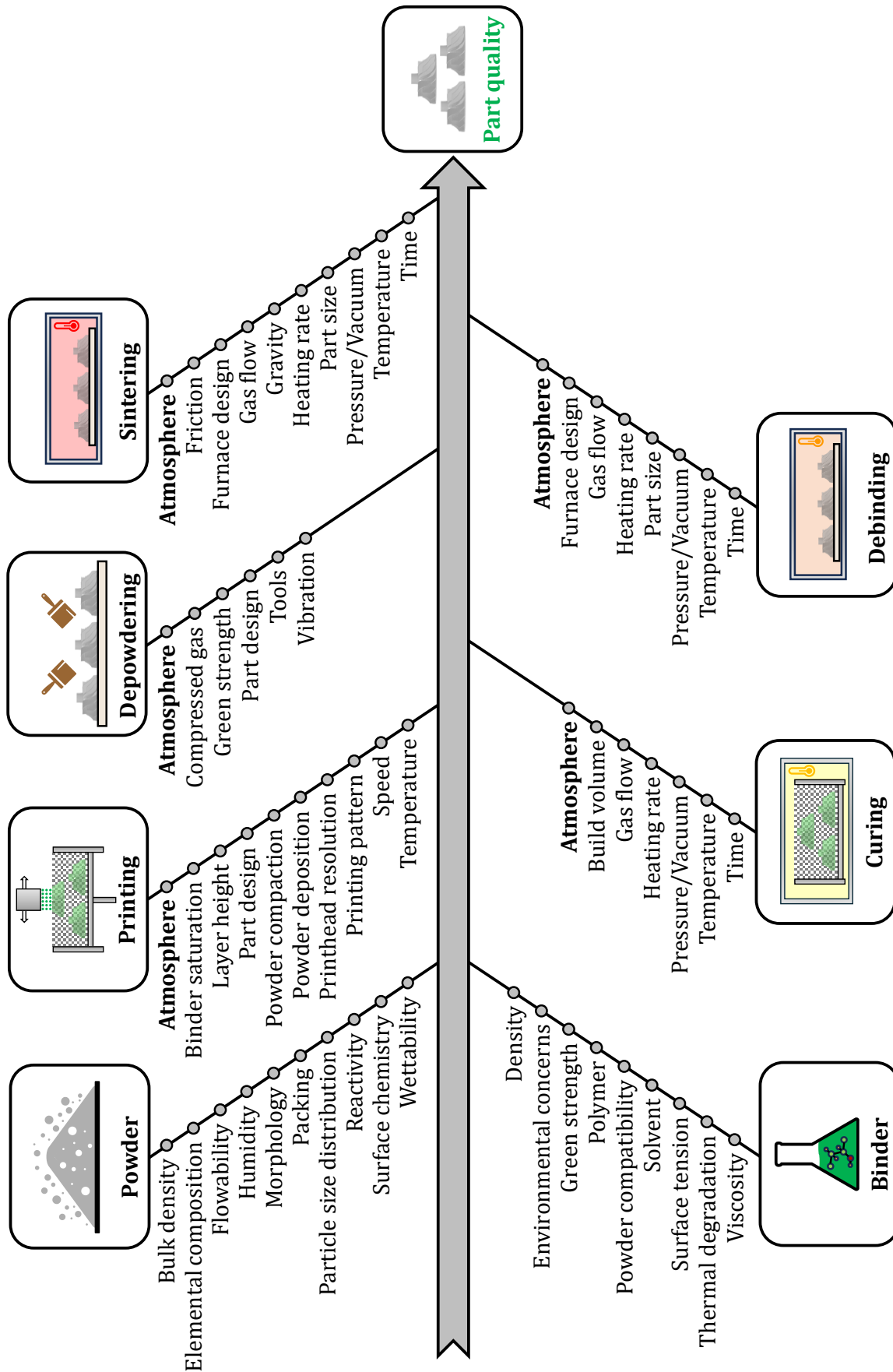


Figure 6: Overview of powder characteristics, binder properties and processing parameters for BJT influencing the final part quality. More details on the various aspects can be found in [1,5,14,16,26].

3 Role of the Processing Atmosphere

The processing atmosphere is an important parameter along the BJT manufacturing chain. The atmosphere becomes increasingly important as the processing temperatures increase. Figure 7 visualizes the potential interactions between the metal powder, binder and atmosphere. The role of the processing atmosphere will be discussed in this chapter for printing, curing, depowdering, debinding and sintering.

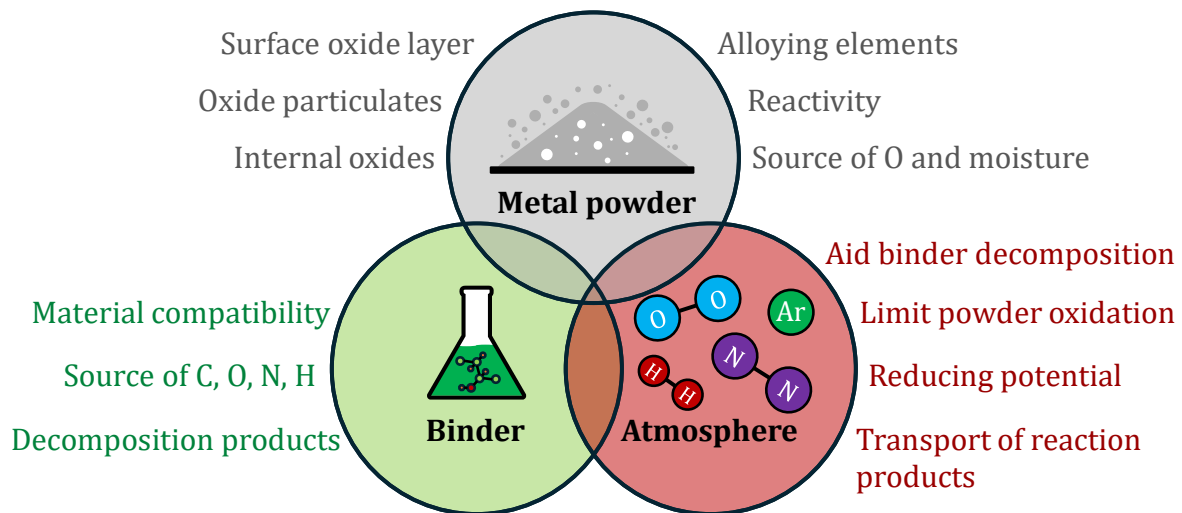


Figure 7: Potential interactions between the powder, binder and processing atmosphere during BJT.

3.1 Printing, Curing & Depowdering Atmospheres

The printing of BJT components is usually conducted at room temperature in ambient conditions. The print chamber is usually not filled with inert gas, as the powder is not exposed to elevated temperatures during printing, which could cause oxidation in ambient air. The reusability of overflow (oversupplied) powder is considered high [1].

Nevertheless, humidity can strongly alter the behavior of the powder during printing. It was shown that 17-4 PH powder picked up humidity from the printing environment, which decreased the powder packing of the green parts after powder reuse [139]. Bidare et al. [139] concluded that a controlled humidity in the build chamber for BJT should be established.

Other studies highlighted the effect of powder drying before printing, which affected the powder cohesion, flowability and quality of the green parts [140,141]. The influence of humidity needs to be especially considered for humid or dry seasons, which can affect the ambient humidity. The humidity can be monitored by sensors and regulated by steaming and gas purging of the print chamber.

In addition, fine metal powder with high reactivity, such as titanium or aluminum, might require an inert printing environment and additional safety features to prevent the creation of explosive atmospheres during printing [142,143]. The same safety considerations apply to depowdering, where powder dust is created. The inertization of

the print chamber with N₂ allows for the safe and controlled printing of fine and reactive metal powder.

During the curing process, the powder is subjected to temperatures between 150°C and 250°C [15]. Curing is typically performed in ambient air, where the powder is prone to oxidation. Barthel et al. [144] demonstrated that curing in air led to powder oxidation for tool steel, which led to increased difficulty of depowdering and lowered the sintered densities. To avoid this problem, curing in inert Ar was adopted [144]. Similarly, Wieland et al. [145] explored the curing of tool steels for BJT with binders that are cured at low temperatures to avoid powder oxidation.

The oxidation of the powder during curing might also affect powder reuse, as the depowdered powder is typically collected and reused for future build jobs. Research on the influence of curing atmospheres and powder reuse is, however, limited.

3.2 Debinding Atmospheres

The composition of the atmosphere influences the reactions with the metal powder and binder during debinding. The atmosphere penetration and chemical reactions might vary between the internal pores of the green part, referred to as the micro-climate [146], and the external surface of the green part. A continuous gas flow during debinding helps to transport the reaction products away from the part.

The debinding atmosphere can be inert, oxidizing or reducing [19,33,147]. Debinding in vacuum or inert atmospheres, such as Ar or N₂, is commonly applied to prevent powder oxidation [19]. However, debinding in inert atmospheres is limited to fragments formed from the binder itself, which leads to carbon residue [19]. Vacuum debinding aids the binder removal but suffers from low heat transfer via radiation at temperatures below 500°C [52,148].

A standard reducing atmosphere for debinding is H₂. Debinding in H₂ can facilitate the removal of binder and carbon [19]. Hydrogen is a small molecule that can easily enter pores and hydrogenate carbon-hydrogen bonds of the binder, aiding the volatilization of the polymeric binder [40,149]. Hydrogen is also known to reduce metal oxides during debinding [40]. However, processing in H₂ atmosphere might be restricted due to safety concerns requiring special furnace design as well as adherence to safety regulations and standards [20].

Oxidizing atmospheres facilitate the binder removal, as binders are oxidized by O₂, CO₂ and H₂O vapor [40]. Debinding in ambient air is a simple and low-cost solution [19]. The thermal degradation of many polymers is enhanced by the presence of O₂ [150]. Debinding in air results in the formation of CO, CO₂ and H₂O vapor due to the presence of O₂ in the atmosphere [19]. However, the powder is prone to oxidation at typical debinding temperatures above 300°C. Powder oxidation hinders subsequent sintering densification and oxide inclusions in sintering necks are detrimental to the mechanical performance of steels [151]. More details on metal oxides and their reactions are provided in Section 3.3.

In summary, the choice of the debinding atmosphere influences the final part quality as it affects reactions with and between the binder and metal powder. The influence of the atmosphere on binder removal was examined for the delubrication of PM steels in several studies [41,152–154]. Systematic studies on debinding atmospheres for BJT components are missing.

3.3 Sintering Atmospheres

The surface characteristics of metal powders must be considered first to understand the importance of the sintering atmosphere. Metal powders used for sintering are typically covered by a layer of metal oxide as well as physically and chemically bonded water (adsorbed water and hydroxides) due to the atomization process and further exposure to air during powder handling [155–157].

Figure 8 shows a sketch of a spherical gas-atomized metal powder, usually used for BJT. The powder surface is typically covered by a homogenous oxide layer and a few particulate oxides and their agglomerates [158,159]. Additionally, internal oxides can be present inside the powder [160–162].

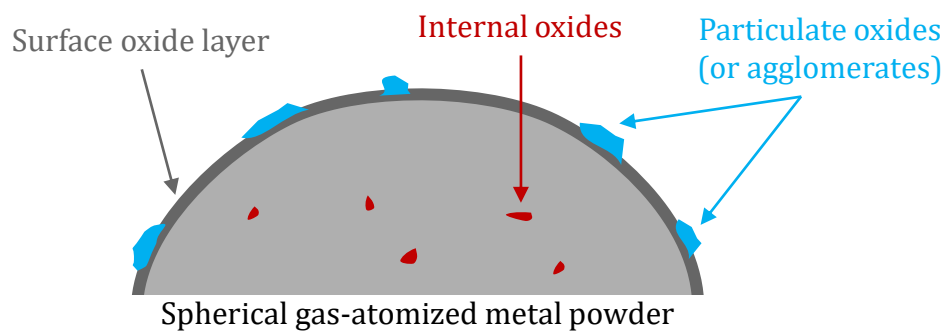


Figure 8: Sketch of a spherical gas-atomized metal powder covered by a homogenous oxide layer with the presence of particulate oxides and their agglomerates as well as internal oxides.

In the case of gas-atomized steel powders, the surface is covered by a thin iron oxide layer with a usual thickness of up to 4 nm [158]. Particulate oxides are up to 20 nm in size and rich in oxygen-sensitive elements [158]. The thickness of the oxide layer, along with the composition and amount of fine particulate oxides and their agglomerates, is determined by the powder alloying content, powder manufacturing process and subsequent powder handling [158,161].

The affinity of various metals to form oxides and their corresponding stability can be understood by considering the thermodynamics of the metal oxide formation. The formation of metal oxides results in a standard Gibbs free energy change ΔG° , which can be described by the standard enthalpy change ΔH° and standard entropy change ΔS° as formulated in Equation (1) [163–165]. T is the absolute temperature in Kelvin, R is the molar gas constant and K is the equilibrium constant of the reaction.

$$\Delta G^\circ = \Delta H^\circ - T \cdot \Delta S^\circ = -R \cdot T \cdot \ln(K) \quad (1)$$

The Ellingham diagram, which plots the ΔG° of oxide formation for different elements over the temperature, is a helpful tool for comparing the stability of various metal oxides [163]. Figure 9 shows the Ellingham diagram for selected metal oxides, which are relevant for 17-4 PH stainless steel. However, the Ellingham diagram does not provide information about the reaction kinetics [166].

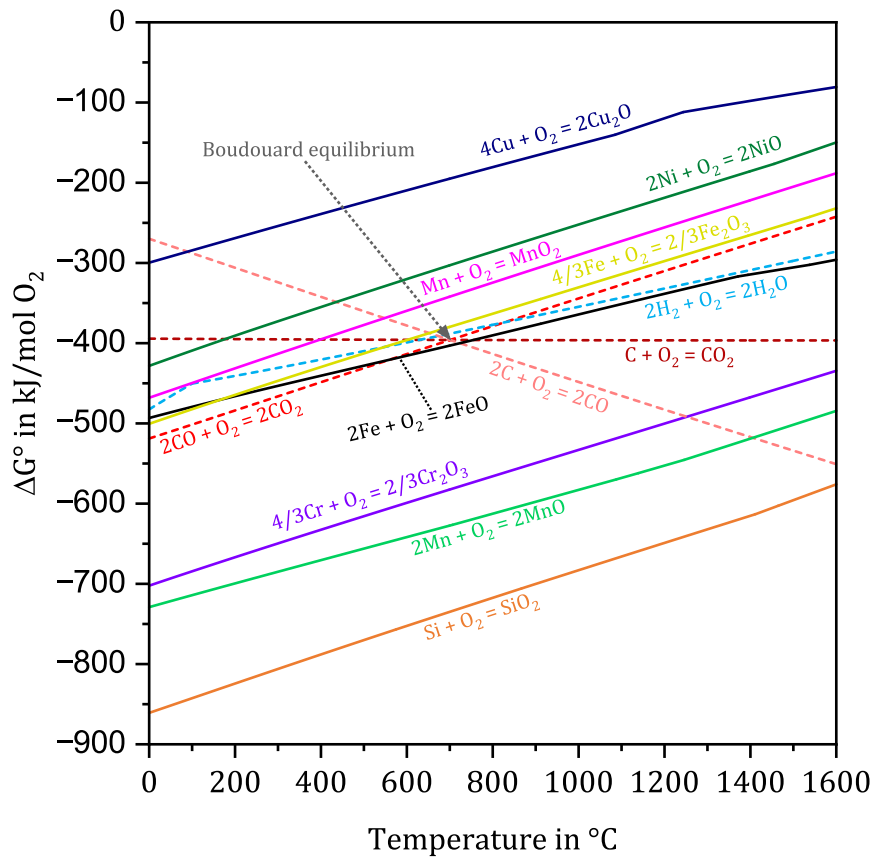


Figure 9: Ellingham diagram for selected elements of 17-4 PH stainless steel indicating oxide stability. Thermodynamic calculations via FactSage Education 8.3 [167] with the database FactPS.

The more negative the standard Gibbs free energy change, the more stable a metal oxide is. Chromium (Cr), manganese (Mn) and silicon (Si) oxides are generally considered thermodynamically stable and are difficult to reduce during sintering [168–170]. In contrast, iron (Fe) oxides are considered easy to reduce during sintering due to their lower thermodynamic stability [171,172]. During sintering, Fe oxides can be reduced, releasing oxygen that can react with elements such as Cr to form more stable oxides, which can inhibit the formation of sintering necks [154,157,173,174].

Surface oxides hinder the mass transport mechanisms of sintering, which retards the sintering neck development [156,162,168,175,176]. Hence, the removal of the surface oxides covering the powder surfaces is critical for successful sintering [177,178]. The inclusion of stable oxides, such as Mn-Cr-Si-rich oxides, inside the interparticle necks is detrimental to the mechanical properties of steels, especially for ductility and fatigue resistance [151,179–182]. The impact toughness of PM steels generally decreases with increasing sintered oxygen content [183].

Therefore, sintering requires protective atmospheres to avoid severe powder oxidation, especially due to the high surface area and reactivity of metal powders [169,184,185]. The sintering atmosphere can serve multiple purposes. Besides protection from oxidation, the sintering atmosphere can reduce surface oxides, sweep away reaction products and carburize or decarburize the material [184–186].

Table 2 classifies common sintering atmosphere constituents for steels according to their reactive tendency but does not universally apply [187]. Whether a gas is inert, oxidizing, reducing, carburizing or decarburizing depends strongly on the material, processing temperatures and partial pressures of the gases.

Table 2: Common atmosphere constituents for sintering of steels and their reactive tendency during processing [187].

Inert gases	Oxidizing gases	Reducing gases	Carburizing gases	Decarburizing
Ar	O ₂	H ₂	CO	H ₂ O
N ₂ *	H ₂ O	CO	C _n H _m	CO ₂
He	CO ₂			O ₂

*N₂ is mainly considered an inert gas but can interact with certain materials such as stainless steel or titanium.

The dissociation of metal oxides, described by Reaction (1), can occur for sintering in an inert atmosphere or vacuum in the absence of reducing agents [178]. The dissociation of metal oxides requires high temperatures and low oxygen partial pressures. An oxygen partial pressure of $\sim 10^{-15}$ bar or lower is necessary at a temperature of 1000°C to provide the thermodynamic conditions for the dissociation of iron oxide [168]. In contrast, dissociation of silicon oxide at 1000°C would require an oxygen partial pressure below 10^{-30} bar, which is unrealistic under industrial sintering conditions [172].

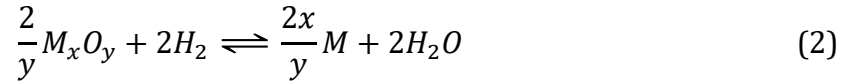


Vacuum sintering under high temperatures and low oxygen partial pressures can achieve the thermodynamic conditions required to reduce some refractory oxides [168]. However, vacuum sintering does not sufficiently reduce stable oxides during the heating stage, when sintering necks start forming [168]. Furthermore, sintering under vacuum can lead to the evaporation of alloying elements at high temperatures, such as chromium, lowering the corrosion resistance due to reduced chromium availability [188].

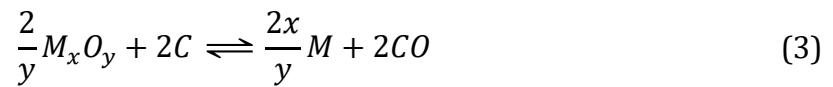
While N₂ is considered inert for many materials, Ar and helium (He) are universal inert gases for sintering. Nitrogen can react with certain materials, such as stainless steels, forming chromium nitrides [188]. Argon is insoluble in solid metals and can be trapped in pores during sintering, which will not close [189]. Helium has excellent heat transport properties but is an expensive option [52].

Hydrogen is a widely adopted sintering atmosphere for the production of high-quality stainless steel parts [188]. Metal oxides can be reduced by H₂ forming H₂O, which is

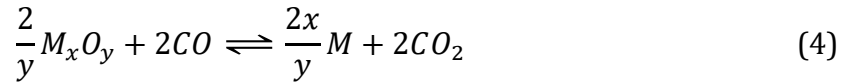
generally described by Reaction (2). Iron oxides can be efficiently removed by H₂ at temperatures of around 400°C [168,177,190]. Hydrogen is, however, flammable and explosive in mixtures with O₂, which requires special furnace designs and procedures for safe operation [20]. In addition, H₂ is considered a costly gas [52,148].



Another common metal oxide reduction mechanism encountered during sintering is the carbothermal reduction by carbon. The carbothermal reduction can be distinguished into direct and indirect carbothermal reduction. Direct carbothermal reduction is defined as the reduction of the metal oxide by carbon, forming CO as the reaction product, as expressed by Reaction (3).



In contrast, indirect carbothermal reduction is described by Reaction (4), where metal oxides are reduced by CO, forming CO₂ as the reaction product. Carbon monoxide can be part of the sintering gas or be formed as a reaction product during sintering.



The direct and indirect carbothermal reduction during sintering are linked by the Boudouard equilibrium presented by Reaction (5). According to the Boudouard equilibrium, the formation of CO is thermodynamically favored at temperatures above ~720°C [190,191]. Hence, the regeneration of CO will be ensured above ~720°C for indirect carbothermal reduction of metal oxides [174].



Whether carbon or hydrogen can reduce a metal oxide at a given temperature can be evaluated based on the ΔG° associated with the oxidation of carbon or hydrogen, as presented in Figure 9. If the ΔG° is more negative than the corresponding oxide formation, then reduction by carbon or H₂ is thermodynamically possible. Therefore, it becomes clear from the Ellingham diagram that H₂ is a stronger reducing agent than carbon or carbon monoxide at low temperatures, while carbon is the strongest reducing agent at high temperatures [169]. Sufficient reduction of stable oxides such as Cr and Mn usually requires high sintering temperatures of 1200°C or higher [183].

In conventional PM, carbon in the form of graphite is added to the green part on purpose to induce carbothermal reduction of stable oxides during sintering [160,191,192]. In the case of BJT, the powder and binder are potential carbon sources. More details on sintering reactions and the efficiency of various reducing agents for the sintering of iron-based materials can be found elsewhere [157,160,160,168,177,190,193].

4 Experimental Methods

The experimental methods used in this thesis are briefly summarized in this chapter. The materials, printer hardware, curing process and depowdering step are shortly described. The strategy for the research on powder reuse and curing atmospheres is introduced. The thermal processing of the green samples is explained depending on the study. In addition, different methods of material characterization are outlined. More details on methods, parameters and number of experiments can be found in the appended Papers.

4.1 Materials & Printing

All green parts were printed with N₂-atomized 17-4 PH stainless steel powder (17-4 PH, Desktop Metal Inc., USA). The particle size distribution (PSD) was comparable for all experiments with a D_{10} (10th percentile) of $\sim 7 \mu\text{m}$, a D_{50} (50th percentile) of $\sim 15 \mu\text{m}$ and a D_{90} (90th percentile) of $\sim 28 \mu\text{m}$. The elemental composition of all powder batches used for printing fulfilled the specifications of the MPIF35/ASTM B883 – 24 standards for MIM [97,98], which are listed in Table 1. A water-based binder (SPJ-04, Desktop Metal Inc., USA) containing solvents and a thermosetting polymer was used for printing.

The printer hardware (Production System™ P-1, Desktop Metal Inc., USA) utilized for BJT printing is visualized in Figure 10. The build box, surrounded by an overflow tray for oversupplied powder, had a build volume of $200 \times 100 \times 40 \text{ mm}^3$. The BJT printer included several distinct features compared to most commercially available BJT platforms. Unlike most BJT printers, the build box is moved during printing, while the powder dispensing, powder compaction, steamer and printhead modules are stationary.

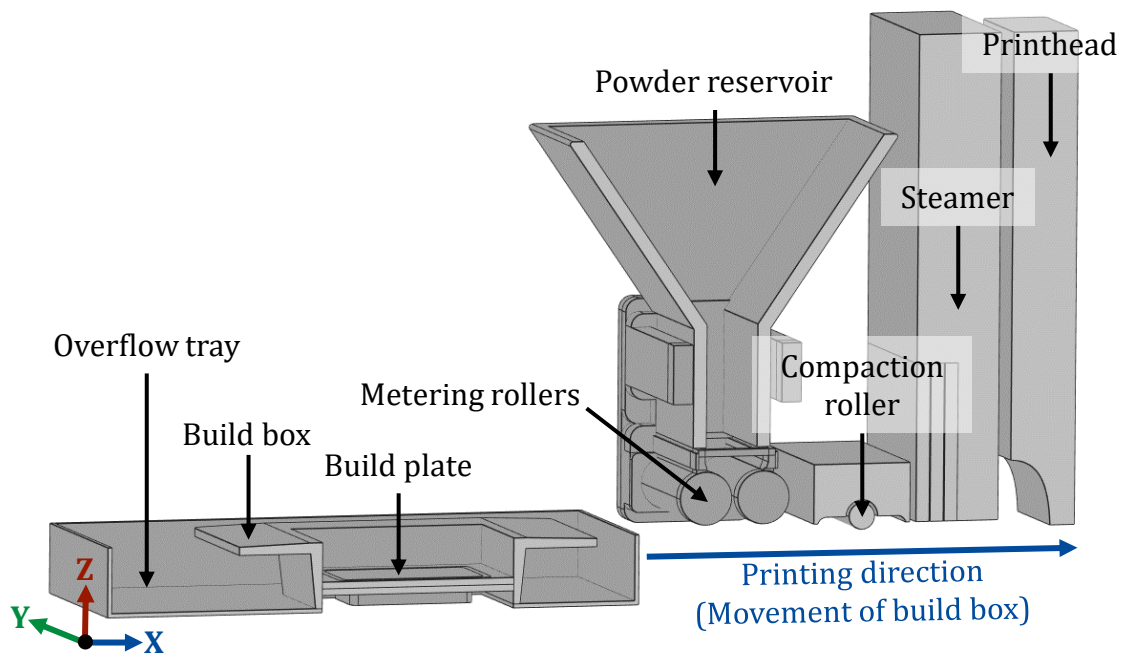


Figure 10: Sectioned sketch of the printing modules of the Production System™ P-1 (not to scale), excluding camera and light sources for print monitoring.

The powder is deposited by metering rollers from the powder reservoir. The compaction roller compacts the deposited powder layer. A steamer module is situated between the powder compaction roller and printhead, which steams each deposited powder layer to prevent powder ejecta during printing [194,195]. The printer includes sensors to control the humidity and O₂ content in the build chamber by purging with N₂ gas during printing.

In addition, the printer contains a camera and light sources to monitor the quality of the printed layers, which are not displayed in Figure 10. The powder and binder deposition occurs in a single pass of the build box. After printing in a single pass, the build box returns to the initial position depicted in Figure 10 and starts printing the next layer. The layer thickness was set to 65 μm for all build jobs in this thesis.

The as-received powder oxygen content was ~1200 ppm due to powder conditioning by oxidation after the powder atomization to meet the flowability requirements for printing. Powder oxidation can reduce the powder cohesion and increase the flowability [196].

Cuboid green parts with dimensions of 10 x 10 x 10 mm³ were printed in Papers I, III, IV, V and VI. Additionally, cylinders with a diameter of 2.9 mm and a height of 11.9 mm were printed for chemical analysis in Papers V and VI. Green samples with dimensions of 7.5 x 7.5 x 7.5 mm³ were printed for thermogravimetric analysis in Paper VII. The printing and binder saturation parameters are mentioned in the corresponding Papers.

The slicing software (Fabricate MFG™, Desktop Metal Inc., USA) defined binder printing patterns with specific voids in the green parts absent of binder, which is termed dithering. Dithering allows faster gas escape during printing as the powder bed is wetted [195]. In addition, dithering reduces the binder content, decreasing the risk of binder residue in the material [197].

The binder printing patterns are visualized in Figure 11 for printing a standard green sample. The first few layers were printed with homogenous binder saturation, as typical for BJT printing. However, most layers were printed with dithering, slicing the part into distinct regions: shell, inner shell and inner region. The top layers of the part were again considered shell regions.

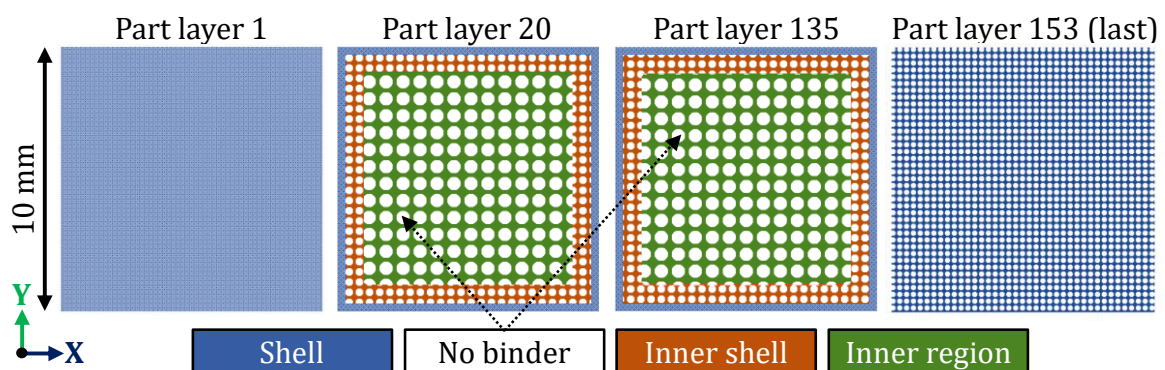


Figure 11: Binder printing patterns (dithering) of selected layers for printing of a standard green sample with distinct slicing regions: shell, inner shell and inner shell region.

Printing hollow (shelled) part geometries can even further minimize the binder content in the green part by adjusting the computer-aided design (CAD) of the part. Only the shell of the green part with a defined thickness is printed, which encloses a binder-free core consisting of loosely packed powder. The shell printing approach was utilized in Paper III for cuboid samples with $10 \times 10 \times 10 \text{ mm}^3$. Green parts with different shell thicknesses of 0.46 mm, 1.03 mm, 1.85 mm and 5.00 mm were printed, which corresponded to shell volumes of 25 %, 50 %, 75 % and 100 %. The corresponding printing patterns are displayed in Figure 12. Note that 100 % shell volume corresponded to the standard printing process, as depicted in Figure 11.

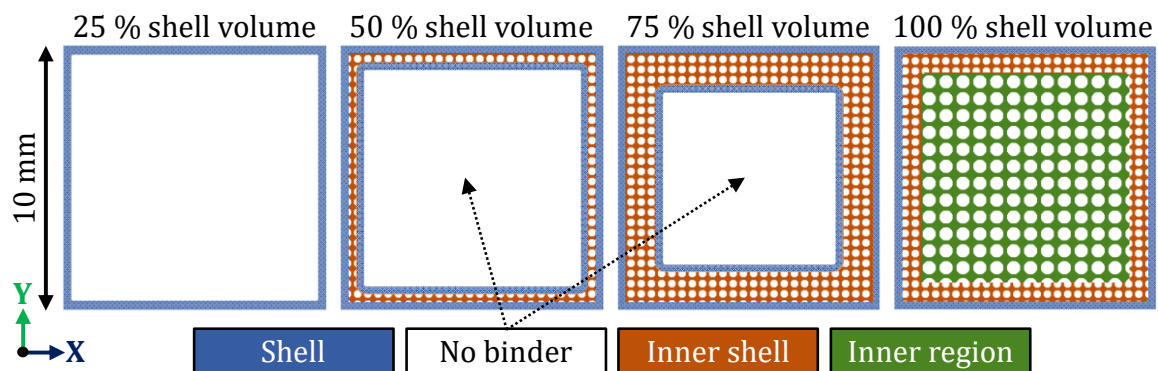


Figure 12: Binder printing pattern for shell printing of cuboid samples with 25 %, 50 %, 75 % and 100 % shell volume defined by the wall thicknesses set during CAD design of the parts.

4.2 Curing & Depowdering

The build box was placed after printing in a furnace with forced air-convection (TR 120 LS, Nabertherm GmbH, Germany) for curing. The curing process was conducted at 200°C for 4 h with a heating rate of $1.5^\circ\text{C}/\text{min}$ for all build jobs. After curing, the green parts were separated from the powder bed in the printing chamber under N_2 gas utilizing brushes and tweezers. Compressed gas or air was subsequently used to remove the remaining powder from the green parts.

4.3 Powder Reuse & Curing Atmosphere

The influence of powder reuse and curing atmosphere was studied in Paper I. The 17-4 PH powder was classified into virgin, overflow and depowdered powder. The virgin powder was introduced for printing and the generated overflow (oversupplied) powder was continuously reused in the printer for five consecutive build jobs. The five build boxes were simultaneously placed into the curing furnace at 200°C for 4 h under ambient air. The obtained depowdered powder from the depowdering of the green parts was sieved and reintroduced into the printer for the next set of five consecutive build jobs. This procedure was repeated until a total of 20 build jobs were printed, which corresponded to four curing cycles in total. More details are provided in Paper I.

The influence of the curing atmosphere was compared by conditioning virgin powder in ambient air and inert Ar at 200°C for 4 h. Furthermore, empty build jobs were performed

with virgin powder and the same powder after conditioning in ambient air to assess the influence on the powder packing in the build box.

4.4 Debinding & Sintering

The debinding and sintering trials were conducted in a laboratory tube furnace, dilatometer or thermogravimetric analyzer. The used process parameters, especially atmospheres, are summarized in this section. More details on the thermal processing can be found in the appended Papers.

4.4.1 Tube Furnace

A laboratory tube furnace with a steel muffle tube was used for debinding and sintering. The gas flow during debinding and sintering was set to 4 l/min for all gases. A thermocouple was placed close to the samples inside the furnace to measure the actual temperature with a resolution of 0.1°C. The O₂ concentration of the off-gas at the furnace outlet was measured through an O₂ monitoring system (Hydroflex, Linde GmbH, Germany) to confirm a high-purity atmosphere.

The laboratory tube furnace was used for the debinding and sintering trials in Papers V and VI. A prior debinding step, recommended by the printer manufacturer, was conducted in Paper V at 300°C for 2 h under various debinding gas mixes with a heating rate of 3°C/min. The obtained brown samples were then sintered in Paper VI at a peak temperature of 1300°C with a 2 h dwell. Natural cooling took place in the furnace after the prior debinding or sintering. The combinations of studied debinding and sintering atmospheres are listed in Table 3.

Table 3: Combinations of debinding and sintering atmospheres used for the laboratory tube furnace.

Debinding atmosphere at 300°C for 2 h	Sintering atmosphere at 1300°C for 2 h
Ar	Ar
Ar + 1 vol.% O ₂	Ar
Ar + 3 vol.% O ₂	Ar
Ar + 4 vol.% O ₂ + 5 vol.% CO ₂	Ar
Ar + 8 vol.% O ₂	Ar
N ₂ + 20 vol.% O ₂	Ar

4.4.2 Dilatometry

Dilatometry was applied to measure the dimensional changes over the temperature and time during sintering with a resolution of 0.01 µm. A negative dimensional change corresponded to part shrinkage. The dilatometer (L75HS1600C, Linseis Messgeräte GmbH, Germany) contained a horizontal pushrod and a ceramic gas capillary close to the sample. The gas flow through the capillary was 300 ml/min and the purge gas flow was 100 ml/min. The processing atmosphere was either Ar or H₂. The pushrod force was set to 300 mN and the measuring frequency was set to 60 Hz.

Sintering was conducted at 1300°C for 1 h with a controlled heating and cooling rate of 5°C/min. The temperature was measured and regulated via an encapsulated thermocouple close to the sample with a resolution of 0.01°C. For Paper III, the sintering shrinkage was measured in the X-direction to compare the influence of shell printing on sintering densification, which is exemplified in Figure 13. The dilatometry experiments were conducted in the X-, Y- and Z-directions for Papers I and IV to study sintering densification and shrinkage anisotropy.

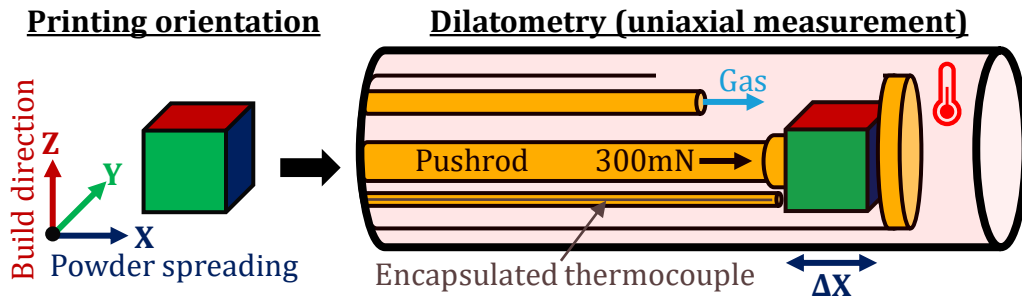


Figure 13: Sketch of the uniaxial measurement during dilatometry depicting a measurement of the dimensional change in the X-direction (powder spreading direction).

The shrinkage anisotropy can be expressed by anisotropic factors, which describe the ratio of the shrinkage ε in the three spatial directions [124,198]. The anisotropic factors K_1 , K_2 and K_3 are defined in Equations (2), (3) and (4) for ratios of the shrinkages in X-direction (ε_X), Y-direction (ε_Y) and Z-direction (ε_Z).

$$K_1 = \frac{\varepsilon_Y}{\varepsilon_X} \quad (2)$$

$$K_2 = \frac{\varepsilon_Z}{\varepsilon_Y} \quad (3)$$

$$K_3 = \frac{\varepsilon_Z}{\varepsilon_X} \quad (4)$$

4.4.3 Thermogravimetry

Thermogravimetry (TG) was utilized in Paper VII to measure the mass changes during debinding and sintering in various atmospheres. The resolution of the measurements was 0.025 μg . Virgin powder and green samples with a mass of ~ 2 g were placed into the thermogravimetric analyzer (STA 449 F1 Jupiter, NETZSCH-Gerätebau GmbH, Germany). The protective gas flow was set to 20 ml/min, while the purge gas flow was fixed at 100 ml/min for all measurements. The thermocouple was selected according to the studied atmosphere.

Virgin powder and green parts were heated up to 700°C with 10°C/min to analyze the impact of the debinding atmosphere on binder removal and powder oxidation. The influence of a prior debinding step at 300°C for 2 h on the subsequent sintering was investigated for various debinding and sintering atmosphere combinations. The investigated combinations of debinding and sintering atmospheres are summarized in Table 4.

Table 4: Debinding and sintering atmosphere combinations for TG experiments.

Debinding atmospheres (700°C, 5 min)	Atmosphere combinations for debinding and sintering	
	Debinding (300°C, 2 h)	Sintering (1300°C, 1 h)
Ar	Ar	H ₂
H ₂	H ₂	H ₂
Ar + 1 vol.% O ₂	Ar + 1 vol.% O ₂	H ₂
Ar + 3 vol.% O ₂	Ar + 1 vol.% O ₂	Ar
Ar + 4 vol.% O ₂ + 5 vol.% CO ₂	Ar + 1 vol.% O ₂	N ₂
Ar + 8 vol.% O ₂	Ar + 1 vol.% O ₂	Vacuum
N ₂ + 20 vol.% O ₂	N ₂ + 20 vol.% O ₂	H ₂

4.5 Material Characterization

Several material characterization techniques were used to analyze the samples in this thesis. The metal powder properties were determined by several methods. Green parts, brown parts and sintered parts were analyzed for density and chemistry. The microstructure and microhardness of sintered specimens were investigated. More information on sampling and the number of measurements is presented in the appended Papers.

4.5.1 Powder Characterization

The PSD of the powders was analyzed via dynamic imaging analysis (CAMSIZER X2, Microtrac Retsch GmbH, Germany). Inductively coupled plasma optical emission spectroscopy (ICP-OES) and X-ray fluorescence (XRF) spectroscopy were used to determine the elemental composition of the virgin powder. The humidity content was identified by Karl Fischer titration (C30S Compact KF Coulometer, Mettler-Toledo GmbH, Germany). The powder density was obtained by helium pycnometry (AccuPyc 1330, Micromeritics Instrument Corporation, USA).

The powder flowability was tested in a rotating drum analyzer (Revolution Powder Analyzer 2015, Mercury Scientific Inc., USA). The same device was used for powder packing tests. All trials were conducted with 100 ml of powder. The flowability tests provided avalanche energies and dynamic densities. The packing tests measured apparent and tap densities.

Scanning electron microscopy (SEM) was used to investigate the powder. The SEM (Gemini 450 SEM, Carl Zeiss Microscopy Deutschland GmbH, Germany) was equipped with a field emission gun. X-ray photoelectron spectroscopy (XPS) was used to analyze the powder surface chemistry and oxide layer thickness. The XPS (PHI 5000 VersaProbe III, ULVAC-PHI Inc., Japan/USA) was equipped with an Al K α source.

4.5.2 Elemental Analysis

The carbon, oxygen, nitrogen and hydrogen contents of the powder, green parts, brown parts and sintered specimens were determined. The carbon content was obtained via a carbon/sulfur analyzer (CS 2000, ELTRA GmbH, Germany). The inert gas fusion method (ONH836, LECO Corporation, USA) was utilized to measure the oxygen, nitrogen and hydrogen contents. The sampling for elemental analysis is described in the appended Papers.

4.5.3 Density Determination

The density of green and sintered parts was determined by their mass and volume. A precision scale with a resolution of 0.001 g was used to measure the weight. The dimensions in the X-, Y- and Z-directions were determined through a micrometer screw gauge with a resolution of 0.001 mm. The dimensions were used to calculate the sample volume. In addition, the shrinkage from green to sintered samples could be calculated. Archimedes' principle was applied as a second method to measure the sintered densities.

4.5.4 Microstructural Investigation

Sintered specimens were cut, hot-embedded, ground and polished for microstructural analysis by light optical microscopy (LOM). Stitched images of the whole cross-sections were taken via LOM (VHX-6000, Keyence, Germany). The image analysis software Fiji (open-source) was used to quantify the porosity via the thresholding method. Samples were etched with Kalling's reagent to reveal microstructural features by LOM.

Electron backscatter diffraction (EBSD) was performed to map the phase composition of 17-4 PH after sintering. An EBSD detector (Nordlys II, Oxford Instruments, UK) was used in an SEM (LEO Gemini 1550, Carl Zeiss AG, Germany) to identify the crystal structure and grain orientations. The accelerating voltage was 20 kV with a magnification of 350X and a step size of 0.4 μm . The EBSD images were used to quantify the fractions of δ -ferrite in the microstructure by using the Trainable Weka Segmentation plugin of the image analysis software Fiji (open-source).

4.5.5 Microhardness Testing

Microhardness testing (DuraScan 10, EMCO-TEST Prüfmaschinen GmbH, Germany) was performed with a load of 0.98 N (HV0.1). Indents were placed in pore-free areas to determine differences in the microstructure.

4.6 Thermodynamic Simulations

Thermodynamic calculations (ThermoCalc 2019b, Thermo-Calc Software AB, Sweden) were applied to calculate the quasi-binary Fe-C phase diagram of 17-4 PH using the database TCFE9 Steels/Fe-alloys. In addition, the phase fractions at 1300°C were calculated for varying carbon content.

Thermodynamic and kinetics simulations (JMatPro 14.0, Sente Software Ltd., United Kingdom) were further conducted to predict the phase fractions of austenite, ferrite and martensite during cooling of 17-4 PH for 0.02 wt.%, 0.10 wt.% and 0.20 wt.% carbon.

5 Summary of Results

The previously formulated research questions are addressed in this chapter by summarizing the results from the appended Papers I to VII. This chapter is divided into three sections according to the three posed research questions. Section 5.1 summarizes Papers I and II, highlighting the influence of powder reuse and curing atmosphere on powder characteristics, green parts and sintering densification. Section 5.2 provides a summary of Papers III and IV, demonstrating the impact of the binder and its distribution on green and sintered part quality. Section 5.3 highlights the insights of Papers V, VI and VII, emphasizing the effect of the debinding atmosphere on sintered part quality.

5.1 Influence of curing atmosphere and powder reuse on powder characteristics, green parts and sintering densification

Figure 14 depicts the green density and powder oxygen content over 20 build jobs reusing the same 17-4 PH powder. The direct reuse of overflow powder for build jobs 1–5 led to consistent green densities and printing accuracies (see Paper I). The slight standard deviations are based on variations in the powder bed density. The oxygen content of the overflow powder remained stable for five consecutive build jobs. The oxygen content of the overflow powder remained stable for five consecutive build jobs.

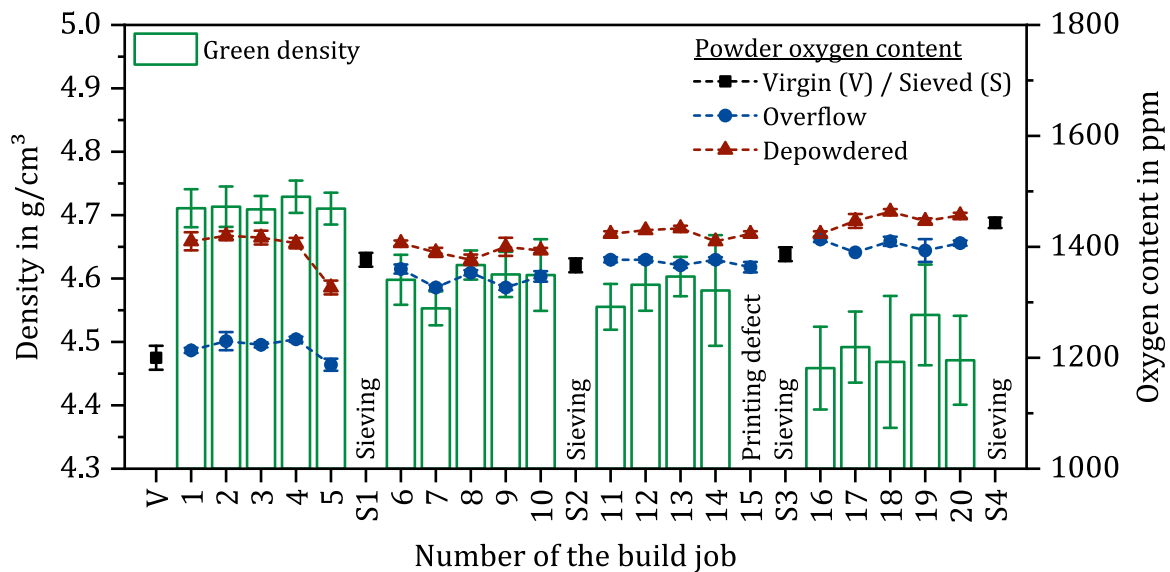


Figure 14: Green densities for build jobs 1–20 and powder oxygen contents of virgin, overflow, depowdered and sieved (S1–S4) powder (Results from Paper I).

A significant reduction of $\sim 0.11 \text{ g/cm}^3$ in green densities was measured between build jobs 1–5 and 6–10, where the powder was subjected to curing and sieving between build jobs 5 and 6. This notable decrease in green densities correlated with the highest powder oxygen pickup by 15 % in the depowdered powder, which was caused by oxidation during curing at 200°C for 4 h in ambient air.

Figure 15 demonstrates the direct impact of the curing process and atmosphere on powder rheology. The three measurements per sample condition (a, b, c) demonstrated reproducibility of the results. The virgin powder conditioned in ambient air at 200°C for 4 h resulted in considerably decreased avalanche energies and dynamic densities but higher tap densities compared to the virgin powder. In contrast, curing in an inert Ar atmosphere led to powder oxygen contents, avalanche energies and dynamic densities similar to those of the virgin powder.

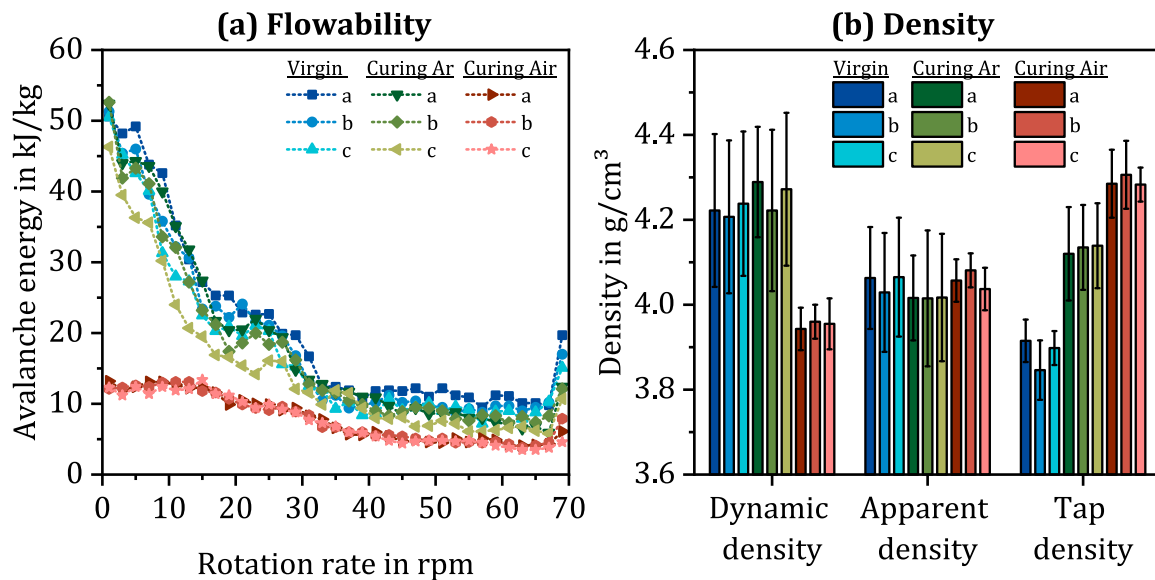


Figure 15: Multiflow and packing tests showing (a) powder flowability and (b) powder densities for different powder conditions: virgin, after curing in Ar and after curing in air (Results from Paper I).

The change in powder characteristics caused by curing in ambient air was identified as the leading cause of the reduced green densities. This was confirmed by printing empty build jobs, in which the powder packing decreased by 0.34 g/cm^3 compared to the virgin powder due to conditioning the powder in ambient air at 200°C for 4 h. The powder oxidation was assumed to affect the complex interaction of the powder with the metering rollers, compaction roller, binder and the powder itself, leading to lower powder packing.

Figure 16 shows SEM images of the virgin and reused powder after 20 build jobs and four curing cycles, where differences between the powder conditions were difficult to identify. The powder was mostly spherical with the presence of satellites. Nano-sized oxide particulates were observed via SEM but were difficult to distinguish due to the presence of a thick oxide layer.

The normalized oxygen (O1s) intensities over the etch depths from XPS analysis are compared in Figure 16 for the virgin powder and for the first, second, third and fourth curing cycles. The oxide layer thickness was determined at a normalized intensity of 0.65 for each powder condition. XPS analysis estimated the growth of the powder oxide layer thickness from $\sim 7.1 \text{ nm}$ to $\sim 9.5 \text{ nm}$ after the first curing cycle, while it remained comparable for the following curing cycles.

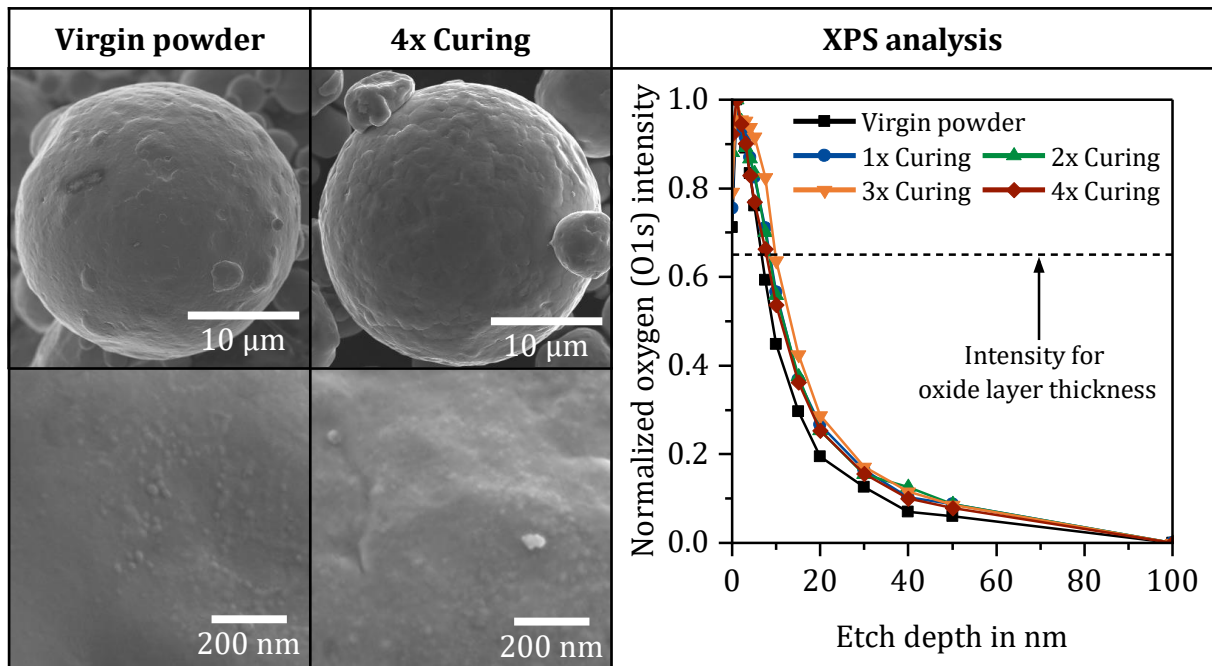


Figure 16: SEM images of virgin powder and powder after four curing cycles along with XPS analysis of normalized oxygen intensities (O1s) for virgin powder and four curing cycles (Results from Paper II).

After 20 consecutive build jobs, the powder flowability and tap density increased while the dynamic density reduced compared to the virgin powder, similar to the powder conditioned in ambient air at 200°C for 4 h (see Paper I). The PSD of the powder did not change notably over 20 build jobs, while the humidity increased slightly from 44 ± 3 ppm to 54 ± 2 ppm. The green densities declined from 4.71 ± 0.03 g/cm³ to 4.47 ± 0.07 g/cm³ after 20 build jobs. The increasing standard deviations in green densities and green part dimensions indicated reduced process robustness due to powder reuse and curing in ambient air.

For simplicity, the green parts printed with virgin powder will be referred to as virgin samples (build jobs 1–5), while the samples printed with reused powder will be referred to as reused samples (build jobs 16–20).

Dilatometry under H₂ atmosphere in Paper I revealed that the lower initial green densities of the reused samples led to higher shrinkages than for the virgin samples under the same sintering conditions. The shrinkage from virgin to reused samples increased considerably in the powder spreading direction ($\Delta\epsilon_x=1.1\%$) and compaction roller axis direction ($\Delta\epsilon_y=1.8\%$), whereas the lowest increase was found for the build direction ($\Delta\epsilon_z=0.6\%$).

The unequal increase in the shrinkages led to a change in the sintering anisotropy for reused samples compared to the virgin samples. The higher shrinkages and associated changes in shrinkage anisotropy indicated that the porosity in reused green samples increased, compared to virgin samples, primarily in the powder spreading direction and compaction roller axis direction rather than in the build direction.

The sintered densities were slightly higher for virgin samples ($99.2 \pm 0.1 \%$) than for reused samples ($98.9 \pm 0.2 \%$) after sintering in H_2 . Therefore, higher shrinkages could nearly fully compensate for the lower initial green densities under the same sintering conditions. The obtained hardness and sintered chemistry were comparable between the virgin and reused samples processed in H_2 . A similar influence of the lower green densities was observed for sintering in Ar, but the sintering shrinkages were much lower compared to the results when processing in H_2 . The shrinkages of the reused samples increased only slightly compared to the virgin samples, leading to notably lower sintered densities for the reused samples. Additional information can be found in Paper I.

5.2 Impact of binder content and distribution on powder packing, sintering densification, microstructure gradients and shrinkage anisotropy

Cuboid samples with 25 %, 50 %, 75 % and 100 % shell volume were printed. The green density increased with increasing shell volume from $4.46 \pm 0.01 \text{ g/cm}^3$ for 25 % shell volume to $4.82 \pm 0.04 \text{ g/cm}^3$ for 100 % shell volume. The higher density was primarily linked to higher powder packing in the green part, as the binder only accounted for $\sim 11 \%$ of the mass gain.

The increase in green density followed a nearly linear correlation between density and shell volume. This led to the assumption that the powder packing was higher in the shell than in the core, which was attributed to binder-induced particle rearrangement locally in the shell region.

Samples with 25 %, 50 %, 75 % and 100 % shell volume were debinded and sintered in a dilatometer at 1300°C for 1 h under inert Ar. The measured dilatometric curves in the X-direction are displayed in Figure 17. The final sintering shrinkage reduced significantly from 15.15 % for 25 % shell volume to 10.85 % for 100 % shell volume under processing in Ar, reducing the sintered density from $99.3 \pm 0.2 \%$ to $93.4 \pm 1.8 \%$.

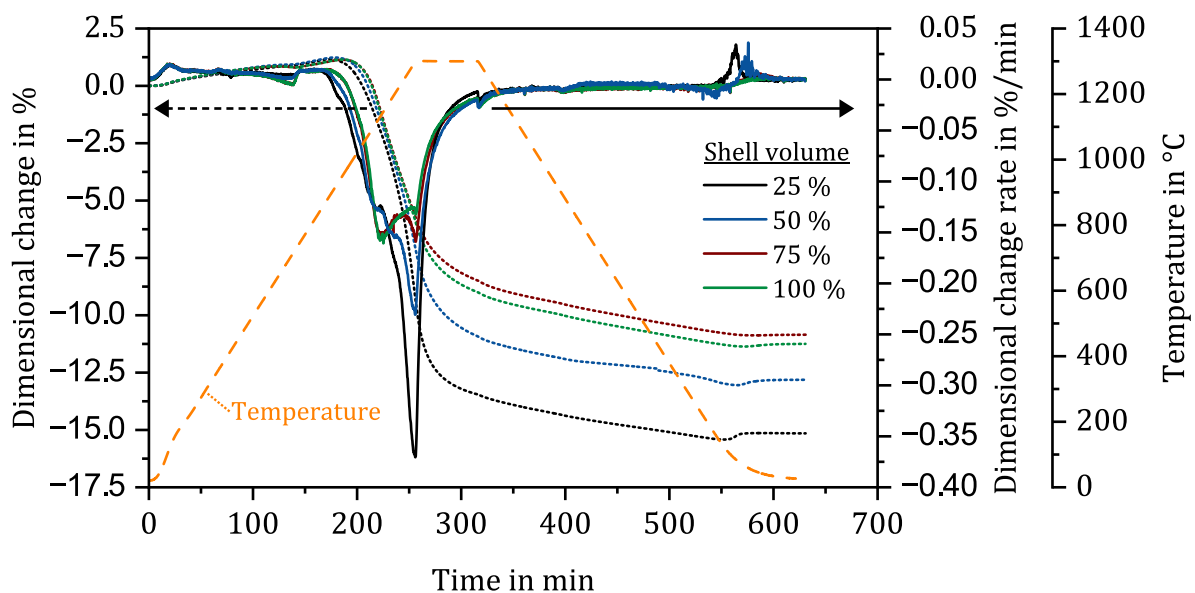


Figure 17: Dilatometric curves of green parts with 25 %, 50 %, 75 % and 100 % shell volume sintered under Ar atmosphere at 1300°C for 1 h (Results from Paper III).

A rapid surge in the shrinkage rate was observed at between 1162°C and 1300°C for 25 % shell volume, which was associated with the formation of δ -ferrite. The formation of δ -ferrite enhances sintering densification because of the higher self-diffusivity in the bcc crystal structure of δ -ferrite than in the fcc crystal structure of γ -austenite [104,105]. Comparable peaks in the shrinkage rate were found for 50 % and 75 % shell volume, but the intensity decreased with increasing shell volume. For 100 % shell volume, the formation of δ -ferrite was only slightly indicated.

The formation of δ -ferrite during sintering depends on the carbon content since carbon stabilizes γ -austenite [199]. The sintered carbon content was 289 ppm for 25 % shell volume, close to the virgin powder content of 205 ppm. In contrast, a sintered carbon content of 994 ppm was measured for 100% shell volume, indicating low debinding efficiency under inert Ar with increasing shell volume. Thermodynamic calculations in Paper III demonstrated that the δ -ferrite fraction during sintering decreases as the carbon content increases.

The sintered oxygen content decreased from 745 ppm for 25 % shell volume to 63 ppm for 100 % shell volume. These values were both below the virgin powder content of 1163 ppm. The decrease in oxygen content was caused by the carbothermal reduction of the metal oxides [160,177], which was enhanced by increased carbon residue from the binder with increasing shell volume.

Due to the shell printing, the carbon-rich binder residue was not distributed uniformly during sintering, leading to microstructure gradients between the core and the shell. Figure 18 depicts the differences in the microstructure by LOM images (XY-plane) between the core and fringe of the samples sintered in Ar.

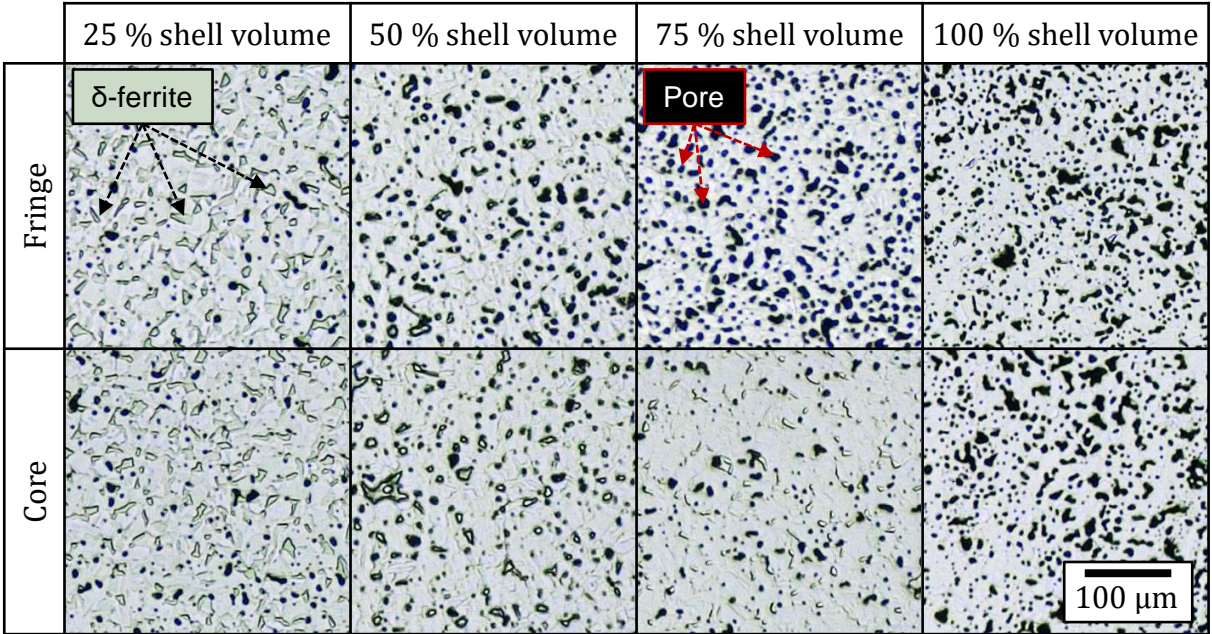


Figure 18: As-sintered microstructure (XY-plane) in the core and fringe of green parts with 25 %, 50 %, 75 % and 100 % shell volume processed under Ar atmosphere (Results from Paper III).

For 25 % shell volume, a high fraction of δ -ferrite was apparent in the core and fringe of the sample. In contrast, no δ -ferrite was found in the cross-section for 100 % shell volume. For 75 % shell volume, slight fractions of δ -ferrite were identified in the core but none in the fringe. For 50 % shell volume, only minor fractions of δ -ferrite were present in the fringe, while a higher fraction was located in the core.

These gradients in the δ -ferrite fractions between the shell and core caused gradients in the sintered porosity since δ -ferrite enhanced the sintering densification. Figure 19 highlights the porosity distribution of samples with 25 %, 50 %, 75 % and 100 % shell volume sintered in Ar. The most significant porosity gradients were present for 75 % and 50 % shell volume, following the division into the core and shell region. The carbon pickup inhibited the formation of δ -ferrite in the shell, while higher fractions could form in the binder-free core. The porosity gradient for 100 % shell volume is potentially linked to a debinding gradient due to the gas flow along the X-direction, as displayed in Figure 13.

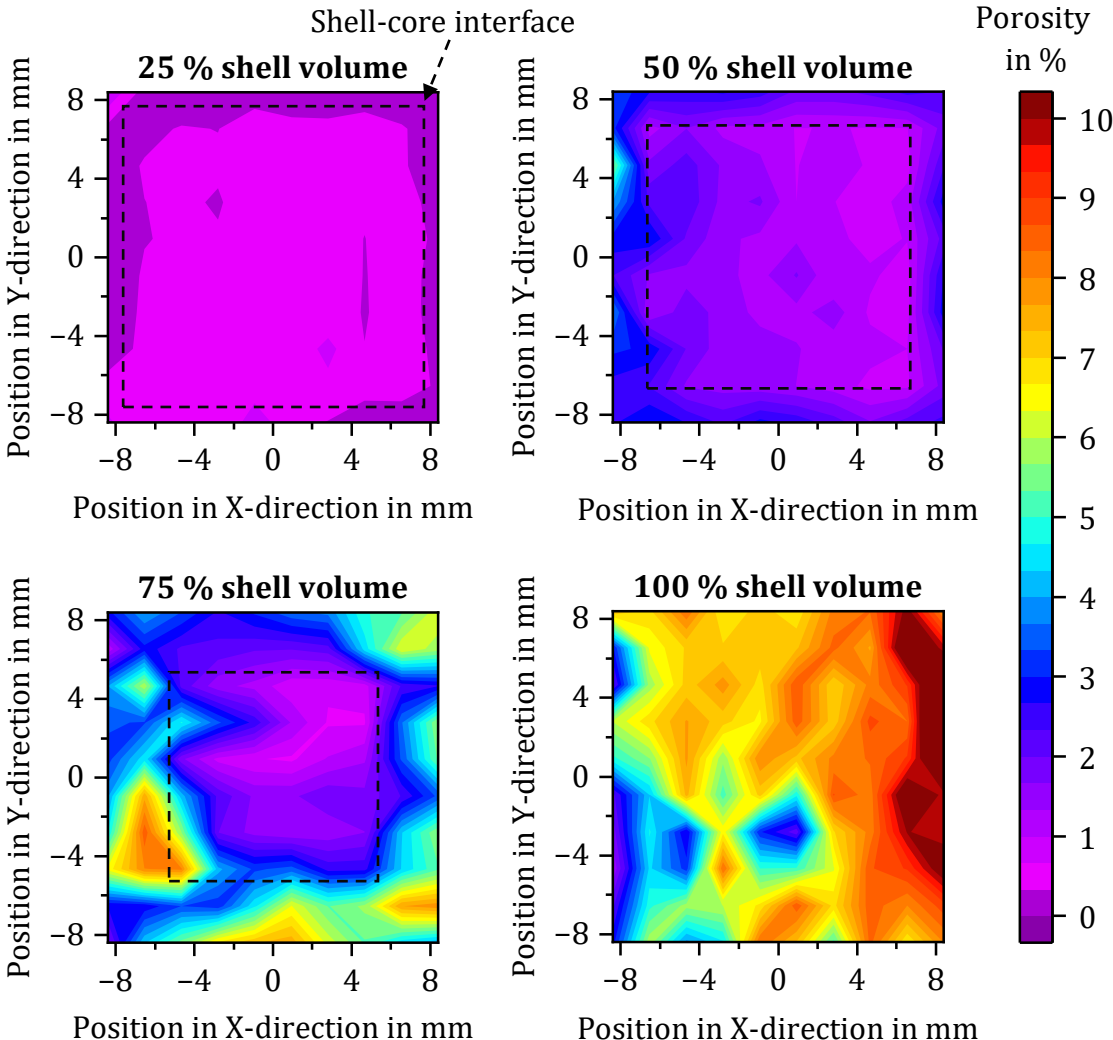


Figure 19: Porosity distribution for 25 %, 50 %, 75 % and 100 % shell volume after sintering at 1300°C for 1 h under Ar atmosphere (Results from Paper III).

While the carbon-rich binder residue influenced the phase transformations associated with δ -ferrite during sintering, the carbon pickup in 17-4 PH also affected the phase transformations during the cooling stage after sintering, leading to gradients in the microhardness (see Paper III). The core exhibited higher microhardness values than the shell. This was connected to the stabilization of the austenitic phase by carbon in the shell, which resulted in high fractions of retained austenite that did not transform into martensite during cooling.

The EBSD measurements in Paper III confirmed high fractions of retained austenite (fcc) for 100 % shell volume debinded and sintered in Ar, leading to a low microhardness of 176 ± 21 HV0.1. In contrast, the retained austenite fraction for 25 % shell volume sintered in Ar was negligible. For 25 % shell volume, the EBSD analysis indicated the presence of martensite and δ -ferrite (bcc), which led to a high microhardness of 307 ± 27 HV0.1.

In contrast, processing in H_2 resulted in efficient binder and oxide removal for all shell volumes (see Paper III). High fractions of δ -ferrite formed during sintering, leading to high sintering densification. The sintering shrinkage under H_2 decreased from 25 % to 100 % shell volume, primarily due to the increasing powder packing in the green parts. The resulting sintered densities were comparable between 99.7 ± 0.1 % and 99.9 ± 0.0 %. Slight gradients were found in the porosity and microhardness after debinding and sintering in H_2 . These were attributed to the initial porosity gradients in the green parts and potential debinding gradients from the core to the surface of the part. More details are provided in Paper III.

The shrinkage anisotropy of standard green samples was compared for sintering in Ar and H_2 , as the processing atmosphere significantly altered the sintering densification. Figure 20 plots the evolution of the anisotropic factors K_1 , K_2 and K_3 , which are the shrinkage ratios of two directions.

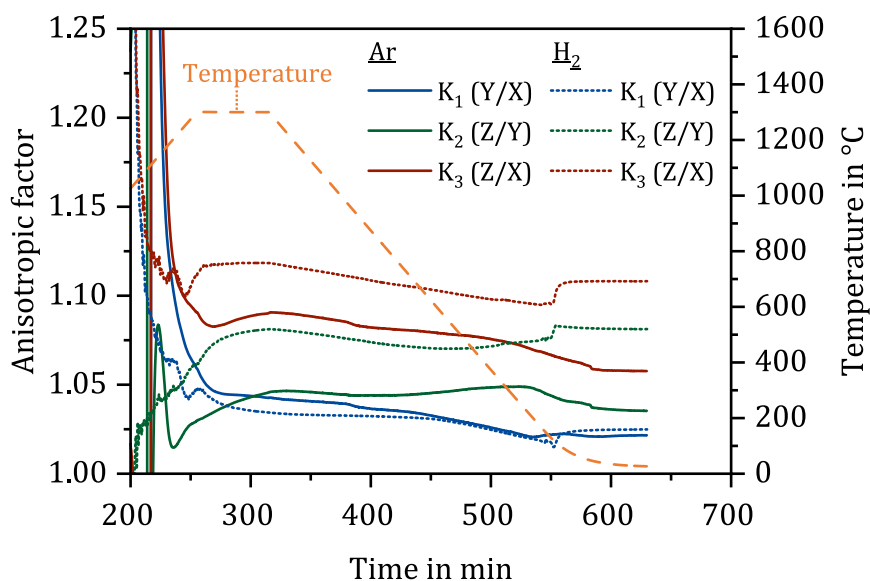


Figure 20: Anisotropic factors for sintering of standard green samples processed under Ar or H_2 atmosphere (Results from Paper IV).

For processing in H₂, the highest shrinkage was measured in the build direction (ϵ_z), indicated by high final anisotropic values for K_2 (~ 1.08) and K_3 (~ 1.11). The highest shrinkage in the build direction is commonly observed for BJT components, which is connected to the porosity distribution in the green parts. The layer-wise printing process typically leads to areas of elevated porosity between two deposited layers, which result in higher shrinkages along the build direction during sintering [124,200].

The final anisotropic factor K_1 was equal for sintering in Ar and H₂ at ~ 1.02 , which corresponded to slightly higher shrinkage in the compaction roller axis direction (ϵ_y) than in the powder spreading direction (ϵ_x). Sintering in Ar led to lower final K_2 (~ 1.04) and K_3 (~ 1.06) values compared to sintering in H₂, which indicated an altered shrinkage anisotropy. This was connected to the lower densification overall for processing in Ar compared to H₂. While the initial porosity gradients in the green part determine the potential shrinkage anisotropy, the processing atmosphere can significantly alter the sintering densification and, thereby, actual shrinkage anisotropy.

5.3 Impact of oxygen content in the debinding atmosphere on binder removal, powder oxidation and sintering densification

The binder consists of various elements, which can be introduced into the material if the debinding process is inadequate. Figure 21 demonstrates how the binder changed the green part chemistry compared to the virgin powder before and after the curing process. The dried state of the green part refers to leaving the build box to dry for 24 h under ambient conditions.

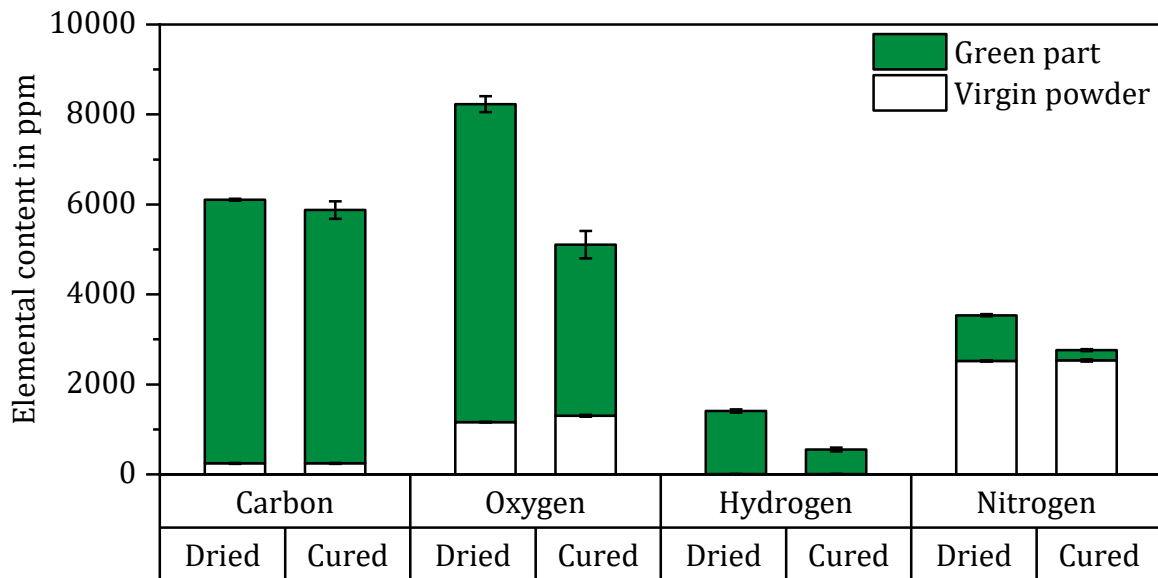


Figure 21: Chemistry of the 17-4 PH powder and corresponding green part before and after the curing process at 200°C for 4 h (Results from Paper V). Figure adapted from [201].

The binder in the green part increased the carbon, oxygen and hydrogen levels significantly compared to those of the original 17-4 PH powder, while the nitrogen content was slightly higher than for the N₂-atomized powder. After the curing process, the binder accounted for ~ 1 wt.% of the total green part mass. The effectiveness of the

debinding process was analyzed by the mass loss and elemental contents of the brown parts. The influence of the O₂ content in the debinding atmosphere was evaluated for debinding at 300°C for 2 h, corresponding to a state-of-the-art prior debinding step.

Figure 22 illustrates the weight loss, carbon content and visual appearance of the brown parts following the prior debinding at 300°C for 2 h under various O₂ concentrations in the atmosphere. Debinding gas mixes with 3 vol.% O₂ up to 20 vol.% O₂ resulted in nearly complete binder removal. However, the brown part stability was notably reduced due to the significant binder removal, which caused minor powder losses during brown part handling, as shown in Figure 22. The low brown part stability can cause problems if the brown parts need to be transferred into a sintering furnace. In addition, unsupported part features might break before sintering neck formation.

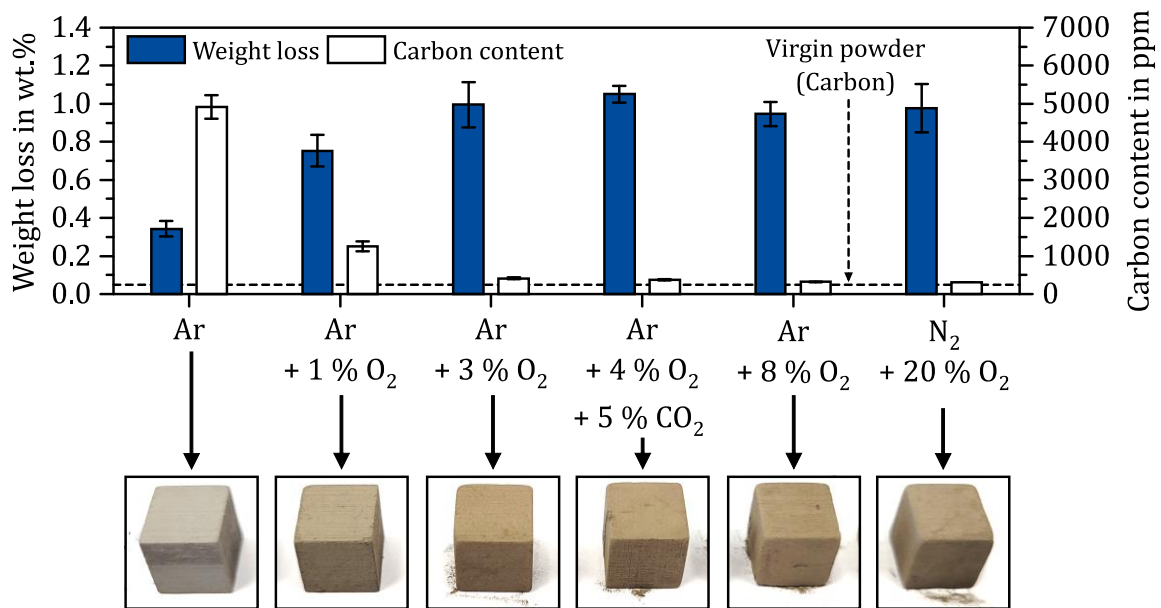


Figure 22: Weight loss, carbon content and visual appearance of brown parts after prior debinding at 300°C for 2 h depending on the debinding atmosphere (Results from Paper V). Figure adapted from [201].

Debinding in inert Ar resulted in low binder removal, leading to a high carbon content of 4923 ± 308 ppm in the brown part. Debinding in Ar + 1 vol.% O₂ exhibited no notable powder losses during handling, although the mass loss was higher than for Ar debinding, resulting in a carbon content of 1256 ± 13 ppm in the brown part.

The prior debinded samples (brown parts) were sintered in inert Ar to assess the effect of the O₂ content in the debinding atmosphere on the sintered chemistry and sintering densification. Figure 23 displays the sintered oxygen and carbon contents for the various debinding atmospheres.

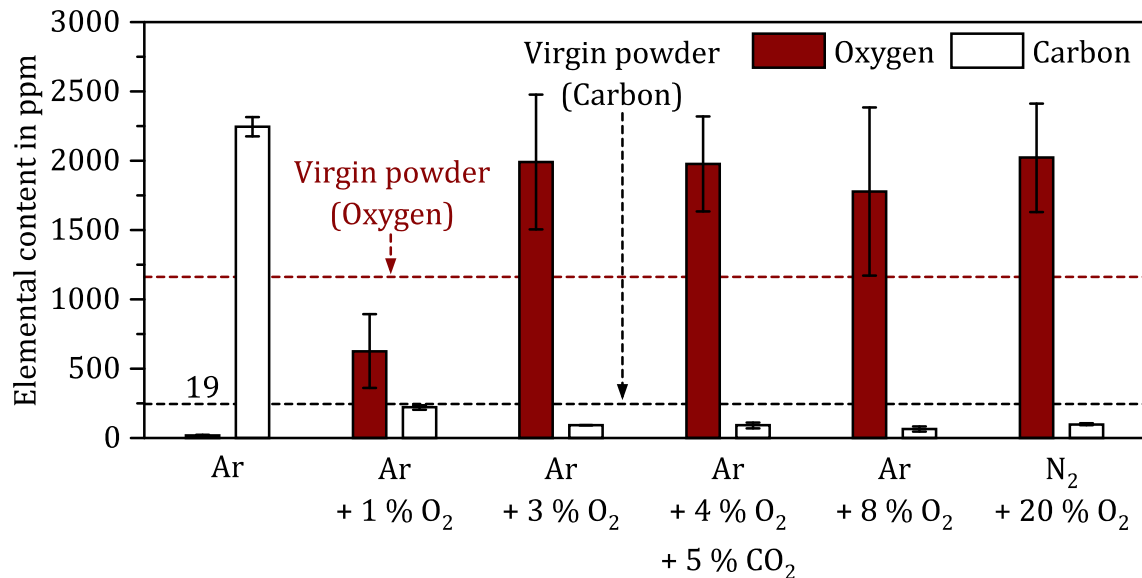


Figure 23: Sintered carbon and oxygen contents for prior debinding at 300°C for 2 h under different atmosphere compositions followed by sintering in inert Ar (Results from Paper VI). Figure adapted from [202].

Prior debinding in Ar and subsequent sintering in Ar resulted in a high amount of carbon above 2000 ppm in the sintered material, caused by the low debinding efficiency in an inert debinding atmosphere. The sintered carbon content was significantly higher than the maximum carbon content of 700 ppm specified for 17-4 PH stainless steel by MPIF35/ASTM B883 – 24 standards for MIM [97,98]. However, the initial oxygen content present in the virgin powder was almost entirely removed by carbothermal reduction due to the high carbon content stemming from the binder.

For prior debinding in 3 vol.% O₂ up to 20 vol.% O₂, the sintered oxygen content was 53 % to 74 % higher than for the virgin powder, which was connected to the powder oxidation in the brown parts during debinding. The oxidation caused during prior debinding could not be sufficiently reversed by sintering in inert Ar because an insufficient amount of carbon was available for carbothermal reduction. The sintered carbon contents dropped even slightly below the virgin powder content, implying that carbon from the powder was consumed for carbothermal reduction. In the case of prior debinding in Ar + 1 vol.% O₂, the sintered oxygen content was 46 % lower than in the virgin powder, while the carbon content was comparable to the virgin powder.

The influence of the prior debinding atmosphere on the as-sintered microstructure of 17-4 PH stainless steel is displayed in Figure 24. The microstructure was comparable for all oxidizing atmospheres, which consisted of a martensitic matrix, island-type δ -ferrite and residual pores. A high sintered density of $\sim 98\%$ was achieved for debinding in Ar + 1 vol.% O_2 and Ar + 3 vol.% O_2 , while the densities varied between $\sim 96\%$ and $\sim 98\%$ for debinding under 4 vol.% O_2 to 20 vol.% O_2 .

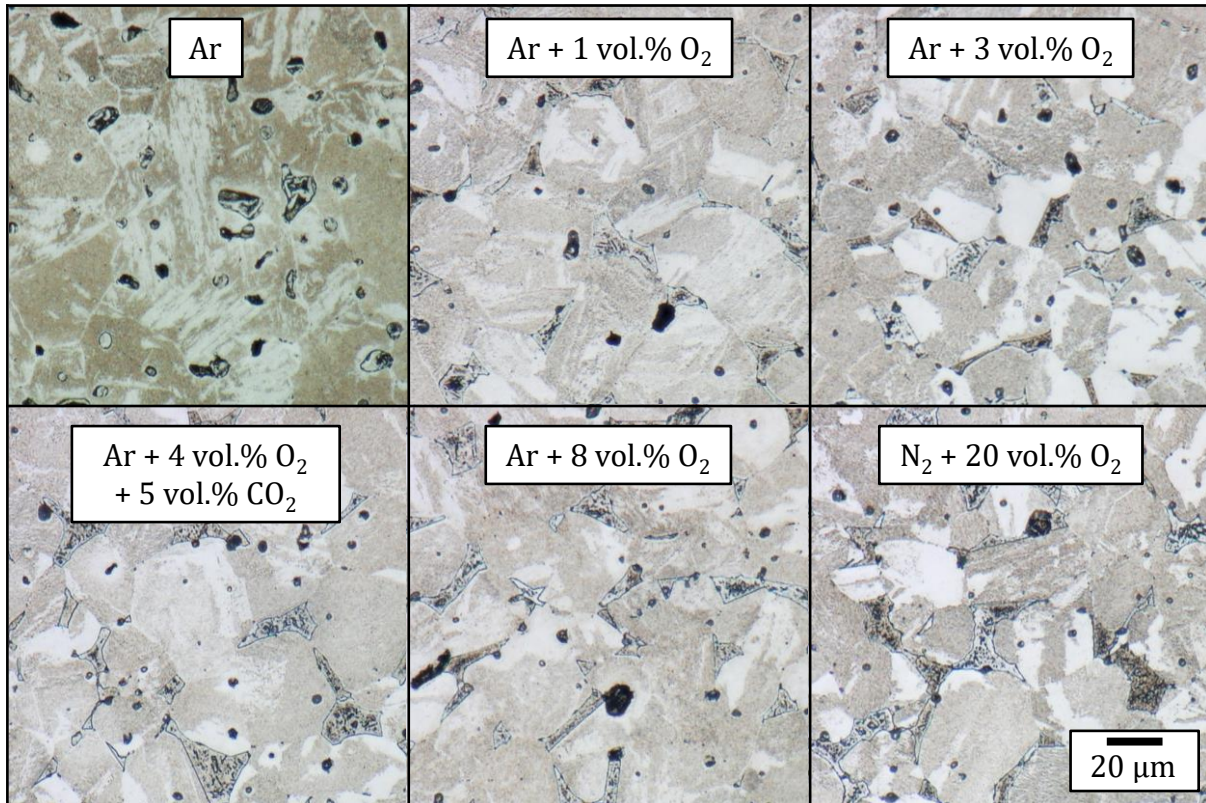


Figure 24: As-sintered microstructure of 17-4 PH stainless steel parts debinded in atmospheres with varying O_2 contents and sintered at $1300^\circ C$ in Ar (Results from Paper VI). Figure adapted from [202].

In contrast, no δ -ferrite was observed in the as-sintered microstructure for prior debinding in Ar, which was caused by the high carbon pickup in the material. Thermodynamic simulations estimated that a carbon level below 1600 ppm is required to form δ -ferrite at $1300^\circ C$, which was not the case for prior debinding and sintering in Ar. Hence, a low sintered density of $\sim 88\%$ was obtained.

The TG experiments were conducted on 17-4 PH virgin powder (see Paper VII) by heating to $700^\circ C$ to assess the effect of the debinding atmosphere on the powder over a broader temperature range. Inert Ar did not cause any powder oxidation, while H_2 caused a decrease of the powder oxygen content by ~ 200 ppm. This decrease in the oxygen content was connected to the reduction of iron oxides by H_2 [168,170], which was registered during TG between $\sim 210^\circ C$ and $\sim 435^\circ C$.

For oxidizing atmospheres, the virgin powder showed a two-stage oxidation behavior. The mass gain progressed comparably between 1 vol.% O_2 and 20 vol.% O_2 in the first stage, with a local maximum mass gain rate registered at $\sim 390^\circ C$. A significant surge in

the oxidation rate was measured starting from $\sim 510^{\circ}\text{C}$, which was enhanced by an increasing O_2 concentration in the atmosphere. Therefore, debinding in oxidizing atmospheres should be conducted far below 510°C for 17-4 PH stainless steel to avoid severe powder oxidation.

Green parts were heated to 700°C to identify the effect of the debinding atmosphere on temperatures of maximum binder removal and notable brown part oxidation. In addition, the effectiveness of the prior debinding step at 300°C for 2 h was compared for Ar, H_2 , Ar + 1 vol.% O_2 and N_2 + 20 vol.% O_2 . Figure 25a presents the TG curves of the green parts under these four atmospheres during heating to 700°C .

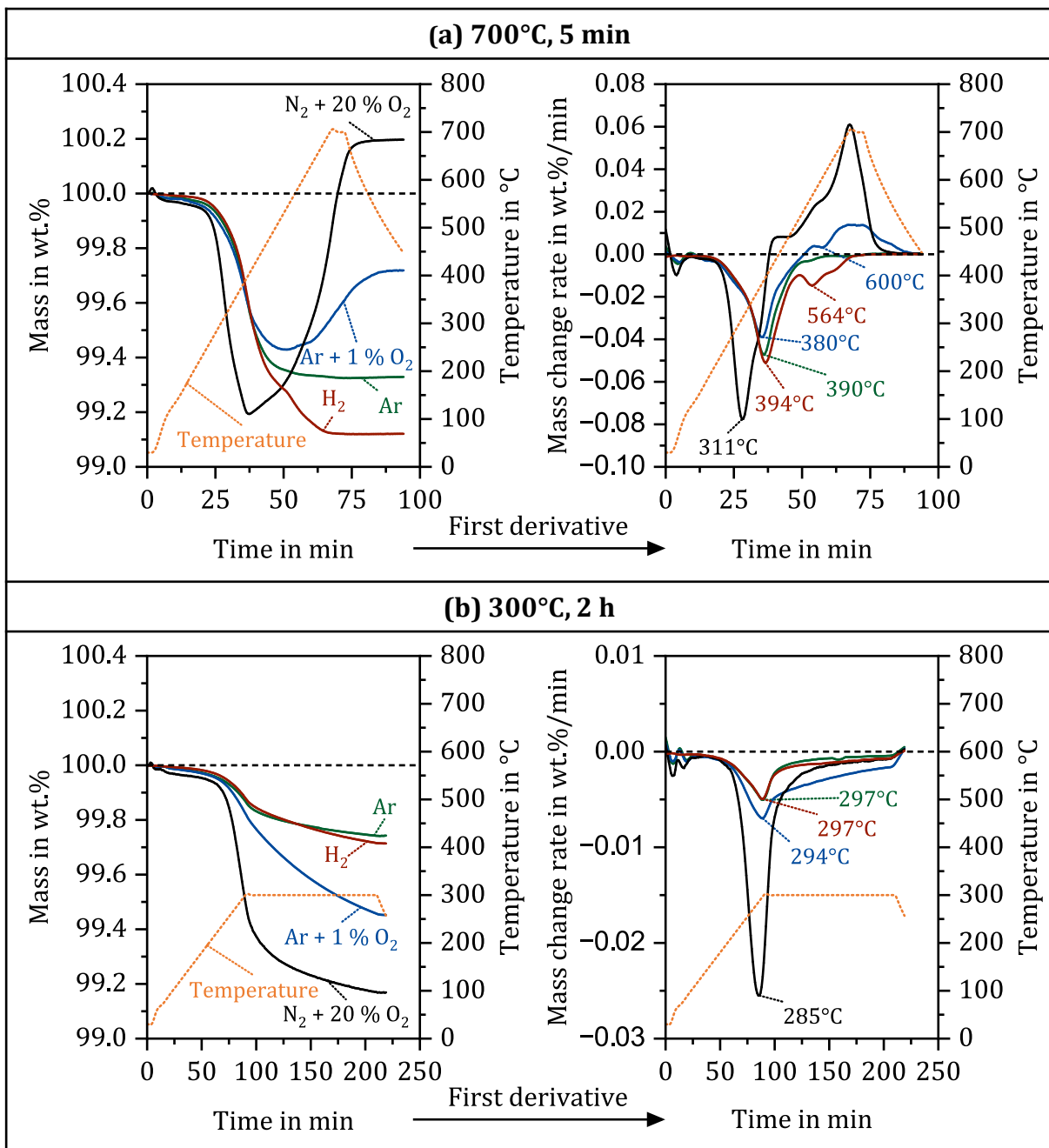


Figure 25: Thermogravimetric curves for debinding in Ar, H_2 , Ar + 1 vol.% O_2 and N_2 + 20 vol.% O_2 at (a) 700°C for 5 min and at (b) 300°C for 2 h (Results from Paper VII).

Debinding in inert Ar resulted in a mass loss of 0.67 wt.% at 700°C. Debinding in H₂ was comparable to debinding in inert Ar up to ~380°C. However, a notable second-stage binder removal was registered at 564°C for H₂ debinding, increasing the total mass loss to 0.88 wt.% at 700°C compared to Ar. Therefore, H₂ seemed to react with the remaining binder components at higher temperatures, aiding the binder decomposition.

The TG trials at 300°C for 2 h in Figure 25b confirmed that debinding in inert Ar and reducing H₂ is inefficient at low temperatures despite a holding step. After the 2 h dwell at 300°C, the mass loss was only 0.26 wt.% for Ar and 0.28 wt.% for H₂, indicating high binder residue in the brown part. Although H₂ enhances binder removal at higher temperatures, it could lead to issues for metals that sinter at low temperatures before the binder is completely removed.

The TG curves for debinding up to 700°C in Figure 25a under oxidizing atmospheres showed an initial mass loss due to binder removal, which was followed by mass gain due to powder oxidation. The maximum mass loss of 0.57 wt.% for Ar + 1 vol.% O₂ was measured at 540°C. For debinding in N₂ + 20 vol.% O₂, the maximum mass loss of 0.81 wt.% was registered at 403°C. The maximum mass loss rate shifted from 380°C for Ar + 1 vol.% O₂ to 311°C for N₂ + 20 vol.% O₂. The shift of the binder removal to lower temperatures was linked to the oxidative binder decomposition, which lowers the required thermal activation [203,204].

After reaching the maximum mass loss due to binder removal, the sample gained 0.15 wt.% of mass during heating to 700°C under Ar + 1 vol.% O₂ due to powder oxidation. The corresponding mass gain due to powder oxidation for debinding in N₂ + 20 vol.% O₂ was significantly higher with 0.82 wt.%. Accordingly, the brown part oxygen content increased from 5340 ppm for Ar + 1 vol.% O₂ to 12900 ppm for N₂ + 20 vol.% O₂.

Debinding in Ar + 1 vol.% O₂ resulted even in a lower brown part oxygen content than the corresponding powder heat treated under the same conditions, indicating that the binder residues on the powder surface decreased powder oxidation during debinding. Notable brown part oxidation occurred above ~510°C for the oxidizing atmospheres, comparable to the isolated virgin powder.

Debinding at 300°C for 2 h in Ar + 1 vol.% O₂ and N₂ + 20 vol.% O₂ resulted in mass losses comparable to the maximum mass losses measured during heating to 700°C. During the dwell of 2 h at 300°C, the mass loss rate approached zero, indicating that the O₂ concentration in the atmosphere limits the maximum binder removal at 300°C. The debinding in oxidizing atmospheres can be effective even at low temperatures. Low debinding temperatures can minimize the risk of powder oxidation and allow for the use of low-cost furnace equipment for prior debinding.

The TG trials for the sintering of brown samples (debinded at 300°C for 2 h) led to a mass loss between ~900°C and ~1300°C, which verified the removal of metal oxides by carbothermal reduction. As the binder residue and powder oxidation varied for different

atmosphere combinations, the mass loss associated with carbothermal reduction was more or less pronounced, which can be seen in Paper VII.

The highest mass loss connected to carbothermal reduction was measured for prior debinding in Ar + 1 vol.% O₂ and subsequent sintering in inert Ar. This was caused by the binder residue in the brown sample, which was not efficiently removed during heating to the sintering temperature under inert Ar. The resulting sintered oxygen content after TG was 191 ppm, significantly lower than in the virgin powder with 1174 ppm.

These findings demonstrate that prior debinding in Ar + 1 vol.% O₂ and subsequent sintering in inert Ar can pose a viable alternative to H₂ debinding and sintering, resulting in high sintering densification and comparable sintered chemistry. Compared to prior debinding in air, powder oxidation can be minimized by reducing the O₂ concentration in the debinding atmosphere.

6 Conclusions

This thesis studied the impact of the processing atmosphere on BJT of 17-4 PH stainless steel, highlighting the role of powder reuse, curing atmospheres, binder residue and debinding atmospheres. The conclusions are presented based on the three research questions of this thesis.

What is the influence of the curing atmosphere and powder reuse on powder characteristics, green parts and sintering densification?

- Curing in ambient air led to oxidation of the 17-4 PH stainless steel powder, which increased powder flowability and packing but reduced the dynamic density during flowability tests. The highest oxygen pickup was measured after the first curing cycle, which was in accordance with an increasing thickness of the powder surface oxide layer. In contrast, curing in inert Ar did not cause powder oxidation and led to rheological properties comparable to the virgin powder.
- Powder reuse over 20 build jobs increased the powder oxygen content by 20 % due to four curing cycles in ambient air. The flowability and packing increased despite a slight humidity pickup of the powder, while the dynamic density decreased after 20 build jobs. The PSD remained comparable after 20 build jobs.
- The curing in ambient air led to a significant drop in the green density by 0.11 g/cm^3 when the depowdered powder was reused for printing. This reduction was assumed to be connected to a change in powder interaction during powder spreading and compaction, which was confirmed by the powder packing obtained from empty build jobs. Powder reuse resulted in a green density reduction from $4.71 \pm 0.03 \text{ g/cm}^3$ to $4.47 \pm 0.07 \text{ g/cm}^3$ over 20 build jobs with decreasing part consistency and, therefore, decreasing process stability.
- The lower green part densities of the reused samples were compensated by higher sintering shrinkages for processing under H_2 , resulting in only slightly lower sintered densities. This was accompanied by a change in the shrinkage anisotropy, indicating a different porosity gradient in the reused green parts.
- While the impact of curing and powder reuse on part quality was minor for sintering in H_2 , the sintered dimensions were significantly changed, decreasing the process robustness. Consequently, the curing process should be conducted in an inert environment such as Ar or N_2 to avoid changes in powder characteristics that can significantly change the outcome of the green part.

How do binder content and its distribution impact powder packing, sintering densification, microstructure gradients and shrinkage anisotropy?

- Samples with 25 %, 50 %, 75 % and 100 % shell volume were printed. The green density increased considerably with increasing shell volume, which was connected to a higher powder packing in the shell. This was attributed to binder-induced particle rearrangement during printing, resulting in a higher powder packing in the binder-affected shell than in the binder-free core.
- Sintering under Ar highlighted the detrimental impact of increasing binder content in the green part since the debinding efficiency was low for inert Ar. The sintering

densification decreased significantly from 25 % to 100 % shell volume, primarily due to the increased carbon pickup in the steel during debinding, inhibiting the formation of δ -ferrite, which enhanced the sintering densification of 17-4 PH considerably. Therefore, the sintered densities decreased from 99.3 ± 0.2 % to 93.4 ± 1.8 % from 25 % to 100 % shell volume. However, the sintered oxygen content decreased from 745 ppm for 25 % shell volume to 63 ppm for 100 % shell volume due to a more pronounced carbothermal reduction connected to the increasing carbon residue.

- Sintering under H_2 demonstrated the impact of the powder packing on sintering densification. Processing in H_2 efficiently removed the binder and metal oxides for all shell volumes, resulting in high fractions of δ -ferrite. The lower powder packing with decreasing shell volume was compensated by higher shrinkages, leading to comparable sintered densities between 99.7 ± 0.1 % and 99.9 ± 0.0 %.
- Significant microstructure gradients were identified for processing in Ar, which were connected to the inhomogeneous binder distribution. For 50 %, 75 % and 100 % shell volume, the carbon introduced by the binder reduced the δ -ferrite formation in the shell, leading to higher porosity in the shell than in the binder-free core. The higher carbon content in the shell stabilized austenite during cooling, resulting in high fractions of retained austenite and low microhardness after cooling. Sintering in H_2 resulted in slight microstructure gradients, likely due to a slight gradient in the powder packing and debinding from the core to the surface of the part.
- The processing atmosphere significantly affected the sintering densification and, therefore, the sintering anisotropy, indicated by varying anisotropic factors. The highest shrinkage was measured in the build direction for Ar and H_2 sintering due to elevated inter-layer porosity created in the build direction during printing. The part design must account for the differences in the shrinkage and anisotropy depending on the set processing atmosphere.

What is the impact of oxygen content in the debinding atmosphere on binder removal, powder oxidation and subsequent sintering densification?

- Oxidizing atmospheres exhibited efficient binder removal at lower temperatures in contrast to inert Ar and reducing H_2 , as rising O_2 concentrations in the debinding atmosphere decreased the debinding temperatures due to the lower thermal activation for oxidative binder degradation. The maximum mass loss was 0.57 wt.% for debinding in Ar + 1 vol.% O_2 , whereas 0.81 wt.% for debinding in N_2 + 20 vol.% O_2 during heating to 700°C.
- Prior debinding at 300°C for 2 h showed nearly complete binder removal for 3 vol.% O_2 up to 20 vol.% O_2 in the debinding atmosphere composition. However, this led to minor powder losses during part handling due to low brown part stability. TG trials demonstrated that binder removal under Ar + 1 vol.% O_2 and N_2 + 20 vol.% O_2 was equally effective for prior debinding at 300°C for 2 h as for heating to 700°C.
- TG experiments showed that severe powder and brown part oxidation occurred above $\sim 510^\circ\text{C}$, which was considerably enhanced with increasing O_2 content from

1 vol.% O₂ to 20 vol.% O₂ in the atmosphere. At temperatures below 510°C, the oxidation of the virgin powder progressed comparably for all O₂ concentrations. Consequently, debinding in oxidizing atmospheres should be conducted between 300°C and 500°C to maximize binder removal and minimize powder oxidation. The brown part oxidation was lower than the virgin powder oxidation for processing in Ar + 1 vol.% O₂, which suggested that the binder on powder surfaces decreased the powder oxidation slightly.

- Sintering densification was high for sintering in inert Ar if the prior debinding step at 300°C for 2 h removed the binder sufficiently, allowing for the formation of δ -ferrite during sintering, which was the case for all oxidizing atmospheres from 1 vol.% O₂ to 20 vol.% O₂. This resulted in comparable sintered densities between 96 % and 98 %. However, prior debinding and sintering in Ar resulted in a high sintered carbon content above 2000 ppm, which led to low sintering densification due to the absence of δ -ferrite. Nevertheless, the high carbon residue stemming from the binder aided oxide removal by carbothermal reduction, leading to nearly complete oxide removal.
- Samples prior debinded in 3 vol.% O₂ up to 20 vol.% O₂ led to sintered oxygen contents, which were 53 % to 74 % higher than in the virgin powder after sintering in inert Ar. Debinding in Ar + 1 vol.% O₂ resulted in the best combination of binder removal, brown part stability, sintering densification and reduction of the sintered oxygen content by 46 % compared to the virgin powder after sintering in Ar.

7 Future Work

Based on the insights of this thesis, several research areas are recommended for future exploration.

Influence of the curing atmosphere and powder reuse

- Printing in a controlled atmosphere resulted in consistent printing results. The humidity in the printing environment can potentially alter the printing behavior of the powder and binder. The influence of varying ambient conditions, such as different relative humidity levels, on the printing results should be systematically studied.
- The detrimental impact of curing in ambient air on process robustness was highlighted for 17-4 PH stainless steel. The effect of the curing atmosphere on powder characteristics, powder reuse and printing results should be investigated for more materials, especially metal powders prone to oxidation, such as copper.
- During BJT printing, complex interactions arise between the powder, binder and printer hardware, which are affected by the powder and binder properties. The simulation and modeling of such phenomena can provide valuable insights into how different material properties and printing parameters influence powder packing during printing.
- It was shown that sintering in H₂ atmosphere resulted in slightly lower sintered densities due to the lower initial green densities of reused samples. The influence of powder reuse on the mechanical properties should be investigated.

Impact of the binder content and its distribution

- A higher powder packing was indicated in the binder-affected shell than in the binder-free core of the green parts. To analyze the difference in density between the core and the shell, high-resolution synchrotron X-ray computed tomography (SXCT) can be utilized.
- The choice of powder, binder and printer hardware influences the potential for particle rearrangement during printing. The powder-binder interaction during printing and the influence on powder packing should be studied in detail.
- The binder had a detrimental impact on the sintering densification of 17-4 PH stainless steel due to carbon pickup in the case of insufficient debinding. The effect of binder residue on other materials, such as copper, titanium or nickel-based alloys, should be studied.
- Despite efficient debinding under H₂, slight gradients in microstructure and porosity were found in the sintered samples. It is expected that larger wall thicknesses might lead to even stronger microstructure gradients due to the increasing difficulty of binder removal from the core of the part. The influence of increasing wall thicknesses on microstructure gradients needs to be explored.

- The impact of the microstructure gradients due to shell printing on mechanical properties and corrosion resistance of 17-4 PH stainless steel should be studied. The interfaces between the shell and core could be potential crack initiation sites.

Impact of the oxygen content in the debinding atmosphere

- Varying the O₂ concentration in the atmosphere influenced the debinding temperatures and effectiveness. However, it remains unclear whether the O₂ concentration affects the decomposition products forming during debinding. Process monitoring by measuring the O₂, CO₂ and CO concentrations in the debinding zone and at the outlet of the debinding furnace can provide insights into the binder decomposition. The binder decomposition products can be analyzed in detail by mass spectroscopy or FTIR, which can identify species like CO₂, CO, H₂O, NH₃ and hydrocarbons.
- The heating profile for debinding can be optimized for each O₂ concentration in the debinding gas mix individually. TG, FTIR and other sensors can be utilized to improve the debinding process parameters to balance binder removal, powder oxidation and processing times.
- The concept of tailoring the O₂ content in the debinding atmosphere should, in principle, be transferable to other binder formulations and metal powders, as binder decomposition and powder oxidation are expected to be affected similarly. The transferability also applies to other binder-assisted powder manufacturing technologies that require thermal debinding, including various SBAM and traditional PM technologies.
- The sintered oxygen content varied for the different O₂ concentrations in the debinding atmospheres. The influence of the sintered oxygen content on mechanical properties of 17-4 PH should be investigated since the inclusions of metal oxides in the sintering necks can be detrimental to the mechanical properties. Corrosion properties might also be affected.
- The gas flow and sample positioning in the furnace were kept constant. However, an influence of the gas flow, part sizes, part positioning, furnace load and design on the debinding effectiveness is expected. The gas flow and composition requirements might vary based on part size and furnace load. A systematic analysis of the influence of gas flow rates and part sizes on debinding efficiency should be conducted.
- Sintering in a vacuum and a slightly reducing atmosphere (Ar-H₂ gas mix) are viable alternatives to sintering in Ar or H₂. The combination with a tailored debinding atmosphere could result in part quality comparable to or better than H₂ debinding and sintering.

Acknowledgments

First, I want to express my gratitude to Prof. Eduard Hryha and Pierre Forêt, who granted me the opportunity to pursue a PhD degree in an industrial environment under a unique cooperation. This setting provided me with valuable insights into both academia and industry, facilitating my personal development as a researcher and engineer. Setting up a new laboratory and process chain for Binder Jetting was an enriching experience.

I am thankful for the funding provided by Linde GmbH, the Federal Ministry of Research and Education (BMBF, Germany), the Centre for Additive Manufacturing – Metal (CAM²) and the Swedish Governmental Agency of Innovation Systems (Vinnova).

My utmost gratitude goes to my supervisor, Prof. Eduard Hryha, for his continuous support, excellent academic guidance and constant encouragement during my journey. I also want to thank Pierre Forêt sincerely for his industrial guidance and outstanding support in the realization of the research and projects. I would also like to express my gratitude to my examiner, Prof. Lars Nyborg.

The success of this thesis is closely tied to the valuable support from many people along the journey. Without their support, this milestone would not have been possible to achieve. I am especially thankful for my co-supervisors, Dr. Elena Bernardo and Dr. Sophie Dubiez-Le Goff, whose expertise, experience and continuous support I highly value.

I want to place a special thank you to my current and former office colleagues, Tobias Deckers, Julian Henrichs and Siegfried Bähr, who shared the journey of pursuing a doctoral degree with me. Their support in daily challenges, scientific questions and valuable feedback contributed significantly to the success of this work.

I would like to recognize and thank my colleagues Anok, Sofia and Gowtham from Chalmers for their great contribution to the work. I would also like to acknowledge Rasmus, Alberto, Bharat, Bala, Fardan, William and Laura from Chalmers, who shared my path of pursuing a PhD degree.

I am also thankful for the support of my three master's thesis students, Sankhya, Jim and Fawas, whom I had the pleasure of supervising. I also appreciate our interns Victor, Ning, Umair and Harhi, who helped with experimental work. Furthermore, I also want to thank current and former colleagues at Linde who helped me set up the laboratory, provided technical support or advised in safety aspects: Dominik, Tanja, Thomas, Matthias, Tobias and Ron.

My deepest gratitude goes to my family and friends, who indirectly contributed to the success of my PhD journey by providing continuous encouragement and loving support during these busy and stressful times.

References

- [1] A. Mostafaei *et al.*, “Binder jet 3D printing—Process parameters, materials, properties, modeling, and challenges,” *Progress in Materials Science*, vol. 119, p. 100707, Jun. 2021, <https://doi.org/10.1016/j.pmatsci.2020.100707>.
- [2] T. Pereira, J. V. Kennedy, and J. Potgieter, “A comparison of traditional manufacturing vs additive manufacturing, the best method for the job,” *Digital Manufacturing Transforming Industry Towards Sustainable Growth*, vol. 30, pp. 11–18, Jan. 2019, <https://doi.org/10.1016/j.promfg.2019.02.003>.
- [3] W. Gao *et al.*, “The status, challenges, and future of additive manufacturing in engineering,” *Computer-Aided Design*, vol. 69, pp. 65–89, Dec. 2015, <https://doi.org/10.1016/j.cad.2015.04.001>.
- [4] S. A. M. Tofail, E. P. Koumoulos, A. Bandyopadhyay, S. Bose, L. O’Donoghue, and C. Charitidis, “Additive manufacturing: scientific and technological challenges, market uptake and opportunities,” *Materials Today*, vol. 21, no. 1, pp. 22–37, Jan. 2018, <https://doi.org/10.1016/j.mattod.2017.07.001>.
- [5] A. Lores, N. Azurmendi, I. Agote, and E. Zuza, “A review on recent developments in binder jetting metal additive manufacturing: materials and process characteristics,” *Powder Metallurgy*, vol. 62, no. 5, pp. 267–296, Oct. 2019, <https://doi.org/10.1080/00325899.2019.1669299>.
- [6] A. H. Alami *et al.*, “Additive manufacturing in the aerospace and automotive industries: Recent trends and role in achieving sustainable development goals,” *Ain Shams Engineering Journal*, vol. 14, no. 11, p. 102516, Nov. 2023, <https://doi.org/10.1016/j.asej.2023.102516>.
- [7] M. H. Mobarak *et al.*, “Recent advances of additive manufacturing in implant fabrication – A review,” *Applied Surface Science Advances*, vol. 18, p. 100462, Dec. 2023, <https://doi.org/10.1016/j.apsadv.2023.100462>.
- [8] N. Zhao *et al.*, “Direct additive manufacturing of metal parts for automotive applications,” *Journal of Manufacturing Systems*, vol. 68, pp. 368–375, Jun. 2023, <https://doi.org/10.1016/j.jmsy.2023.04.008>.
- [9] I. Fidan *et al.*, “Recent Inventions in Additive Manufacturing: Holistic Review,” *Inventions*, vol. 8, no. 4, p. 103, Aug. 2023, <https://doi.org/10.3390/inventions8040103>.
- [10] M. Armstrong, H. Mehrabi, and N. Naveed, “An overview of modern metal additive manufacturing technology,” *Journal of Manufacturing Processes*, vol. 84, pp. 1001–1029, Dec. 2022, <https://doi.org/10.1016/j.jmapro.2022.10.060>.
- [11] T. Studnitzky, C. Zhong, T. Weissgaerber, and C. Aumund-Kopp, “Review Of Sinter-Based Additive Manufacturing (SBAM) - Status And Prospects,” in *Euro PM2023 Proceedings*, Lisbon, Portugal, Sep. 2023, <https://doi.org/10.59499/EP235765077>.
- [12] “ISO/ASTM 52900:2021 Additive manufacturing – General principles – Fundamentals and vocabulary.” International Organization for Standardization/ASTM International, Nov. 16, 2021.

- [13] T. Do, P. Kwon, and C. S. Shin, "Process development toward full-density stainless steel parts with binder jetting printing," *International Journal of Machine Tools and Manufacture*, vol. 121, pp. 50–60, Oct. 2017, <https://doi.org/10.1016/j.ijmachtools.2017.04.006>.
- [14] M. Ziaee and N. B. Crane, "Binder jetting: A review of process, materials, and methods," *Additive Manufacturing*, vol. 28, pp. 781–801, Aug. 2019, <https://doi.org/10.1016/j.addma.2019.05.031>.
- [15] K. Janzen, T. Rieß, and C. Emmelmann, "Investigation on curing strategies for metal binder jetting with Ti-6Al-4V," *Additive Manufacturing Letters*, vol. 13, p. 100272, Apr. 2025, <https://doi.org/10.1016/j.addlet.2025.100272>.
- [16] M. Li, W. Du, A. Elwany, Z. Pei, and C. Ma, "Metal Binder Jetting Additive Manufacturing: A Literature Review," *Journal of Manufacturing Science and Engineering*, vol. 142, no. 9, p. 090801, Sep. 2020, <https://doi.org/10.1115/1.4047430>.
- [17] R. M. German, "MIM 17-4 PH Stainless Steel: Processing, properties and best practice," *Powder Injection Moulding International*, vol. 12, no. 2, pp. 49–76, 2018.
- [18] R. M. German and A. Bose, Eds., "Case Studies of Powder-Binder Processing Practices," in *Binder and Polymer Assisted Powder Processing*, ASM International, pp. 201–249, April 2020, <https://doi.org/10.31399/asm.tb.bpapp.t59290201>.
- [19] R. M. German and A. Bose, Eds., "Binder Removal," in *Binder and Polymer Assisted Powder Processing*, ASM International, pp. 139–167, 2020, <https://doi.org/10.31399/asm.tb.bpapp.t59290139>.
- [20] P. F. Stratton and M. S. Stanescu, "An Introduction to Atmosphere Furnace Safety," in *Proceedings of the 22nd Heat Treating Society Conference and the 2nd International Surface Engineering Congress*, Indianapolis, USA, Sep. 2003, pp. 15–23.
- [21] R. M. German and A. Bose, Eds., "Opportunities for Powder-Binder Forming Technologies," in *Binder and Polymer Assisted Powder Processing*, ASM International, pp. 251–260, April 2020, <https://doi.org/10.31399/asm.tb.bpapp.t59290251>.
- [22] K. Yu *et al.*, "Oxygen content control in metal injection molding of 316L austenitic stainless steel using water atomized powder," *Journal of Manufacturing Processes*, vol. 50, pp. 498–509, Feb. 2020, <https://doi.org/10.1016/j.jmapro.2019.12.038>.
- [23] P. Forcellese, T. Mancina, M. Simoncini, and T. Bellezze, "Investigation on Corrosion Resistance Properties of 17-4 PH Bound Metal Deposition As-Sintered Specimens with Different Build-Up Orientations," *Metals*, vol. 12, no. 4, p. 588, Apr. 2022, <https://doi.org/10.3390/met12040588>.
- [24] U. Hofmann, J. Ferchow, and M. Meboldt, "Evaluating effect of manufacturing process on design in metal binder jetting," *Results in Engineering*, vol. 24, p. 103430, Dec. 2024, <https://doi.org/10.1016/j.rineng.2024.103430>.
- [25] A. Davids, L. Apfelbacher, L. Hitzler, and C. Kremaszky, "Multi-step Additive Manufacturing Technologies Utilizing the Powder Metallurgical Manufacturing Route," in *Lectures Notes on Advanced Structured Materials*, H. Altenbach, M. Jöhltz,

- M. Merkel, and A. Öchsner, Eds. Cham: Springer International Publishing, pp. 99–117, 2022, https://doi.org/10.1007/978-3-031-11589-9_6.
- [26] S. Mirzababaei and S. Pasebani, “A Review on Binder Jet Additive Manufacturing of 316L Stainless Steel,” *Journal of Manufacturing and Materials Processing*, vol. 3, no. 3, p. 82, Sep. 2019, <https://doi.org/10.3390/jmmp3030082>.
- [27] X. Lv, F. Ye, L. Cheng, and L. Zhang, “A versatile thermally initiated crosslinking binder for additive manufacturing of strong structures,” *Additive Manufacturing*, vol. 56, p. 102893, Aug. 2022, <https://doi.org/10.1016/j.addma.2022.102893>.
- [28] Z. Su *et al.*, “Overcoming the penetration–saturation trade-off in binder jet additive manufacturing via rapid in situ curing,” *Additive Manufacturing*, vol. 59, p. 103157, Nov. 2022, <https://doi.org/10.1016/j.addma.2022.103157>.
- [29] D. Gilmer *et al.*, “An in-situ crosslinking binder for binder jet additive manufacturing,” *Additive Manufacturing*, vol. 35, p. 101341, Oct. 2020, <https://doi.org/10.1016/j.addma.2020.101341>.
- [30] N. Shang, T. Dahmen, T. Christiansen, and V. Nadimpalli, “Impact Of Saturation, Layer Thickness And Part Orientation On Green Strength In Metal Binder Jetting Additive Manufacturing Of Powder Feedstock Obtained From Spray Forming,” in *Euro PM2023 Proceedings*, Lisbon, Portugal, Sep. 2023, <https://doi.org/10.59499/EP235764032>.
- [31] R. K. Enneti and K. C. Prough, “Effect of binder saturation and powder layer thickness on the green strength of the binder jet 3D printing (BJ3DP) WC-12%Co powders,” *International Journal of Refractory Metals and Hard Materials*, vol. 84, p. 104991, Nov. 2019, <https://doi.org/10.1016/j.ijrmhm.2019.104991>.
- [32] J.-W. Oh, S. Nahm, B. Kim, and H. Choi, “Anisotropy in Green Body Bending Strength due to Additive Direction in the Binder-Jetting Additive Manufacturing Process,” *Korean Journal of Metals and Materials*, vol. 57, no. 4, pp. 227–235, Apr. 2019.
- [33] R. K. Enneti, S. J. Park, R. M. German, and S. V. Atre, “Review: Thermal Debinding Process in Particulate Materials Processing,” *Materials and Manufacturing Processes*, vol. 27, no. 2, pp. 103–118, Feb. 2012, <https://doi.org/10.1080/10426914.2011.560233>.
- [34] M. Khademitab *et al.*, “Does selective shell printing advance binder jetting additive manufacturing?,” *Powder Technology*, vol. 441, p. 119812, May 2024, <https://doi.org/10.1016/j.powtec.2024.119812>.
- [35] P. Cao and M. D. Hayat, “Chapter 4 - Impurity management in reactive metals injection molding,” in *Feedstock Technology for Reactive Metal Injection Molding*, P. Cao and M. D. Hayat, Eds. Elsevier, pp. 145–190, January 2020, <https://doi.org/10.1016/B978-0-12-817501-9.00004-1>.
- [36] D. Gilmer, S. Kim, D. J. Goldsby, P. Nandwana, A. Elliott, and T. Saito, “Predictive binder jet additive manufacturing enabled by clean burn-off binder design,” *Additive Manufacturing*, vol. 80, p. 103955, Jan. 2024, <https://doi.org/10.1016/j.addma.2024.103955>.
- [37] Y. Wu, D. Blaine, B. Marx, and C. Schlaefer, “Effects of residual carbon content on sintering shrinkage, microstructure and mechanical properties of injection molded

- 17-4 PH stainless steel," *Journal of Materials Science*, vol. 37, pp. 3573–3583, Sep. 2002, <https://doi.org/10.1023/A:1016532418920>.
- [38] K. M. Rahman, A. Wei, H. Miyajima, and C. B. Williams, "Impact of binder on part densification: Enhancing binder jetting part properties through the fabrication of shelled geometries," *Additive Manufacturing*, vol. 62, p. 103377, Jan. 2023, <https://doi.org/10.1016/j.addma.2022.103377>.
- [39] M. Pourshams, A. Elliott, C. Chinnasamy, B. Poorganji, O. Benafan, and M. Elahinia, "Process development of NiTi using binder jetting additive manufacturing: Investigation of the sintering process," *Journal of Manufacturing Processes*, vol. 127, pp. 671–682, Oct. 2024, <https://doi.org/10.1016/j.jmapro.2024.08.009>.
- [40] M. Renowden and P. Pourtalet, "Experimental studies on lubricant removal," *Metal Powder Report*, vol. 45, no. 9, pp. 625–628, Sep. 1990, [https://doi.org/10.1016/0026-0657\(90\)90593-6](https://doi.org/10.1016/0026-0657(90)90593-6).
- [41] P. Quadbeck, A. Strauß, L. Wimbert, R. Lindenau, and B. Kieback, "Atmosphere Study on the Thermal Decomposition Behavior of Delubrication Aiding Additives," in *Proceedings Euro PM 2017*, Milano, Italy, Oct. 2017.
- [42] Y. Xianfeng *et al.*, "Study of thermal degradation mechanism of binders for ceramic injection molding by TGA-FTIR," *Ceramics International*, vol. 45, no. 8, pp. 10707–10717, Jun. 2019, <https://doi.org/10.1016/j.ceramint.2019.02.142>.
- [43] R. German, "Thinking about metal Binder Jetting or FFF? Here is (almost) everything you need to know about sintering," *Metal AM*, vol. 5, no. 3, pp. 127–139, 2019.
- [44] "Powder metallurgy — Vocabulary (ISO 3252:2023)." International Organization for Standardization, 2023.
- [45] R. M. German, "Coarsening in Sintering: Grain Shape Distribution, Grain Size Distribution, and Grain Growth Kinetics in Solid-Pore Systems," *Critical Reviews in Solid State and Materials Sciences*, vol. 35, no. 4, pp. 263–305, Nov. 2010, <https://doi.org/10.1080/10408436.2010.525197>.
- [46] M. N. Rahaman, "2 - Kinetics and mechanisms of densification," in *Sintering of Advanced Materials*, Z. Z. Fang, Ed. Woodhead Publishing, pp. 33–64, January 2010, <https://doi.org/10.1533/9781845699949.1.33>.
- [47] S.-J. L. Kang, "4 - INITIAL STAGE SINTERING," in *Sintering*, S.-J. L. Kang, Ed. Oxford: Butterworth-Heinemann, pp. 39–55, January 2005, <https://doi.org/10.1016/B978-075066385-4/50004-2>.
- [48] R. M. German, "1 - Thermodynamics of sintering," in *Sintering of Advanced Materials*, Z. Z. Fang, Ed. Woodhead Publishing, pp. 3–32, January 2010, <https://doi.org/10.1533/9781845699949.1.3>.
- [49] R. M. German, "Chapter Six - Geometric Trajectories during Sintering," in *Sintering: from Empirical Observations to Scientific Principles*, R. M. German, Ed. Boston: Butterworth-Heinemann, pp. 141–181, January 2014, <https://doi.org/10.1016/B978-0-12-401682-8.00006-9>.
- [50] H. Salmang, H. Scholze, and R. Telle, Eds., "Sintern," in *Keramik*, Berlin, Heidelberg: Springer, pp. 313–380, 2007, https://doi.org/10.1007/978-3-540-49469-0_4.

- [51] R. J. Brook, "Sintering: An Overview," in *Concise Encyclopedia of Advanced Ceramic Materials*, R. Brook, Ed. Oxford: Pergamon, pp. 438–440, January 1991, <https://doi.org/10.1016/B978-0-08-034720-2.50121-0>.
- [52] R. M. German and A. Bose, Eds., "Sintering Densification," in *Binder and Polymer Assisted Powder Processing*, ASM International, pp. 169–191, April 2020, <https://doi.org/10.31399/asm.tb.bpapp.t59290169>.
- [53] R. M. German, "Chapter Nine - Sintering With a Liquid Phase," in *Sintering: from Empirical Observations to Scientific Principles*, R. M. German, Ed. Boston: Butterworth-Heinemann, pp. 247–303, January 2014, <https://doi.org/10.1016/B978-0-12-401682-8.00009-4>.
- [54] P. Kumar, J. Radhakrishnan, S. S. Gan, A. Bryl, J. McKinnell, and U. Ramamurty, "Tensile and fatigue properties of the binder jet printed and hot isostatically pressed 316L austenitic stainless steel," *Materials Science and Engineering: A*, vol. 868, p. 144766, Mar. 2023, <https://doi.org/10.1016/j.msea.2023.144766>.
- [55] A. Yegyan Kumar, Y. Bai, A. Eklund, and C. B. Williams, "The effects of Hot Isostatic Pressing on parts fabricated by binder jetting additive manufacturing," *Additive Manufacturing*, vol. 24, pp. 115–124, Dec. 2018, <https://doi.org/10.1016/j.addma.2018.09.021>.
- [56] A. Kaletsch, F. Radtke, S. Herzog, P. Köhnen, S. Höges, and C. Broeckmann, "Influence of Hot Isostatic Pressing on Microstructure and Tensile Properties of Nickel-Free Stainless Steel for Metal Binder Jetting," *Applied Sciences*, vol. 13, no. 23, p. 12676, Jan. 2023, <https://doi.org/10.3390/app132312676>.
- [57] A. Lores, N. Azurmendi, I. Agote, E. Espinosa, and M. B. García-Blanco, "A study of parameter and post-processing effects on surface quality improvement of Binder Jet 3D-printed Invar36 alloy parts," *Progress in Additive Manufacturing*, vol. 7, no. 5, pp. 917–930, Oct. 2022, <https://doi.org/10.1007/s40964-022-00267-w>.
- [58] B. Utela, D. Storti, R. Anderson, and M. Ganter, "A review of process development steps for new material systems in three dimensional printing (3DP)," *Journal of Manufacturing Processes*, vol. 10, no. 2, pp. 96–104, Jul. 2008, <https://doi.org/10.1016/j.jmapro.2009.03.002>.
- [59] R. M. German and A. Bose, Eds., "Binder Formulation," in *Binder and Polymer Assisted Powder Processing*, ASM International, pp. 67–83, April 2020, <https://doi.org/10.31399/asm.tb.bpapp.t59290067>.
- [60] J. Saruta, T. Osada, and S. Kobayashi, "Properties of Thermosetting Urethane Acrylate Binder for Metal Binder Jet Additive Manufacturing," *Journal of the Japan Society of Powder and Powder Metallurgy*, vol. 72, no. Supplement, pp. S1073–S1078, 2025, <https://doi.org/10.2497/jjspm.16A-T7-28>.
- [61] S. Im, R. Batmaz, A. Natarajan, and É. Martin, "Compatibility Study of Polymeric Binders for Aluminum Binder Jet Parts," in *Light Metals 2023*, Cham, 2023, pp. 471–477, https://doi.org/10.1007/978-3-031-22532-1_64.
- [62] X. Fang, Y. Zu, Q. Ma, and J. Hu, "State of the art of metal powder bonded binder jetting printing technology," *Discover Materials*, vol. 3, no. 1, p. 15, Jun. 2023, <https://doi.org/10.1007/s43939-023-00050-w>.

- [63] E. L. S. Erickson and M. Chmielus, "Binder Jetting," in *Springer Handbook of Additive Manufacturing*, E. Pei, A. Bernard, D. Gu, C. Klahn, M. Monzón, M. Petersen, and T. Sun, Eds. Cham: Springer International Publishing, pp. 443–458, 2023, https://doi.org/10.1007/978-3-031-20752-5_27.
- [64] J. Marczyk, K. Ostrowska, and M. Hebda, "Influence of binder jet 3D printing process parameters from irregular feedstock powder on final properties of Al parts," *Advanced Powder Technology*, vol. 33, no. 11, p. 103768, Nov. 2022, <https://doi.org/10.1016/j.apt.2022.103768>.
- [65] M. Munsch, M. Schmidt-Lehr, and E. Wycisk, "Binder Jetting and FDM: A comparison with Laser Powder Bed Fusion and Metal Injection Moulding," *Metal AM*, vol. 4, no. 3, pp. 159–167, Autumn/Fall 2018.
- [66] M. Ziaee, E. M. Tridas, and N. B. Crane, "Binder-Jet Printing of Fine Stainless Steel Powder with Varied Final Density," *JOM*, vol. 69, no. 3, pp. 592–596, Mar. 2017, <https://doi.org/10.1007/s11837-016-2177-6>.
- [67] D. Huber, L. Vogel, and A. Fischer, "The effects of sintering temperature and hold time on densification, mechanical properties and microstructural characteristics of binder jet 3D printed 17-4 PH stainless steel," *Additive Manufacturing*, vol. 46, p. 102114, Oct. 2021, <https://doi.org/10.1016/j.addma.2021.102114>.
- [68] P. Nandwana, A. M. Elliott, D. Siddel, A. Merriman, W. H. Peter, and S. S. Babu, "Powder bed binder jet 3D printing of Inconel 718: Densification, microstructural evolution and challenges☆," *Current Opinion in Solid State and Materials Science*, vol. 21, no. 4, pp. 207–218, Aug. 2017, <https://doi.org/10.1016/j.cossms.2016.12.002>.
- [69] R. Jiang, L. Monteil, K. Kimes, A. Mostafaei, and M. Chmielus, "Influence of powder type and binder saturation on binder jet 3D-printed and sintered Inconel 625 samples," *The International Journal of Advanced Manufacturing Technology*, vol. 116, no. 11, pp. 3827–3838, Oct. 2021, <https://doi.org/10.1007/s00170-021-07496-3>.
- [70] T. Dahmen *et al.*, "Densification, microstructure, and mechanical properties of heat-treated MAR-M247 fabricated by Binder Jetting," *Additive Manufacturing*, vol. 39, p. 101912, Mar. 2021, <https://doi.org/10.1016/j.addma.2021.101912>.
- [71] M. Khademitab, P. R. de Vecchis, P. Staszal, M. K. Vaicik, M. Chmielus, and A. Mostafaei, "Structure-property relationships of differently heat-treated binder jet printed Co-Cr-Mo biomaterial," *Materials Today Communications*, vol. 38, p. 107716, Mar. 2024, <https://doi.org/10.1016/j.mtcomm.2023.107716>.
- [72] S. Im *et al.*, "Evaluation of Different Sintering Agents for Binder Jetting of Aluminum Alloy," *Journal of Materials Engineering and Performance*, vol. 32, no. 21, pp. 9550–9560, Nov. 2023, <https://doi.org/10.1007/s11665-023-07829-1>.
- [73] M. Zanon, A. Müller, J. Croteau, N. Murphy, J. Workman, and T. Pelletiers, "Metal Binder-jetting Of Aluminium-based Alloys," in *World PM2022 Proceedings*, Lyon, France, Sep. 2022, <https://doi.org/10.59499/WP225367982>.
- [74] A. Simchi, F. Petzoldt, T. Hartwig, S. B. Hein, B. Barthel, and L. Reineke, "Microstructural development during additive manufacturing of biomedical grade Ti-6Al-4V alloy by three-dimensional binder jetting: material aspects and

- mechanical properties," *The International Journal of Advanced Manufacturing Technology*, vol. 127, no. 3, pp. 1541–1558, Jul. 2023, <https://doi.org/10.1007/s00170-023-11661-1>.
- [75] Z. Zeng, M. Salehi, A. Kopp, S. Xu, M. Esmaily, and N. Birbilis, "Recent progress and perspectives in additive manufacturing of magnesium alloys," *Journal of Magnesium and Alloys*, vol. 10, no. 6, pp. 1511–1541, Jun. 2022, <https://doi.org/10.1016/j.jma.2022.03.001>.
- [76] D. H. Cho, D. Dean, and A. A. Luo, "Mechanical and corrosion properties of full liquid phase sintered WE43 magnesium alloy specimens fabricated via binder jetting additive manufacturing," *Journal of Magnesium and Alloys*, vol. 12, no. 7, pp. 2711–2724, Jul. 2024, <https://doi.org/10.1016/j.jma.2024.06.023>.
- [77] J. Chen and B. Chen, "Progress in Additive Manufacturing of Magnesium Alloys: A Review," *Materials*, vol. 17, no. 15, p. 3851, Jan. 2024, <https://doi.org/10.3390/ma17153851>.
- [78] Y. Bai and C. B. Williams, "An exploration of binder jetting of copper," *Rapid Prototyping Journal*, vol. 21, no. 2, pp. 177–185, Mar. 2015, <https://doi.org/10.1108/RPJ-12-2014-0180>.
- [79] H. Miyanaji, D. Ma, M. A. Atwater, K. A. Darling, V. H. Hammond, and C. B. Williams, "Binder jetting additive manufacturing of copper foam structures," *Additive Manufacturing*, vol. 32, p. 100960, Mar. 2020, <https://doi.org/10.1016/j.addma.2019.100960>.
- [80] A. Yegyan Kumar, J. Wang, Y. Bai, S. T. Huxtable, and C. B. Williams, "Impacts of process-induced porosity on material properties of copper made by binder jetting additive manufacturing," *Materials & Design*, vol. 182, p. 108001, Nov. 2019, <https://doi.org/10.1016/j.matdes.2019.108001>.
- [81] T. Romano, E. Migliori, M. Mariani, N. Lecis, and M. Vedani, "Densification behaviour of pure copper processed through cold pressing and binder jetting under different atmospheres," *Rapid Prototyping Journal*, vol. 28, no. 6, pp. 1023–1039, Jan. 2022, <https://doi.org/10.1108/RPJ-09-2021-0243>.
- [82] P. Nandwana, R. Kannan, and D. Siddel, "Microstructure evolution during binder jet additive manufacturing of H13 tool steel," *Additive Manufacturing*, vol. 36, p. 101534, Dec. 2020, <https://doi.org/10.1016/j.addma.2020.101534>.
- [83] J. Liu, R. Kannan, D. Zhang, T. Liu, P. Nandwana, and A. Devaraj, "Multi-scale characterization of supersolidus liquid phase sintered H13 tool steel manufactured via binder jet additive manufacturing," *Additive Manufacturing*, vol. 56, p. 102834, Aug. 2022, <https://doi.org/10.1016/j.addma.2022.102834>.
- [84] R. K. Enneti, K. C. Prough, T. A. Wolfe, A. Klein, N. Studley, and J. L. Trasorras, "Sintering of WC-12%Co processed by binder jet 3D printing (BJ3DP) technology," *International Journal of Refractory Metals and Hard Materials*, vol. 71, pp. 28–35, Feb. 2018, <https://doi.org/10.1016/j.ijrmhm.2017.10.023>.
- [85] M. Lehmann, C. G. Kolb, J. Gschloessl, and M. F. Zaeh, "Using particle-loaded inks to selectively change the material properties in binder-jetted WC-Co parts," *Journal of Materials Science*, vol. 58, no. 41, pp. 16089–16104, Nov. 2023, <https://doi.org/10.1007/s10853-023-09023-z>.

- [86] T. Zhang, Y. Tan, and C. Liu, "Enhancing mechanical properties and density of WC-Co with pressureless sintering via shell structure binder jetting additive manufacturing," *International Journal of Refractory Metals and Hard Materials*, vol. 123, p. 106790, Sep. 2024, <https://doi.org/10.1016/j.ijrmhm.2024.106790>.
- [87] T. A. Wolfe, R. M. Shah, K. C. Prough, and J. L. Trasorras, "Binder jetting 3D printed cemented carbide: Mechanical and wear properties of medium and coarse grades," *International Journal of Refractory Metals and Hard Materials*, vol. 113, p. 106197, Jun. 2023, <https://doi.org/10.1016/j.ijrmhm.2023.106197>.
- [88] Z. Zhao *et al.*, "A Short Review of Advancements in Additive Manufacturing of Cemented Carbides," *Crystals*, vol. 15, no. 2, p. 146, 2025, <https://doi.org/10.3390/cryst15020146>.
- [89] T. A. L. Néel, P. Mognol, and J.-Y. Hascoët, "A review on additive manufacturing of sand molds by binder jetting and selective laser sintering," *Rapid Prototyping Journal*, vol. 24, no. 8, pp. 1325–1336, Oct. 2018, <https://doi.org/10.1108/RPJ-10-2016-0161>.
- [90] "Desktop Metal materials - engineered to perform," *Desktop Metal Inc.* <https://www.desktopmetal.com/materials/> (accessed Mar. 25, 2025).
- [91] "PX100 Metal Binder Jetting 3D Printer - Formerly Digital Metal," *Markforged Holding Corporation.* <https://markforged.com/3d-printers/px100> (accessed Mar. 25, 2025).
- [92] "Materials & Binders-EASYMFG," *EASYMFG.* <https://www.easymfg3d.com/binders> (accessed Mar. 25, 2025).
- [93] "Binder Jet Larger parts at industrial scale," *GE Colibrium Additive.* <https://www.colibriumadditive.com/printers/binder-jet> (accessed Mar. 25, 2025).
- [94] "Metal 3D Printer - HP Metal Jet S100 3D Printing Solution," *HP Inc.* <https://www.hp.com/gb-en/printers/3d-printers/products/metal-jet.html> (accessed Mar. 25, 2025).
- [95] "Aluminium Metal binder Jetting (BJT)," *Ricoh Company, Ltd.* <https://3d.ricoh.com/technologies/metal-binder-jetting-bjt/> (accessed Mar. 25, 2025).
- [96] W. D. Yoo, J. H. Lee, K. T. Youn, and Y. M. Rhyim, "Study on the Microstructure and Mechanical Properties of 17-4 PH Stainless Steel Depending on Heat Treatment and Aging Time," *Solid State Phenomena*, vol. 118, pp. 15–20, 2006, <https://doi.org/10.4028/www.scientific.net/SSP.118.15>.
- [97] Metal Powder Industries Federation, *MPIF STANDARD 35 - STRUCTURAL PARTS.* 2018.
- [98] B09 Committee, "Standard Specification for Metal Injection Molded (MIM) Materials," ASTM B883-24.
- [99] M. Villa *et al.*, "Aging 17-4 PH martensitic stainless steel prior to hardening: effects on martensitic transformation, microstructure and properties," *Materialia*, vol. 32, p. 101882, Dec. 2023, <https://doi.org/10.1016/j.mtla.2023.101882>.

- [100] U. K. Viswanathan, S. Banerjee, and R. Krishnan, "Effects of aging on the microstructure of 17-4 PH stainless steel," *Materials Science and Engineering: A*, vol. 104, pp. 181–189, Oct. 1988, [https://doi.org/10.1016/0025-5416\(88\)90420-X](https://doi.org/10.1016/0025-5416(88)90420-X).
- [101] M. Murayama, K. Hono, and Y. Katayama, "Microstructural evolution in a 17-4 PH stainless steel after aging at 400 °C," *Metallurgical and Materials Transactions A*, vol. 30, no. 2, pp. 345–353, Feb. 1999, <https://doi.org/10.1007/s11661-999-0323-2>.
- [102] M. Q. Kareem, T. Mikó, G. Gergely, and Z. Gácsi, "A review on the production of 17-4PH parts using press and sinter technology," *Science Progress*, vol. 106, no. 1, pp. 1–31, Jan. 2023, <https://doi.org/10.1177/00368504221146060>.
- [103] C. N. Hsiao, C. S. Chiou, and J. R. Yang, "Aging reactions in a 17-4 PH stainless steel," *Materials Chemistry and Physics*, vol. 74, no. 2, pp. 134–142, Mar. 2002, [https://doi.org/10.1016/S0254-0584\(01\)00460-6](https://doi.org/10.1016/S0254-0584(01)00460-6).
- [104] Y. Wu, R. M. German, D. Blaine, B. Marx, and C. Schlaefer, "Effects of residual carbon content on sintering shrinkage, microstructure and mechanical properties of injection molded 17-4 PH stainless steel," *Journal of Materials Science*, vol. 37, no. 17, pp. 3573–3583, Sep. 2002, <https://doi.org/10.1023/A:1016532418920>.
- [105] X. Xu *et al.*, "Experimental and theoretical study on static recrystallization of a low-density ferritic steel containing 4 mass% aluminum," *Materials & Design*, vol. 180, p. 107924, Jun. 2019, <https://doi.org/10.1016/j.matdes.2019.107924>.
- [106] F. C. Campbell, Ed., "Diffusion," in *Elements of Metallurgy and Engineering Alloys*, ASM International, pp. 63–73, June 2008, <https://doi.org/10.31399/asm.tb.emea.t52240063>.
- [107] H. Mehrer, Ed., "Self-diffusion in Metals," in *Diffusion in Solids: Fundamentals, Methods, Materials, Diffusion-Controlled Processes*, Berlin, Heidelberg: Springer, pp. 297–312, 2007, https://doi.org/10.1007/978-3-540-71488-0_17.
- [108] K. C. Antony, "Aging Reactions in Precipitation Hardenable Stainless Steel," *JOM*, vol. 15, no. 12, pp. 922–927, Dec. 1963, <https://doi.org/10.1007/BF03397271>.
- [109] H. J. Rack and D. Kalish, "The strength, fracture toughness, and low cycle fatigue behavior of 17-4 PH stainless steel," *Metallurgical transactions*, vol. 5, no. 7, pp. 1595–1605, Jul. 1974, <https://doi.org/10.1007/BF02646331>.
- [110] B. AlMangour and J.-M. Yang, "Integration of Heat Treatment with Shot Peening of 17-4 Stainless Steel Fabricated by Direct Metal Laser Sintering," *JOM*, vol. 69, no. 11, pp. 2309–2313, Nov. 2017, <https://doi.org/10.1007/s11837-017-2538-9>.
- [111] A. Elliott and C. Cramer, "Binder Jetting and Sintering in Additive Manufacturing," in *Additive Manufacturing Processes*, vol. 24, D. L. Bourell, W. Frazier, H. Kuhn, and M. Seifi, Eds. ASM International, pp. 239–246, June 2020, <https://doi.org/10.31399/asm.hb.v24.a0006569>.
- [112] S. Cacace, M. Boccadoro, and Q. Semeraro, "Investigation on the effect of the gas-to-metal ratio on powder properties and PBF-LB/M processability," *Progress in Additive Manufacturing*, vol. 9, no. 4, pp. 889–904, Aug. 2024, <https://doi.org/10.1007/s40964-023-00490-z>.
- [113] J. Kowen, "The evolving story of metal Binder Jetting: The pain and the promise," *Powder Injection Moulding International*, vol. 15, no. 3, pp. 79–91, Sep. 2021.

- [114] I. Gibson, D. Rosen, B. Stucker, and M. Khorasani, "Binder Jetting," in *Additive Manufacturing Technologies*, I. Gibson, D. Rosen, B. Stucker, and M. Khorasani, Eds. Cham: Springer International Publishing, pp. 237–252, 2021, https://doi.org/10.1007/978-3-030-56127-7_8.
- [115] M. Munsch, M. Schmidt-Lehr, and E. Wycisk, "Metal Additive Manufacturing with sinter-based technologies," *AM Power Insights*, vol. 3, pp. 17–37, Oct. 2018.
- [116] B. Barthel, M. Schmidt-Lehr, E. Wycisk, and M. Munsch, "Metal Binder Jetting Implementation," *AM Power Insights*, vol. 14, pp. 28–31, Mar. 2024.
- [117] S. B. Hein, C. Aumund-Kopp, and B. Barthel, "Binder Jet metal Additive Manufacturing: Process chain considerations when moving towards series production," *Metal AM*, vol. 4, no. 4, pp. 79–85, Winter 2018.
- [118] S. R. Narasimharaju *et al.*, "A comprehensive review on laser powder bed fusion of steels: Processing, microstructure, defects and control methods, mechanical properties, current challenges and future trends," *Journal of Manufacturing Processes*, vol. 75, pp. 375–414, Mar. 2022, <https://doi.org/10.1016/j.jmapro.2021.12.033>.
- [119] V. Bechný *et al.*, "Roughness surface analysis of samples produced by the additive manufacturing process," *Transportation Research Procedia*, vol. 74, pp. 702–708, Jan. 2023, <https://doi.org/10.1016/j.trpro.2023.11.200>.
- [120] A. Charles, M. Bayat, A. Elkaseer, L. Thijs, J. H. Hattel, and S. Scholz, "Elucidation of dross formation in laser powder bed fusion at down-facing surfaces: Phenomenon-oriented multiphysics simulation and experimental validation," *Additive Manufacturing*, vol. 50, p. 102551, Feb. 2022, <https://doi.org/10.1016/j.addma.2021.102551>.
- [121] A. Charles, A. Elkaseer, U. Paggi, L. Thijs, V. Hagenmeyer, and S. Scholz, "Down-facing surfaces in laser powder bed fusion of Ti6Al4V: Effect of dross formation on dimensional accuracy and surface texture," *Additive Manufacturing*, vol. 46, p. 102148, Oct. 2021, <https://doi.org/10.1016/j.addma.2021.102148>.
- [122] K. Raoufi, S. Manoharan, T. Etheridge, B. K. Paul, and K. R. Haapala, "Cost and Environmental Impact Assessment of Stainless Steel Microreactor Plates using Binder Jetting and Metal Injection Molding Processes," *Procedia Manufacturing*, vol. 48, pp. 311–319, Jan. 2020, <https://doi.org/10.1016/j.promfg.2020.05.052>.
- [123] J. Ye, M. M. Alam, and C. Okwudire, "Brief Paper: A Preliminary Study on Depowdering of Fragile Objects Using Robots in Binder Jetting Additive Manufacturing," in *Proceedings of the ASME 2024 19th International Manufacturing Science and Engineering Conference*, Knoxville, Tennessee, USA, Jun. 2024, <https://doi.org/10.1115/MSEC2024-125150>.
- [124] A. Cabo Rios, E. Hryha, E. Olevsky, and P. Harlin, "Sintering anisotropy of binder jetted 316L stainless steel: part I – sintering anisotropy," *Powder Metallurgy*, pp. 1–10, Dec. 2021, <https://doi.org/10.1080/00325899.2021.2020485>.
- [125] A. Cabo Rios, M. Persson, E. Hryha, and E. Olevsky, "Phenomenological sintering model and experimental validation of gravity-induced distortions in binder-jetted stainless steel components," *Ceramics International*, vol. 50, no. 19, Part C, pp. 37268–37281, Oct. 2024, <https://doi.org/10.1016/j.ceramint.2024.04.427>.

- [126] A. Roberts *et al.*, “Sintering Simulation of Metal AM and MIM Parts Using Growth-Based Generative Design,” *International Journal of Powder Metallurgy*, vol. 58, no. 1, pp. 21–33, Jan. 2022.
- [127] E. Torresani *et al.*, “Sintering model for predicting distortion of additively manufactured complex parts,” *Rapid Prototyping Journal*, vol. 30, no. 11, pp. 369–383, Dec. 2024, <https://doi.org/10.1108/RPJ-05-2024-0231>.
- [128] K. Zhang *et al.*, “Numerical simulation and experimental measurement of pressureless sintering of stainless steel part printed by Binder Jetting Additive Manufacturing,” *Additive Manufacturing*, vol. 47, p. 102330, Nov. 2021, <https://doi.org/10.1016/j.addma.2021.102330>.
- [129] A. Strauß, P. Quadbeck, O. Andersen, S. Riecker, H.-D. Böhm, and T. Weißgärber, “Gas Analysis and Optimization of Debinding and Sintering Processes for Metallic Binder-Based AM*,” *HTM Journal of Heat Treatment and Materials*, vol. 77, no. 6, pp. 437–448, Dec. 2022, <https://doi.org/10.1515/htm-2022-1033>.
- [130] “Insight from Fraunhofer IFAM’s 4th Workshop on Sinter-based Additive Manufacturing: A status update,” *Powder Injection Moulding International*, vol. 17, no. 4, pp. 77–78, 2023.
- [131] “Metal AM on an industrial scale: GKN Additive draws on decades of sintering expertise to commercialise Binder Jetting,” *Metal AM*, vol. 9, no. 2, pp. 165–171, 2023.
- [132] “Indo-MIM uses Binder Jetting to manufacture over 800 tool inserts,” *Powder Injection Moulding International*, vol. 18, no. 2, p. 17, 2024.
- [133] “Azoth: Driving the acceptance of sinter-based Additive Manufacturing in the automotive industry and beyond,” *Powder Injection Moulding International*, vol. 18, no. 3, pp. 67–78, Winter 2024.
- [134] “China’s Zoltrix using HP Metal Jet Binder Jetting to produce hundreds of thousands of consumer electronics parts,” *Powder Injection Moulding International*, vol. 18, no. 4, p. 12, 2024.
- [135] “Alliance MIM additively manufactures stainless steel watch case for luxury watchmaker,” *Powder Injection Moulding International*, vol. 16, no. 3, p. 9, 2022.
- [136] R. M. German, “1 - Metal powder injection molding (MIM): key trends and markets,” in *Handbook of Metal Injection Molding*, D. F. Heaney, Ed. Woodhead Publishing, pp. 1–25, January 2012, <https://doi.org/10.1533/9780857096234.1>.
- [137] “Customisable stainless steel Italian watch uses HP’s Binder Jetting technology,” *Powder Injection Moulding International*, vol. 19, no. 1, p. 38, Spring 2025.
- [138] “Legor introduces 3D Metal Jet Printing Service aimed at jewellery, fashion and industrial sectors,” *Metal AM*, vol. 10, no. 2, p. 96, Summer 2024.
- [139] P. Bidare, R. Abdullah, A. Jiménez, and K. Essa, “Powder reusability in Metal Binder Jetting,” *Proceedings of the Institution of Mechanical Engineers, Part E: Journal of Process Mechanical Engineering*, vol. 238, no. 4, pp. 1554–1560, Aug. 2024, <https://doi.org/10.1177/09544089221147778>.

- [140] B. Barthel, F. Janas, and S. Wieland, "Powder condition and spreading parameter impact on green and sintered density in metal binder jetting," *Powder Metallurgy*, vol. 64, no. 5, pp. 378–386, Oct. 2021, <https://doi.org/10.1080/00325899.2021.1912923>.
- [141] K. Janzen, K. Kallies, L. Waalkes, P. Imgrund, and C. Emmelmann, "Influence of Different Powder Conditioning Strategies on Metal Binder Jetting with Ti-6Al-4V," *Materials*, vol. 17, no. 3, p. 750, Feb. 2024, <https://doi.org/10.3390/ma17030750>.
- [142] "Desktop Metal showcases its enhanced Production System for high volume Additive Manufacturing," *Metal AM*, vol. 4, no. 4, pp. 102–103, Winter 2018.
- [143] "Desktop Metal upgrade enables titanium and aluminium Binder Jetting," *Powder Injection Moulding International*, vol. 18, no. 2, p. 26, Summer 2024.
- [144] B. Barthel, M. Mirz, and F. Petzoldt, "Process Development Of Grade A11 High Carbon Tool Steel For Metal Binder Jetting," in *World PM2022 Proceedings*, Lyon, France, Sep. 2022, <https://doi.org/10.59499/WP225367264>.
- [145] S. Wieland, L. Reineke, J. Eckel, J. Giel, and S. B. Hein, "Curing Behaviour Of Non-Corrosion-Resistant Tool Steels In Metal Binder Jetting," in *Euro PM2023 Proceedings*, Lisbon, Portugal, 2023, <https://doi.org/10.59499/EP235764652>.
- [146] M. Hrubovčáková, Dudrová, E. Hryha, and M. Kabátová, "Processing Conditions And Reduction Of Oxides During Sintering Of Chromium Pre-Alloyed Steel," *Powder Metallurgy Progress*, vol. 12, no. 3, pp. 144–158, 2012.
- [147] M. N. Rahaman, "The Process of Thermal Debinding," in *Inorganic Reactions and Methods*, vol. 18, Wiley-VCH, Inc., pp. 32–34, January 1999, <https://doi.org/10.1002/9780470145333.ch21>.
- [148] R. M. German, "Chapter Fifteen - Sintering Practice," in *Sintering: from Empirical Observations to Scientific Principles*, R. M. German, Ed. Boston: Butterworth-Heinemann, pp. 471–512, January 2014, <https://doi.org/10.1016/B978-0-12-401682-8.00015-X>.
- [149] M. Phillips and P. Pourtalet, "Understanding parameters for removal of lubricants from P/M tool steels and stainless steels to improve quality," *Industrial Heating*, pp. 37–43, Jan. 1993.
- [150] S. Ray and R. P. Cooney, "Chapter 9 - Thermal Degradation of Polymer and Polymer Composites," in *Handbook of Environmental Degradation of Materials (Third Edition)*, M. Kutz, Ed. William Andrew Publishing, pp. 185–206, January 2018, <https://doi.org/10.1016/B978-0-323-52472-8.00009-5>.
- [151] E. Hryha, E. Dudrova, and L. Nyborg, "Critical Aspects of Alloying of Sintered Steels with Manganese," *Metallurgical and Materials Transactions A*, vol. 41, no. 11, pp. 2880–2897, Nov. 2010, <https://doi.org/10.1007/s11661-010-0357-5>.
- [152] P. Quadbeck, A. Strauß, and T. Weißgärber, "Decarburization and Gas Formation During Sintering of Alloyed PM Steel Components," *Metallurgical and Materials Transactions B*, vol. 55, no. 6, pp. 4352–4360, Dec. 2024, <https://doi.org/10.1007/s11663-024-03237-5>.

- [153] P. Quadbeck, B. Schreyer, A. Strauß, T. Weissgaerber, and B. Kieback, "In-situ monitoring of gas atmospheres during debinding and sintering of PM steel components," in *World PM2010 Congress Proceedings*, Florence, Italy, Oct. 2010.
- [154] S. Karamchedu, E. Hryha, and L. Nyborg, "Changes in the surface chemistry of chromium-alloyed powder metallurgical steel during delubrication and their impact on sintering," *Journal of Materials Processing Technology*, vol. 223, pp. 171–185, Sep. 2015, <https://doi.org/10.1016/j.jmatprotec.2015.03.054>.
- [155] R. De Oro Calderon, C. Gierl-Mayer, and H. Danninger, "Thermoanalytical techniques for characterizing sintering processes in ferrous powder metallurgy," *Journal of Thermal Analysis and Calorimetry*, vol. 148, no. 4, pp. 1309–1320, Nov. 2022, <https://doi.org/10.1007/s10973-022-11740-7>.
- [156] Z. A. Munir, "Analytical treatment of the role of surface oxide layers in the sintering of metals," *Journal of Materials Science*, vol. 14, no. 11, pp. 2733–2740, Nov. 1979, <https://doi.org/10.1007/BF00610647>.
- [157] H. Danninger, R. de Oro Calderon, and C. Gierl-Mayer, "Chemical reactions during sintering of PM steel compacts as a function of the alloying route," *Powder Metallurgy*, vol. 61, no. 3, pp. 241–250, Jul. 2018, <https://doi.org/10.1080/00325899.2018.1458489>.
- [158] E. Hryha, R. Shvab, H. Gruber, A. Leicht, and L. Nyborg, "Surface Oxide State on Metal Powder and its Changes during Additive Manufacturing: an Overview," *Metallurgia Italiana*, vol. 3, pp. 34–39, 2018.
- [159] E. Hryha and L. Nyborg, "Surface Oxides on Metal Powders: An Overview of the Effect of Alloy Composition and Manufacturing Method," in *World PM2016 Proceedings*, Hamburg, Germany, Oct. 2016.
- [160] E. Hryha and L. Nyborg, "Thermogravimetry study of the effectiveness of different reducing agents during sintering of Cr-prealloyed PM steels," *Journal of Thermal Analysis and Calorimetry*, vol. 118, no. 2, pp. 825–834, Nov. 2014, <https://doi.org/10.1007/s10973-014-3915-z>.
- [161] L. Nyborg and E. Hryha, "Characteristics of Surface Oxides: Similarities and Differences between Gas and Water Atomized Steel Powders," in *Euro PM2013 Congress Proceedings*, Gothenburg, Sweden, Sep. 2013.
- [162] E. Hryha, C. Gierl, L. Nyborg, H. Danninger, and E. Dudrova, "Surface composition of the steel powders pre-alloyed with manganese," *Applied Surface Science*, vol. 256, no. 12, pp. 3946–3961, Apr. 2010, <https://doi.org/10.1016/j.apsusc.2010.01.055>.
- [163] J. H. E. Jeffes, "Ellingham Diagrams," in *Encyclopedia of Materials: Science and Technology*, K. H. J. Buschow, R. W. Cahn, M. C. Flemings, B. Ilshner, E. J. Kramer, S. Mahajan, and P. Veyssi re, Eds. Oxford: Elsevier, pp. 2751–2753, January 2001, <https://doi.org/10.1016/B0-08-043152-6/00490-3>.
- [164] S.-L. Shang, S. Lin, M. C. Gao, D. G. Schlom, and Z.-K. Liu, "Ellingham diagrams of binary oxides," *APL Materials*, vol. 12, no. 8, p. 081110, Aug. 2024, <https://doi.org/10.1063/5.0216426>.

- [165] M. Hasegawa, "Chapter 3.3 - Ellingham Diagram," in *Treatise on Process Metallurgy*, S. Seetharaman, Ed. Boston: Elsevier, pp. 507–516, January 2014, <https://doi.org/10.1016/B978-0-08-096986-2.00032-1>.
- [166] P. Stratton, "Ellingham diagrams – their use and misuse," *International Heat Treatment and Surface Engineering*, vol. 7, no. 2, pp. 70–73, Jun. 2013, <https://doi.org/10.1179/1749514813Z.00000000053>.
- [167] C. W. Bale *et al.*, "FactSage thermochemical software and databases," *Calphad*, vol. 26, no. 2, pp. 189–228, Jun. 2002, [https://doi.org/10.1016/S0364-5916\(02\)00035-4](https://doi.org/10.1016/S0364-5916(02)00035-4).
- [168] E. Hryha, E. Dudrova, and L. Nyborg, "On-line control of processing atmospheres for proper sintering of oxidation-sensitive PM steels," *Journal of Materials Processing Technology*, vol. 212, no. 4, pp. 977–987, Apr. 2012, <https://doi.org/10.1016/j.jmatprotec.2011.12.008>.
- [169] H. Danninger, R. de Oro Calderon, and C. Gierl-Mayer, "Powder Metallurgy and Sintered Materials," in *Ullmann's Encyclopedia of Industrial Chemistry*, John Wiley & Sons, Ltd, pp. 1–57, 2017, https://doi.org/10.1002/14356007.a22_105.pub2.
- [170] H. Danninger and C. Gierl-Mayer, "New Alloying Systems for Ferrous Powder Metallurgy PrecisionParts," *Science of Sintering*, vol. 40, no. 1, pp. 33–46, Jan. 2008, <https://doi.org/10.2298/SOS0801033D>.
- [171] E. Hryha and L. Nyborg, "Changes in oxide chemistry during consolidation of Cr/Mn water atomized steel powder," *Powder Metallurgy Progress*, vol. 11, no. 1–2, pp. 42–50, 2011.
- [172] R. Oro, M. Campos, E. Hryha, J. M. Torralba, and L. Nyborg, "Surface phenomena during the early stages of sintering in steels modified with Fe–Mn–Si–C master alloys," *Materials Characterization*, vol. 86, pp. 80–91, Dec. 2013, <https://doi.org/10.1016/j.matchar.2013.07.022>.
- [173] C. Gierl-Mayer, R. de Oro Calderon, and H. Danninger, "The Role of Oxygen Transfer in Sintering of Low Alloy Steel Powder Compacts: A Review of the 'Internal Getter' Effect," *JOM*, vol. 68, no. 3, pp. 920–927, Mar. 2016, <https://doi.org/10.1007/s11837-016-1819-z>.
- [174] D. Chasoglou, E. Hryha, and L. Nyborg, "Effect of process parameters on surface oxides on chromium-alloyed steel powder during sintering," *Materials Chemistry and Physics*, vol. 138, no. 1, pp. 405–415, Feb. 2013, <https://doi.org/10.1016/j.matchemphys.2012.11.074>.
- [175] H. Danninger, C. Gierl-Mayer, S. Kremel, G. Leitner, and Y. Yu, "Degassing and Deoxidation Processes During Sintering of Unalloyed and Alloyed PM Steels," *Powder Metallurgy Progress*, vol. 2, pp. 125–140, Jan. 2002.
- [176] M. F. Ashby, S. Bahk, J. Bevk, and D. Turnbull, "The influence of a dispersion of particles on the sintering of metal powders and wires," *Progress in Materials Science*, vol. 25, no. 1, pp. 1–34, Jan. 1980, [https://doi.org/10.1016/0079-6425\(80\)90013-4](https://doi.org/10.1016/0079-6425(80)90013-4).

- [177] C. Gierl-Mayer, "Reactions between ferrous powder compacts and atmospheres during sintering – an overview," *Powder Metallurgy*, vol. 63, pp. 1–17, Aug. 2020, <https://doi.org/10.1080/00325899.2020.1810427>.
- [178] E. Hryha and J. Wendel, "Effect of heating rate and process atmosphere on the thermodynamics and kinetics of the sintering of pre-alloyed water-atomized powder metallurgy steels," *Journal of the American Ceramic Society*, vol. 102, no. 2, pp. 748–756, 2019, <https://doi.org/10.1111/jace.16079>.
- [179] V. Kerlins, "Modes of Fracture," in *Fractography*, vol. 12, ASM Handbook Committee, Ed. ASM International, pp. 12–71, January 1987, <https://doi.org/10.31399/asm.hb.v12.a0001831>.
- [180] E. Hryha and L. Nyborg, "Oxide Transformation in Cr-Mn-Prealloyed Sintered Steels: Thermodynamic and Kinetic Aspects," *Metallurgical and Materials Transactions A*, vol. 45, no. 4, pp. 1736–1747, Apr. 2014, <https://doi.org/10.1007/s11661-013-1969-3>.
- [181] R. Oro, E. Hryha, M. Campos, and J. M. Torralba, "Effect of processing conditions on microstructural features in Mn–Si sintered steels," *Materials Characterization*, vol. 95, pp. 105–117, Sep. 2014, <https://doi.org/10.1016/j.matchar.2014.06.011>.
- [182] R. T. CUNDILL, MARSH, E., and K. A. and RIDAL, "Mechanical Properties of Sinter/Forged Low-Alloy Steels," *Powder Metallurgy*, vol. 13, no. 26, pp. 165–194, Sep. 1970, <https://doi.org/10.1179/pom.1970.13.26.006>.
- [183] W. Schatt, K.-P. Wieters, and B. Kieback, Eds., "Formteile aus Sintereisen oder Sinterstahl," in *Pulvermetallurgie: Technologien und Werkstoffe*, Berlin, Heidelberg: Springer, pp. 215–261, 2007, https://doi.org/10.1007/978-3-540-68112-0_8.
- [184] H. S. Nayar, "Sintering Atmospheres," in *Powder Metallurgy*, vol. 7, P. Samal and J. Newkirk, Eds. ASM International, pp. 237–246, September 2015, <https://doi.org/10.31399/asm.hb.v07.a0006135>.
- [185] R. Warzel III, "Production Sintering Practices[1]," in *Powder Metallurgy*, vol. 7, P. Samal and J. Newkirk, Eds. ASM International, pp. 337–346, September 2015, <https://doi.org/10.31399/asm.hb.v07.a0006111>.
- [186] C. Blais, "7 - Atmosphere sintering," in *Sintering of Advanced Materials*, Z. Z. Fang, Ed. Woodhead Publishing, pp. 165–188, January 2010, <https://doi.org/10.1533/9781845699949.2.165>.
- [187] "Furnace atmospheres no. 6. Sintering of steels," Linde GmbH, 6. Accessed: Mar. 28, 2025. [Online]. Available: https://static.prd.echannel.linde.com/wcsstore/REN_Industrial_Gas_Store/Sintering-of-steels-brochure-EN.pdf.
- [188] P. A. dePoutiloff and P. K. Samal, "Sintering of Stainless Steels," in *Powder Metallurgy*, vol. 7, P. Samal and J. Newkirk, Eds. ASM International, pp. 433–439, September 2015, <https://doi.org/10.31399/asm.hb.v07.a0006118>.
- [189] M. N. Rahaman, "Sintering Theory and Fundamentals," in *Powder Metallurgy*, vol. 7, P. Samal and J. Newkirk, Eds. ASM International, pp. 205–236, September 2015, <https://doi.org/10.31399/asm.hb.v07.a0006117>.

- [190] R. De Oro Calderon, C. Gierl-Mayer, and H. Danninger, "Application of thermal analysis techniques to study the oxidation/reduction phenomena during sintering of steels containing oxygen-sensitive alloying elements," *Journal of Thermal Analysis and Calorimetry*, vol. 127, pp. 91–105, May 2016, <https://doi.org/10.1007/s10973-016-5508-5>.
- [191] E. Hryha, L. Nyborg, A. Malas, S. Wiberg, and S. Berg, "Carbon control in PM sintering: Industrial applications and experience," *Powder Metallurgy*, vol. 56, no. 1, pp. 5–10, Feb. 2013, <https://doi.org/10.1179/0032589912Z.000000000085>.
- [192] C.-W. Chang, P.-H. Chen, and K.-S. Hwang, "Enhanced Mechanical Properties of Injection Molded 17-4PH Stainless Steel through Reduction of Silica Particles by Graphite Additions," *Materials Transactions*, vol. 51, no. 12, pp. 2243–2250, 2010, <https://doi.org/10.2320/matertrans.M2010209>.
- [193] E. Hryha, S. Karamchedu, D. Riabov, L. Nyborg, and S. Berg, "Effect of Active Components of Sintering Atmosphere on Reduction/Oxidation Processes During Sintering of Cr-Alloyed PM Steels," *Journal of the American Ceramic Society*, vol. 98, no. 11, pp. 3561–3568, 2015, <https://doi.org/10.1111/jace.13607>.
- [194] E. M. Sachs *et al.*, "Methods and systems for condensing a vapor on a powder bed," 11717887, Aug. 08, 2023.
- [195] "Laser-Free Metal 3D Printing with Binder Jetting Technology," Desktop Metal, Inc., 2023. Accessed: Mar. 21, 2025. [Online]. Available: https://www.desktopmetal.com/uploads/2023web_DesktopMetal_UltimateGuideToMetalBinderJetting.pdf.
- [196] W. Zhou *et al.*, "Elucidating the impact of severe oxidation on the powder properties and laser melting behaviors," *Materials & Design*, vol. 221, p. 110959, Sep. 2022, <https://doi.org/10.1016/j.matdes.2022.110959>.
- [197] D. Brunermer, "Saturation in metal Binder Jetting: Simple in principle, complicated in practice?," *Powder Injection Moulding International*, vol. 16, no. 2, pp. 67–73, Jun. 2022.
- [198] B. Hugonnet, J.-M. Missiaen, C. L. Martin, and C. Rado, "Effect of contact alignment on shrinkage anisotropy during sintering: Stereological model, discrete element model and experiments on NdFeB compacts," *Materials & Design*, vol. 191, p. 108575, Jun. 2020, <https://doi.org/10.1016/j.matdes.2020.108575>.
- [199] M. F. McGuire, Ed., "Precipitation-Hardening Stainless Steels," in *Stainless Steels for Design Engineers*, ASM International, pp. 137–146, December 2008, <https://doi.org/10.31399/asm.tb.ssde.t52310137>.
- [200] A. Cabo Rios *et al.*, "Ex-situ characterization and simulation of density fluctuations evolution during sintering of binder jetted 316L," *Materials & Design*, vol. 238, p. 112690, Feb. 2024, <https://doi.org/10.1016/j.matdes.2024.112690>.
- [201] K. Zissel, E. Bernardo, P. Forêt, and E. Hryha, "Impact of oxygen content on debinding of binder jetted 17-4 PH stainless steel: Part I – Debinding," *Powder Metallurgy*, vol. 68, no. 1, pp. 3–15, Dec. 2024, <https://doi.org/10.1177/00325899241307824>.

- [202] K. Zissel, E. Bernardo, P. Forêt, and E. Hryha, "Impact of oxygen content on debinding of binder jetted 17-4 PH stainless steel: Part II – Sintering," *Powder Metallurgy*, vol. 68, no. 1, pp. 16–28, Dec. 2024, <https://doi.org/10.1177/00325899241307871>.
- [203] M. Trunec and J. Cihlář, "Thermal debinding of injection moulded ceramics," *Journal of the European Ceramic Society*, vol. 17, no. 2, pp. 203–209, Jan. 1997, [https://doi.org/10.1016/S0955-2219\(96\)00108-2](https://doi.org/10.1016/S0955-2219(96)00108-2).
- [204] D.-F. Lii, J.-L. Huang, C.-H. Lin, and H.-H. Lu, "The effects of atmosphere on the thermal debinding of injection moulded Si₃N₄ components," *Ceramics International*, vol. 24, no. 2, pp. 99–104, Jan. 1998, [https://doi.org/10.1016/S0272-8842\(96\)00085-5](https://doi.org/10.1016/S0272-8842(96)00085-5).